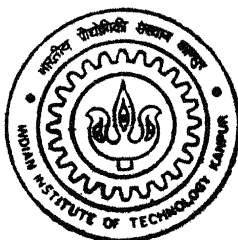


9820607

MAGNETIC FIELD AND VELOCITY MEASUREMENT IN SIMULATED HALL-HEROULT CELL

By
ZUBEIR AHMAD SIDDIQUI

TH
MME/20001M,
Si 13m



DEPARTMENT OF MATERIALS AND METALLURGICAL ENGINEERING
INDIAN INSTITUTE OF TECHNOLOGY, KANPUR

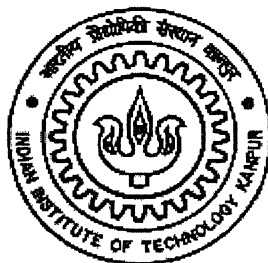
June, 2000

MAGNETIC FIELD AND VELOCITY MEASUREMENT IN SIMULATED HALL-HEROULT CELL

A Thesis Submitted
In Partial Fulfillment of the Requirements
For the Degree of
Master of Technology

By

ZUBEIR AHMAD SIDDIQUI



DEPARTMENT OF MATERIALS AND METALLURGICAL
ENGINEERING

Indian Institute of Technology, Kanpur

JUNE, 2000

6 OCT 2000 AM 11:10

CENTRAL LIBRARY
I.I.T., KANPUR

A132012

11/11
11/11/2000
Sl 13m



A132012

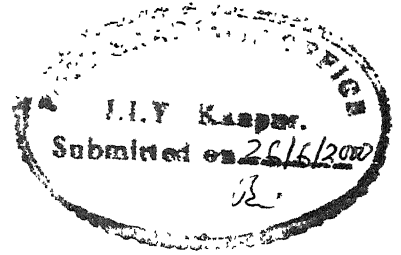
MAGNETIC FIELD AND VELOCITY MEASUREMENT IN SIMULATED HALL-HEROULT CELL

A Thesis Submitted
In Partial Fulfillment of the Requirements
For the Degree of
Master of Technology

By
ZUBEIR AHMAD SIDDIQUI

To the
DEPARTMENT OF MATERIALS AND METALLURGICAL
ENGINEERING
Indian Institute of Technology, Kanpur
JUNE, 2000

CERTIFICATE



This is to certify that the thesis entitled “**Magnetic Field and Velocity Measurement in Simulated Hall-Heroult Cell**” by *Zubeir Ahmad Siddiqui* has been carried out under our supervision, and this has not been submitted elsewhere for a degree.

(Dr. S. P. Mehrotra)

Professor

Department of Materials & Metallurgical Engineering
Indian Institute of Technology, Kanpur

(Dr. Rajiv Shekhar)

Associate Professor

Department of Materials & Metallurgical Engineering
Indian Institute of Technology, Kanpur

Dated : May, 2000



Dedicated to My Father

A real source of light for me, on a dark path of life.

ACKNOWLEDGEMENTS

I acknowledge with sincerity and deep sense of gratitude the expert guidance and continuous encouragement provided by Prof. S. P. Mehrotra and Prof. Rajiv Shekhar through out the course of this work. They provided me a good guidance and at the same time encouraged me to generate my own ideas. Their guidance always acted as catalyst to the progress of work. I am able to finish my thesis only due to their guidance, intellectual support and creative criticism. I offer my most humble and profound indebtedness to them for deep concern both for my academics and for my personal welfare.

I thank the entire staff of the metallurgy and materials engineering department, ITK, for their cooperation. My special thanks are to Mr. G. P. Bajpai, who helped me many times beyond office hours also.

Thanks are due to my friends Santosh, Rohit, Dhaval, Ranjan, Maya, Amit, Sidharth, Saurbh and Sagar for their constant help and moral support during the hard time of my stay. Special thanks to Dulal and Premendra for their help during my experiments, which I carried out at our lab.

Many friends have been helping directly or indirectly. They will always remain in my memory. Words are not sufficient to express my indebtedness to my loving hostel friends.

I would like to thank my family members, villagers and relatives who have been giving their love and affection to me, in spite of my inability to give them time. Finally, I say thank to each and every person who has helped me anyway.

Dated: JUNE 2000

Zubeir Ahmad Siddiqui

TABLE OF CONTANTS

	<u>PAGE</u>
LIST OF FIGURES	ix
LIST OF TABLES	xiii
ABSTRACT	xiv
Chapter 1 INTRODUCTION	1
1.1 Problems in Operation of Hall-Heroult Cells	4
1.2 The Effect of Magnetic and Fluid flow(Velocity) on cell operations	5
1.3 Present Investigation and Its Scope	5
1.4 Brief Description of Thesis Structure	6
Chapter 2 LITERATURE REVIEW	8
2.1 General Features of Magneto-Hydrodynamics in Hall-Heroult Cell	8
2.2 Computation of Temperature, Current, Magnetic Field, Velocity, Melt Topography, and Current Efficiency in Hall-Heroult Cells	11
2.2.1 Temperature Distribution	13
2.2.2 Electric Current Distribution	13
2.2.3 Magnetic Field	14
2.2.4 Melt and Electrolyte Velocities	14
2.2.5 Melt Topography	14
2.2.6 Current Efficiency	15
2.3 Factors Affecting the Fluid Dynamics of Hall-Heroult Cell	15
2.3.1 Effect of Age of Cell	15

2.3.2	Effect of Cold Anode	16
2.3.3	Effect of Anode Geometry	19
2.3.4	Effect of Anode Cathode Distance (ACD)	19
2.3.5	Effect of Ledge Shape	19
2.3.6	Effect of Cell Current	25
2.3.7	Effect of Bus Bar Design	25
2.4	Instability in Electrolyte/metal Interface	31
2.4.1	Types of Metal Pad Waves	32
2.4.1.1	Capillary Wave	32
2.4.1.2	Short Period Wave	32
2.4.1.3	Long Period Wave	32
2.4.2	Application of Interface Wave Analysis in Pot Development	37
2.5	Principle of Velocity Probe	37
2.6	Concluding Remarks	38
Chapter 3	PRESENT INVESTIGATION AND ITS SCOPE	40
Chapter 4	EXPERIMENTAL SETUP AND PROCEDURE	43
4.1	Experimental Setup of Simulated Low temperature Hall-Heroult Cell	43
4.1.1	Components of the Simulated Cell	43
4.1.1.1	Inner Stainless Steel Tank	43
4.1.1.2	Anode Assembly and Bus Bars	44
4.1.1.3	Cathode Collector Bars	44
4.1.1.4	Heating System for the Cell	44
4.1.1.5	Materials Used in the Cell	50
4.1.2	Power Supply	50
4.1.3	Temperature Control of the Cell	52
4.1.4	Current Measuring Instrument	52

4.1.5	Magnetic Field Measuring Instrument	53
4.1.6	Design and Construction of Velocity Probe	53
4.1.7	Design and Fabrication of Calibration Set-up	53
4.2	Experimental Procedure	54
4.2.1	Temperature Measurements	54
4.2.2	Current Density Measurement	54
4.2.3	Magnetic Field Measurements	59
4.2.4	Velocity Measurements	59
4.2.4.1	Calibration of Velocity Probe	59
4.2.4.2	Velocity measurements	60
Chapter 5	RESULTS AND DISCUSSION	70
5.1	Reproducibility Experiments	72
5.2	Thermal Distribution	75
5.3	Current Distribution	75
5.3.1	Effect of Anode-Cathode Distance (ACD)	77
5.3.2	Effect of Total Current Supply to the Cell	77
5.3.3	Effect of Cold Anode	77
5.4	Magnetic Field Distribution	84
5.4.1	Effect of Current Density	84
5.4.2	Effect of Anode-Cathode Distance (ACD)	84
5.4.3	Effect of Cold Anode	84
5.4.4	Effect of Height from Base of the Cell	85
5.4.5	Effect of Bus Bar Design	91
5.5	Velocity Profile	98
5.5.1	Effect of Current Density	98
5.5.2	Effect of ACD	98
5.5.3	Effect of Bus Bar Design	103
5.5.4	Effect of Cold Anode	103

Chapter 6	SUMMARY AND CONCLUSIONS	113
6.1	Suggestions for Future Work	115
APPENDIX A		116
A.1	Flow Chart and Program Structure	116
A.1.1	The Structure of Program Used to Calculate Velocity in the Cell	116
A.2	Validation of Experimental Procedure	121
A.2.1	Experimental Set-Up	121
A.2.2	Experimental Procedure	121
A.2.3	Results and Discussion	124
A.2.3.1	Magnetic Field Measurements	124
A.2.3.2	The E.M.F. Measurements	124
A.2.4	Conclusion	126
REFERENCES		127

LIST OF FIGURES

<u>FIGURE</u>	<u>PAGE</u>
1.1 Noranda Aluminium Reduction Cell	2
2.1 Right hand rule gives force direction as a function of current and magnetic field	12
2.2 Different zones in Hall-Heroult cell	12
2.3 Flow patterns at different ages of the cell	17
2.4 Freeze profiles (a) <150 days (b) >900 days	18
2.5 Horizontal currents in liquid metal for interrupted anodes: (a)corner anode, (b) middle anode, (c) sludge formation	20
2.6 Vertical magnetic flux, case 1: interrupted corner anode	21
2.7 Additional horizontal forces in the liquid metal for two cases: (a)due to an interrupted corner anode (b) interrupted middle anode	21
2.8 Metal velocities in case of interrupted corner anode	22
2.9 Metal pad deformation for interrupted anodes: (a) corner anode (b) middle anode (c) sludge formation	23
2.10 Ledge profile verses cell current efficiency	26
2.11 Effect of ledge lateral toe on current flow	26
2.12 Measured velocity at a point in the Wood's metal verses the square of the current through the model	27
2.13 Computed metal velocities for three cells differing only in design of their risers	28
2.14 Metal flow velocities in 110kA V.S. Soderbreg cell	33
2.15 Metal flow velocities in 100kA H.S. Soderbreg cell	34
2.16 Metal flow velocities in 150 kA end riser prebake cell	34
2.17 Metal flow velocities in 76 kA prebake cell	35
2.18 Metal flow velocities in 150 kA quarter riser cell	35

2.19	Computed and measured (a) magnetic fields (b) and velocities within molten aluminium of the 185 kA Kaiser cell	36
4.1	Schematic diagram of low temperature simulated Hall-Heroult cell	45
4.2	Schematic diagram representing the cell and the heating system assembly	46
4.3a	Top view of bus-bars attached to anodes for end riser design	47
4.3b	Top view of bus-bars attached to anodes for quarter riser design	48
4.4a	Schematic drawing of the end riser design	49
4.4b	Schematic drawing of the quarter riser design	49
4.5	Heating system based on circulation of hot air	51
4.6	Schematic diagram of the velocity probe as used by Banerjee and Evans	55
4.7	Schematic diagram of the modified velocity probe used for measuring velocity	56
4.8	Calibration set-up used to calibrate velocity probe	57
4.9	Points 'A' to 'L' on which measurements are made	58
4.10	Calibration plots for the unmodified velocity probe for both set of tips PQ and RS	61
4.11	Calibration plots for the modified velocity probe for both set of tips PQ and RS	62
4.12	Schematic representation of various parts of net emf	67
4.13	Current verses emf plot, when the emfs generated by the melt flow and drop in the same direction	68
4.14	Current verses emf plot, when the emfs generated by the melt flow and drop in the opposite direction	69
5.1	Block diagram of process representing various inputs and outputs	71
5.2	Measured horizontal components of current densities	73
5.3	Measured horizontal components of current densities	74
5.4	Temperature distribution in simulated cell at mid height of the melt	76
5.5	Measured horizontal components of current densities	78

5.6	Measured horizontal components of current densities	79
5.7	Current density components within the melt with variation in current input	80
5.8	Current density components within melt with variation in current input	81
5.9	Measured horizontal components of current densities for corner cold anode	82
5.10	Measured horizontal components of current densities	83
5.11	Measured magnetic field for end riser design	86
5.12	Measured magnetic field for end riser design	87
5.13	Measured magnetic field for end riser design	88
5.14	Measured magnetic field for corner cold anode case	89
5.15	Measured magnetic field for middle cold anode case	90
5.16	Measured magnetic field at $Z=0$ cm (base of the cell) for the end riser design	92
5.17	Measured and magnetic field at $Z=1.75$ cm (middle plane of the melt) for the end riser design	93
5.18	Measured magnetic field at $Z=3.5$ cm (top plane of the melt) for the end riser design	94
5.19	Measured magnetic field for the quarter riser design	95
5.20	Measured magnetic field for the quarter riser design	96
5.21	Measured magnetic field for the quarter riser design	97
5.22	Square of total current input verses resultant velocity graphs for points 'A', 'B', 'C' and 'D'	99
5.23	Square of total current input verses resultant velocity graphs for points 'E', 'F', 'G' and 'H'	100
5.24	Square of total current input verses resultant velocity graphs for points 'I', 'J', 'K' and 'L'	101
5.25	Measured velocities for ACD 1.0 cm (solid arrow), 1.5 cm (coarse Broken Arrow) and 2.0 cm (fine Broken Arrow)	102

5.26	Measured velocities for the end riser design	105
5.27	Measured velocities for the quarter riser design	106
5.28	Measured velocities for quarter riser design by Banrjee and Evans	107
5.29	Schematic drawing of major current flows, the cell used by Banrjee and Evans : (a) end riser design, (b) the quarter riser design	108
5.30	Measured velocities for end riser design with corner anode as cold anode	109
5.31	Measured velocities for end riser design with middle anode as cold anode	110
5.32	Measured velocities for quarter riser design with corner anode as cold anode	111
5.33	Measured velocities for quarter riser design with middle anode as cold anode	112
A.1	Flow chart of the program used for velocity calculations using velocity probe data	120
A.2	The shape and size of one electrode made of mild steel	122
A.3	The arrangement of electrodes used to validate the experimental procedure for velocity measurements	122
A.4	Experimental set-up of validation experiment (Top view)	123
A.5	The Current verses the emf plots at different velocities of the melt	125

LIST OF TABLES

<u>TABLE</u>		<u>PAGE</u>
2.1	Physical properties of molten aluminium and electrolyte	10
2.2	Typical magnitudes of the fluid velocity, temperature variation, and electromagnetic field strengths	10
2.3	Computed current efficiencies for various cell modifications	29
2.4	Dependency of period on current density	32
4.1	Properties of wood's metal	52
4.2	Ratios of electrical conductivities	52
4.3	Slopes and intercepts of the calibration lines for the modified probe design	60
4.4	Constant part of readings with position and temperature for tips PQ of probe	64
4.5	Constant part of readings with position and temperature for tips RS of probe	64
4.6	Constant part of emf with temperature for point A	64
4.7	Values of constant parameters at different positions of the cell, when E_{net} is in mv and current is in Amp	66
5.1	Process variables and their ranges investigated in various set experiments	70
5.2	Magnetic field (Gauss) recorded in identical experiments on three different days.	72
5.3	Horizontal velocities as measured on three different days under identical experimental conditions	75
5.4	Variation of magnetic field(Gauss) with current density	85
A.1	Magnetic field near the probe in the calibration pot for the current inputs of 6.0 and 15.0 Amp	124
A.2	Emf readings (mv) for varying current inputs at different melt velocities	126

ABSTRACT

Aluminium is made by electrolysis of alumina dissolved in molten cryolite. The process is carried out in large horizontal rectangular cells, known as Hall-Heroult cells. In view of the large amount of electrical energy consumed in these cells, there is considerable incentive for improvement, in energy efficiency. Since the electrolytic process of aluminium production is not likely to be replaced by an alternative process in the near future, worldwide research on aluminium is focused on improved design of the cells for reducing the energy consumption.

The laboratory scale Hall cells operate under actual electrolysis conditions have several difficulties related to: (a) the corrosive nature of the electrolyte, and (b) high level of heat losses. Consequently, one strategy adopted in investigations of Hall cell, is to set-up "low temperature" simulated cells. Data generated on a simulated cell may be used to develop mathematical models that are subsequently used in the design and optimization of the industrial Hall-Heroult cells.

The main objective of the present investigation is to study the magneto-hydrodynamics in the cell and to generate the laboratory scale data on current, magnetic field, and velocity profiles within the cell for different cell changes and upsets.

A physical model, which simulates the electromagnetically driven flow in a Hall cell, has been constructed. The model is approximately one-tenth scale and only a half portion of an actual cell, and it is designed for a total current input of the order 500 Amp, to operate at 100 °C. The low temperature simulated cell contains molten wood's metal, which is driven in a horizontal re-circulating flow by electromagnetic forces.

Effects of current input, anode-cathode distance, 'cold' anodes, and alternative bus bar arrangements ~~on~~ magneto-hydrodynamics have been observed. Measured current, magnetic field, and velocity field distributions are in conformity with those reported for commercial cells. The measured velocities are of the order of 1.0 cm/sec, and are proportional to the square of the current. The flow patterns are found to change markedly, when the bus bar design changes from the end riser design to the quarter riser design.

Chapter 1

INTRODUCTION

The Hall-Heroult cell, in essence, is a tank usually rectangular in shape, consisting of the anodes suspended from the top and the cathodes lying on the bottom of the cell floor, and the two electrodes separated by an electrolyte with electric current flowing through it. The electrolyte consists of alumina dissolved in the molten cryolite ($3\text{NaF} \cdot \text{AlF}_3$) with additions of minor constituents like NaF , CaF_2 , etc. Alumina is reduced into aluminium and oxygen as a result of the electrolysis. Oxygen thus produced, reacts with the carbon anodes forming carbon dioxide (CO_2), which comes out in form of bubbles through the free surface of the electrolyte. The agitation of the bath, caused by the evolution of gases (CO and CO_2) and the magnetic stirring effect produced by the current flowing through the bath helps in dissolution of the fresh additions of Al_2O_3 . The depth of the electrolyte is maintained at about 25 cm. The charging of alumina in fine powder form and tapping of aluminium, which is collected at the bottom of the cell in molten form, take place from time to time to maintain the bath composition as well as the inter-polar distance within closely specified limits. A layer of metal, called metal reserve, stays permanently in the cell and its depth is set according to operating characteristics. Molten aluminium also acts as the cathode in the operation. The geometrical shape of a typical cell is approximately three meters wide, ten meters long, and one meter deep with anodes arranged in two parallel rows (See Fig. 1.1). In certain large cells the number of anodes varies from 16 to 32 in each row. In the electrolytic process, the anodes are consumed and the used ones need to be replaced from time to time.

Temperature in the cell is around 950°C ; approaches its highest value under the anode, and then decreases towards the outer edge of the tank where the electrolyte becomes frozen. This latter region, called 'ledge', provides, insulation and gives protection to the cathode carbon refractory and it is critical for maintaining the heat

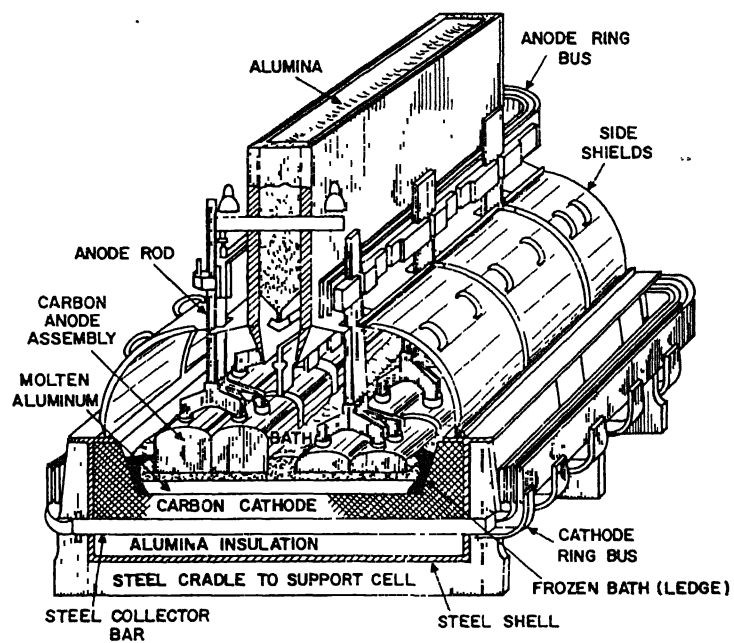


Fig. 1.1 Noranda Aluminium Reduction Cell [1].

balance during the cell operation. The thickness of the ledge varies with variation in the heat content of the electrolyte. Thus, it provides a moving boundary for the flow field. The movement of the ledge boundary, however, is very slow and it is negligible compare to the movement of the electrolyte and molten metal. Heat in the electrolyte is generated by joule heating, resulting from electric current flow through the electrolyte. In some cells the depth of the electrolyte is kept at a minimum as a means of minimizing joule heat, thereby improving the thermal efficiency of the cell. On the other hand, enough joule heat must be provided to avoid excessive ledge thickness, which makes mixing of alumina in the electrolyte difficult.

Velocity profiles in the cell show that the two liquids in the system, the molten aluminium and the electrolyte, are constantly in motion and that the electrolyte/metal interface is always oscillating. This oscillating interface sometimes reaches the underside of the anode, causing short-circuiting - an undesirable feature, resulting in loss in productivity.

Since the cell is primarily a reactor vessel in which chemical reactions take place, the continuous supply and uniform dispersion of the feed stock, the alumina, are essential features of the operation. An excessively low alumina concentration may cause another undesirable features called 'anode effect'. To ensure efficient mass transfer, convective currents and turbulent mixing are the two necessary characteristics of the operation.

Following points are suggested for optimal operation of the cell:

1. There should be minimum heat loss implying high thermal efficiency.
2. There should be an optimal thickness of the ledge implying thermal equilibrium.
3. There should be a uniform concentration of feed stock implying continuous smooth electrochemical reaction with no anode effect.
4. There should be minimum oscillations at the free surfaces to avoid short-circuiting in the cell.

In short, the process should be in a steady-state, which is both optimal and stable.

1.1 PROBLEMS IN OPERATION OF HALL-HEROULT CELLS

A large number of problems are often faced during the operation of the Hall-Heroult cells. Physical phenomena (mass balance, charge balance and momentum balance) in the cell are so closely interrelated that disturbance in one variable affects more or less all other variables. The operating variables, which are usually controlled for smooth functioning of cells, are bath temperature, bath chemistry, bath density, anode design, cathode design, inter-polar distance, anode cathode distance (ACD), and the current distribution.

Some of the common problems found during operation of the cell are: anode effect, instability of metal pad, melting of protective ledge, low current and energy efficiencies, high consumption of anodes as well as cathode carbon refractory.

Anode effect arises when the alumina content of the electrolyte, which decreases with time, reaches below 1 to 2 wt % as compared to the normal value of about 4 to 5 wt %. With low alumina content, the electrolyte loses its good wettability. As a result the electrolyte is no longer able to wash the gas bubbles formed at the anode. This results in formation of a continuous gas film around the anode surface. Being a poor conductor of electric current, the gas film formation increases the anode resistance, which is indicated by sudden shooting up of the cell voltage.

Second problem arises due to short-circuiting of the metal and the anode. It is primarily due to the agitation of the bath by evolving gases (CO and CO_2) and magnetic stirring. The latter aspect is discussed in detail in a subsequent section. During short circuiting a large amount of current flows at the points of contact of two electrodes generating a high temperature in this zone. The localized high temperature may melt the protective ledge causing high consumption of the carbon refractory.

As the refractory consumption in the cell increases, it in turn leads to increase in repairing frequency of the cell in a working plant. Thus, process economy goes down in two ways:

1. Increased price of the electricity and refractory
2. Reduced production per cell due to increased shut down time

1.2 THE EFFECT OF MAGNETIC FIELD AND FLUID FLOW(VELOCITY) ON CELL OPERATIONS

During the operation of the cell, two forces act on the electrolyte: (i) A force due to the interface momentum exchange arising from the anodic gas release (a buoyancy effect), and (ii) an electromagnetic force produced from the interaction between current and magnetic field. The electrolyte flow has important implications for reduction process. It determines mass transfer processes such as alumina mixing, re-oxidation of aluminium, and heat transfer processes such as that between the electrolyte and ledge. Current flow in typical Hall cells varies between 150kA-250kA and produces a strong magnetic field within the cells. This magnetic field interacts with flowing current through to produce an electromagnetic force causing an electromagnetic torque, which provides motion to the conducting melts, the electrolyte and the aluminium metal pad. The electromagnetic force within the cell also causes a horizontal motion, which destabilizes the metal/electrolyte interface. This destabilization may lead to the short-circuiting of the aluminium pad and anode, and erosion of carbon refractory lining by both mechanical abrasion and dissolution of carbon refractory.

Short-circuiting of the metal pad (cathode) and anode, is a major source of thermal instability in the cell. The solid protective ledge, which protects the refractory from erosion, may melt. The efforts of the technology experts are aimed to maintain least turbulent metal/electrolyte interface by reducing the electromagnetic torque with varying various operating as well as design parameters. The maximum effort, however, is to minimize the vertical magnetic field component, which interacts with horizontal currents and creates a swirl and instability in molten aluminium.

1.3 PRESENT INVESTIGATION AND ITS SCOPE

The main commercial objective in aluminium smelting is to reduce the production cost by increasing current and energy efficiencies and reducing carbon consumption. Most Hall cells these days operate with about 90 to 95 % current efficiency. There is

little scope for improvement in this area. However, the energy efficiency of a typical cell is only about 45-48 %, having a larger scope for improvement in this direction. The oscillating metal/electrolyte interface, caused by large electromagnetic forces, is one of the major factors responsible for higher energy consumption. Any improvement in this direction, therefore, requires a better understanding of the magneto-hydrodynamics in the cell, an area which has largely remained ignored hitherto. Due to the complexities of the cell operation at high temperature and under highly corrosive environment prevailing in the cell, measurements of current distribution, magnetic fields and fluids flow, required for understanding of magneto-hydrodynamics, are rather difficult. A simple way would be to estimate these attributes using reliable mathematical models.

The present investigation is a part of a major project which involves formulation of mathematical models to predict the effect of process and design parameters on magneto-hydrodynamics in the cell, and validate these models using experimental data generated in a laboratory scale simulated Hall cell. Since a laboratory scale, single anode Hall cell is highly unstable, coupled with all the problems of commercial cell, current distribution, magnetic field and, melt velocity have been measured using a low temperature, multi-anode, laboratory scale simulated Hall cell using wood's metal as the melt. It is hoped that the data generated in the present investigation will be useful in validating the mathematical models, which are being developed separately as a part of the major project.

1.4 BRIEF DESCRIPTION OF THESIS STRUCTURE

The thesis comprises of six chapters. After this introductory chapter, the second chapter is on literature review, which deals with the relevant literature on various aspects of the magneto-hydrodynamics in cell operation, and the latest developments in this field. Scope of the present investigation is presented in the third chapter. Fourth chapter on experimental set-up and procedure deals with design, fabrication and operational aspects of the multi-anode cell employed in this investigation. Experimental procedures to measure the thermal distribution, current density, magnetic field and

velocity profile in the cell are also described in this chapter. Results of low temperature simulated Hall cell experiments are presented and discussed in the fifth chapter. Sixth chapter presents the summary and conclusions of the complete work. At the end of the thesis Appendix A deals with validation of the experimental procedure used for velocity measurements.

Chapter 2

LITERATURE REVIEW

2.1 GENERAL FEATURES OF MAGNETO-HYDRODYNAMICS IN HALL-HEROULT CELL

In the electrolyte region of the Hall cell, part of the space is occupied by alumina and a part by CO₂ bubbles. At the bottom of the metal, alumina particles get accumulated as some of them sink through electrolyte/metal interface before getting fully dissolved. Strictly speaking, therefore, the space marked “electrolyte” constitutes a zone of three phase flow, gas/liquid/solid, and the space marked “metal”, a zone for a two phase flow, liquid/solid.

Since the cell tank is made of rigid, stationary walls (the only violation of this condition is ledge which may have a time-dependent thickness. But this motion is very slow and may be regarded as a passive response rather than an active primary driving force), in order to have fluid motion, internal driving forces must exist. Two primary driving forces are identified; the first one owes its origin to the electromagnetic field and the second one originates from chemical reactions leading the bubble formation. One may consider that thermal gradient is the third driving force but its magnitude is negligible as compared to the other two forces.

Electromagnetic forces, also known as Lorentz forces, are generated due to interaction between magnetic field within the fluid and electric current flowing through it. The force vector is given by

$$\mathbf{F}_v = \mathbf{J} \times \mathbf{B}$$

where \mathbf{J} is current density and \mathbf{B} is magnetic field vector. Direction of the magnetic field is given by the right hand rule as shown in Fig.2.1 [2]. The Biot-Savart law gives the magnetic field at a specified point caused by each element of the current.

The major effort during electrolysis is to minimise the vertical component of the magnetic field, which produces swirls and instability in molten aluminium pad. It is

well established, that smaller the Anode Cathode Distance (ACD) lower is the energy consumption. However, smaller ACD causes problem of short-circuiting of the metal pad and anode.

The forces, which are to be balanced in the cell, are:

- Electromagnetic forces
- Drag forces
- Pressure gradient

Magneto-hydrodynamics (MHD) related flow has been studied and reported in literature [3-5], through only sparsely. Numerical simulation of gas driven flow has been restricted to only vertical plane or a half anode section of the cell [6,7]. The accuracy of the results, particularly the turbulence prediction, suffers, as the gas bubble escape is 3D in nature. The electrolyte flow has important implications for the reduction process. The electrolyte flow determines the mass transfer processes such as alumina mixing and re-oxidation of aluminium, and heat transfer processes such as that between electrolyte and ledge. The effect of electrolyte flow on alumina mixing has been investigated by Purdie et al. [7]. However, only the effect of gas driven flow is considered. Current efficiency model by Robl et al. [8] has attempted to relate current efficiency to the cell hydrodynamics. Later models by Evans et al. [9] and Echelini et al. [10] take a step further in using the turbulent kinetic energy distribution to assess the mass transfer at the interface. These models, however, include the effect of the MHD force.

The properties of different zones of cell designate the metal as zone 1, the bubble-free electrolyte zone 2, and the bubble-dominated electrolyte zone 3. Zone 1 and 2 are separated by the interface and the dividing boundary is a sharp one as shown in Fig 2.2. The boundary between zone 2 and 3, however, is not sharp. The physical properties of the molten aluminium and the electrolyte are listed in Table 2.1 [11]. The typical magnitudes of fluid velocity, temperature variations, and electromagnetic field strengths are listed in Table 2.2. [11].

Periodic fluctuations of cell voltage and anodic currents are obviously generated by deformations of the interface between electrolyte and the metal due to the large jump of

Table 2.1 Physical properties of molten aluminium and electrolyte [11].

(At 960 °C)			
	Zone 1 (Metal)	Zone 2 (Electrolyte)	Unit
Density	2.27×10^3	2.13×10^3	kg/m ³
Kinematic viscosity	5.2×10^{-7}	5.2×10^{-7}	m ² /s
Thermal conductivity	77.95	1.69	joule/s-k
Specific heat	1.09×10^3	1.66×10^3	Joule/kg-k
Thermal diffusivity	31.6×10^{-6}	0.48×10^{-6}	m ² /s
Permeability	$4 \pi \times 10^{-7}$	$4 \pi \times 10^{-7}$	henery/m
Electric conductivity	3.45×10^6	2.22×10^2	1/ohm-m
Magnetic diffusivity	0.2307	3.58×10^3	m ² /s
Coefficient of vol. exp.	-	10^{-4}	1/k

Table 2.2 Typical magnitudes of the fluid velocity, temperature variation, and electromagnetic field strengths[11].

	Zone 1	Zone 2	Unit
Velocity	0.1	0.1	m/s
Length	1.5	1.5	m
Temperature variation	-	10	K
Current density	10^4	10^4	Amp/m ²
Magnetic induction	10^{-2}	10^{-2}	weber/m ²

electric conductivity across the interface. Horizontal velocities in the electrolyte and metal associated with interface oscillation result in shear stresses and turbulence at the interface and losses in current efficiency. Magneto-hydrodynamic (MHD) instabilities can occur in some special situations, e.g. after anode change, or may be a general characteristics of a pot. For unstable pots the ACD is usually increased to reduce the periodic oscillations of the cell voltage. Therefore, the tendency to MHD-instability is strongly associated with higher specific energy consumption. Other MHD-phenomena like redistribution of current densities, flow field patterns and metal pad deformation after the anode change or perturbations due to sludge can result in undesired effects as well.

Aluminium industry tries to control the phenomena related to MHD-effects in the Hall-Heroult process by optimizing the bus bar design. For improving stability of the cell current distribution in anodes, cathodes, as well as in bus bars and the resulting magnetic fields are of special importance.

2.2 COMPUTATION OF TEMPERATURE, CURRENT, MAGNETIC FIELD, VELOCITY, MELT TOPOGRAPHY, AND CURRENT EFFICIENCY IN HALL-HEROULT CELLS

The task is completed in the following manner. First the temperature distribution is calculated which gives the ledge profile. The current and magnetic field must be calculated as a function of position in the cell, yielding the electromagnetic force distribution. Thirdly, the turbulent fluid flow equations are solved with this force distribution to yield the velocities and turbulence levels within the cell. The solution of the fluid flow equations yields the pressure distribution within the electrolyte and metal, from which, the topography of the electrolyte-metal interface can be computed. Finally, the rate of transport of aluminium to anodes, which causes re-oxidation of aluminium, and the current efficiency are calculated. The kinetic energy distribution within the electrolyte is computed with the help of turbulence in the cell.

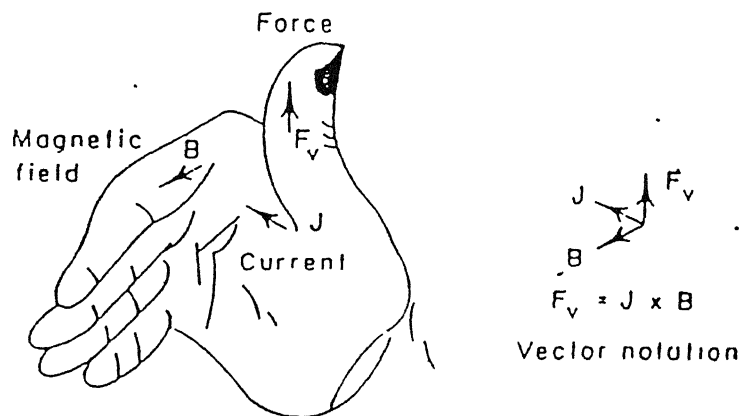


Fig. 2.1 Right hand rule gives force direction as a function of current and magnetic field [2].

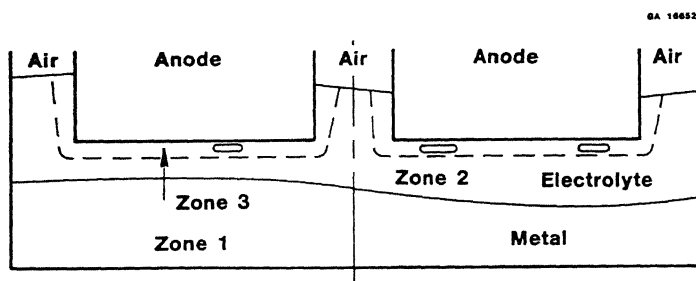


Fig. 2.2 Different zones in Hall-Heroult cell [11].

2.2.1 Temperature Distribution

Thermal phenomena influence the cell operation to a large extent. Current efficiency, specific energy consumption, fluoride emission, movements of fluids and frozen bath shape results are affected. Steady state computation of temperature distribution is useful for thermal cell design; but time evolution of temperature distribution is required in order to obtain certain knowledge about optimal cell operation. In this case, theoretical models must be capable of coping with changes in the cryolitic bath. Thermal model treats conduction of heat within the sides and bottom of the cell as two-dimensional heat flow problem. Resulting equations are solved through the use of a numerical procedure to determine temperature distribution across the cell lining and thickness of the formed ledge. It is found that the controlling factor of temperature in the cathodic block near the cell side is the cathodic bar cross sectional area. It is also noted that the frozen bath width has little significance on thermal balance, and what actually matters is its time of evolution due to its capacity for absorbing or bearing heat during the change of phase [12-17].

2.2.2 Electric Current Distribution

Electric current distribution in different regions of the cell is critical factor in the development of thermal and hydrodynamic phenomena. Electric currents along the bars generate the largest contributions to magnetic fields. The interactions of these fields with electric currents in the melts produce volumetric Laplace forces inducing movements in the fluids. Joule heat generated by electric current flowing through the cell can be calculated by computing resistivity and current distribution within the cell by application of Ohm's law.

The study of the electrical phenomenology can be divided into two central subjects:

1. Electric current and potentials in volumetric conductors (anodes, cathodes and melts)
2. Current distribution in bars (anodic and cathodic bus bars, anodic and cathodic bars)

Computation of local electric current distribution aims at knowing the potential drop in the anodes and the cathodes, electric current density in the melts and the corresponding Joule heat generation [18,19].

2.2.3 Magnetic Field

Once the current density distribution within the cell is determined, magnetic field strength and direction at any point can be determined by application of Biot-Savart law in integral form. There are three sources of magnetic field (MF) in the cell.

1. Electric currents in the bars (bus bars, anodic and cathodic bars, etc.)
2. Electric currents in volumetric conductors (anodes, melts and cathodic blocks).
3. Steel parts (cell shell), actually the demagnetization field.

Magnetic field originated from electric currents in the bars can be computed applying Ampere law to rectilinear conductors of negligible cross section area and finite length. MF from anodes, melts, and cathodes may be computed by integration of the volumetric electric current density flowing through them. MF from volumetric conductors can also be computed, solving the Laplace equation for scalar potentials. This is performed assuming that the MF from bars and from steel parts has nil curl in the region occupied by the melts [20,21].

2.2.4 Melt and Electrolyte Velocities

The mathematical description of the movements of the melts in the cell (cryolitic bath and molten aluminium) is an extremely complicated task. Two layers of viscous fluids are superposed; their movement is turbulent in certain regions of the cell. The cryolitic bath is agitated by the electromagnetic forces and by the movements of CO₂ and CO. Movements of the fluids affect heat and mass transfer in the cell, anodic current distribution, voltage stability, and as a consequence affects the current efficiency. Another important subject within the study of the movements of the fluids is the knowledge of the velocity distribution within the melts [18,19,22,23].

2.2.5 Melt Topography

Time averaged Navier-Stokes equations assume that the interface is a flat one and their solution yields a pressure distribution for the electrolyte and for the metal. In reality both the liquids have freely deformable surfaces and computed pressure distribution is exactly balanced by the hydrostatic pressure gradients developed as the

interfaces deform. It should be noted that curvature of the metal-electrolyte interface (a few centimeters over a few meters) is sufficiently small to permit the use of a rectangular coordinate system for the fluid flow equations. Simple force balances therefore yield the equation for the height of the interface 'h' with respect to an arbitrary reference position [18].

2.2.6 Current Efficiency

Computation of the velocity components, throughout the molten electrolyte and the metal, also yields the distribution of effective viscosity in the two liquids within the cell. From this distribution it is possible to calculate the distribution of eddy (mass) diffusivity throughout the electrolyte. The rate-controlling step in aluminium transport/re-oxidation sequence is transport of aluminium through a concentration boundary layer at the metal/electrolyte interface [18].

$$\text{Current efficiency pct} = 100 \left\{ 1 - \frac{\text{Mass transport rate of Al to anodes}}{\text{Al production rate expected from Faraday's law}} \right\}$$

2.3 FACTORS AFFECTING THE FLUID DYNAMICS OF HALL-HEROULT CELL

2.3.1 Effect of Age of Cell

Measurements have been made over a period of 2 years in a 130-kA Invergorden cell by Bradley et al. [24]. Velocities were measured using the iron rod dissolution technique developed by Johnson [25]. The method yields both the magnitude and the direction of metal flow at each rod location.

Young cells have more or less similar flow patterns, but there are wide variations in older cells. Thus, only for the new cells (<150 days) flow can be characterized with some certainty. Variation is largest for the cells in the 400-900 days group. The new cells have a vortex at each end. Metal flow is higher on the upstream side, and largest at the corners. A central ridge is generally present on the cathode under the crustbreaker, and this may be high enough to partially divide the metal. Group of young cells (150-

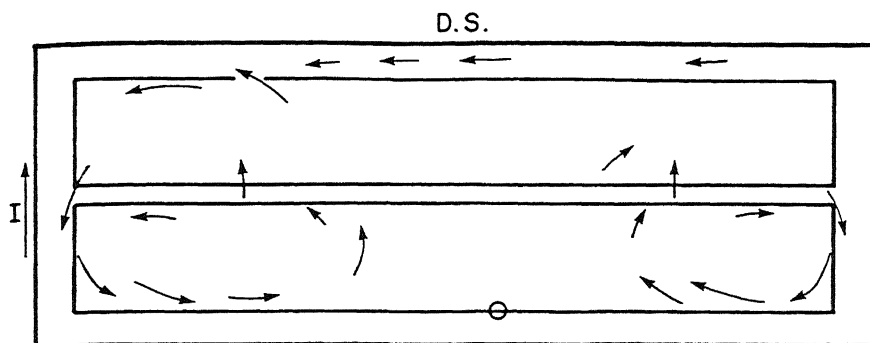
400 days) shows a pattern similar to, but less distinct than, that seen for first set. The highest speeds are still in the vortices at the upstream corners. No general pattern is deduced for the flow in the downstream half of the cell. The middle-aged cells (400-900 days) show greater variations than the two previous groups, with each cell having its own pattern. The group of old cells (>900 days) again show wide variations but a clear trend is seen, when the velocities are averaged. Flow patterns for cells of different age groups are shown in Fig. 2.3. The freeze profiles for two age groups are also shown in Fig. 2.4.

2.3.2 Effect of Cold Anode

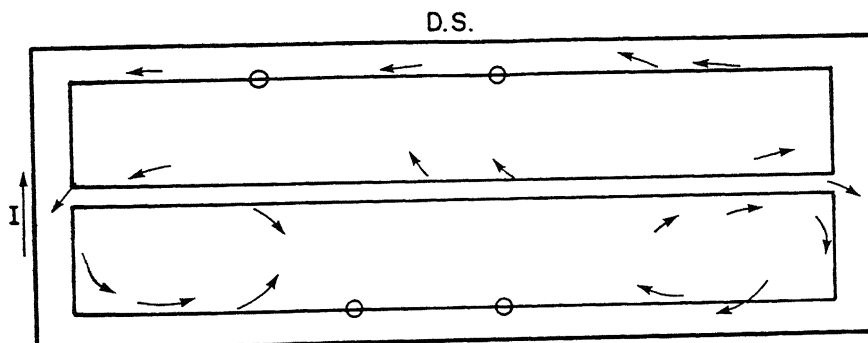
Three cases, typical for a cell, are analyzed by the steady state transient calculation [5]. Case 1, is change of the corner anode. This is compared with case 2 in which an anode in the middle row is changed. The cell under consideration is a 165 kA pre-bake cell in head to head configuration with four risers, 20 anodes and a symmetric bus bar system.

Horizontal current densities in the liquid metal for cases 1 and 2 are shown in Fig 2.5. As expected from the electrical boundary conditions, horizontal currents due to missing vertical current of interrupted anode are spread over the largest part of the liquid metal. Vertical magnetic flux as shown in Fig 2.6 for case 1, shows a typical quadrant structure with an average positive offset of about 25 G caused by the adjacent pot line. Horizontal Lorentz forces in the liquid metal due to anode interruption are strongly affected by this offset as shown in Fig. 2.7 for both cases 1 and 2. Magnitude of the additional horizontal forces is smaller than the vertical Lorentz forces, caused by horizontal currents and horizontal magnetic flux. Nevertheless, their influence on velocity and horizontal interface height is much stronger due to ratio of horizontal to vertical length scale as shown in Fig. 2.8 for velocity and Fig. 2.9 for metal pad deformation for both cases. The forces from additional horizontal magnetic field, mainly due to missing vertical current below interrupted anode and vertical current density are of the same magnitude as well. Their orientation is such that they are

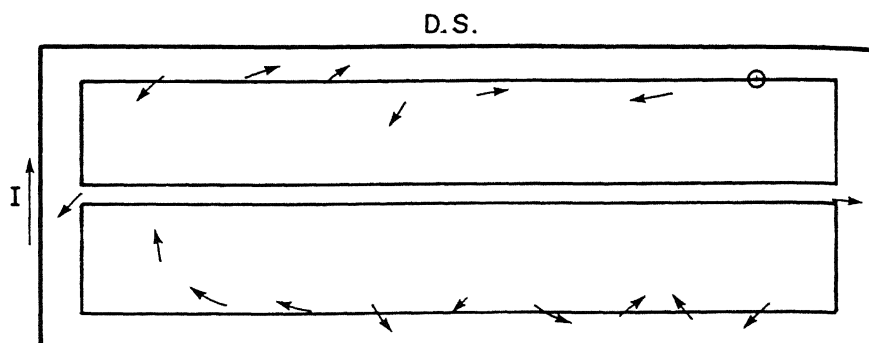
METAL FLOW IN CELLS <150 DAYS OLD



METAL FLOW IN CELLS 150-400 DAYS OLD



METAL FLOW IN CELLS 400-900 DAYS OLD



METAL FLOW IN CELLS >900 DAYS OLD

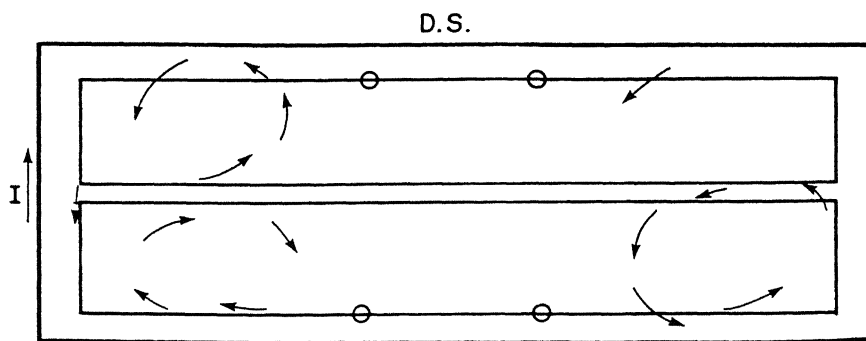


Fig. 2.3 Flow patterns at different ages of the cell [24].

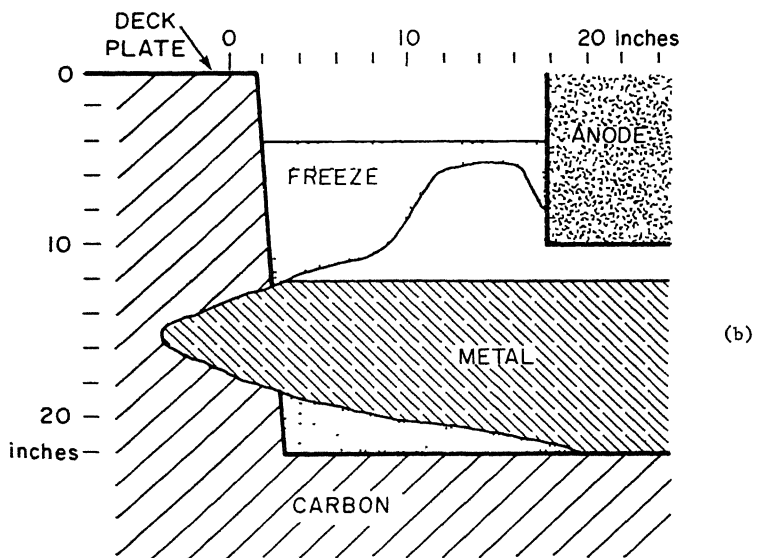
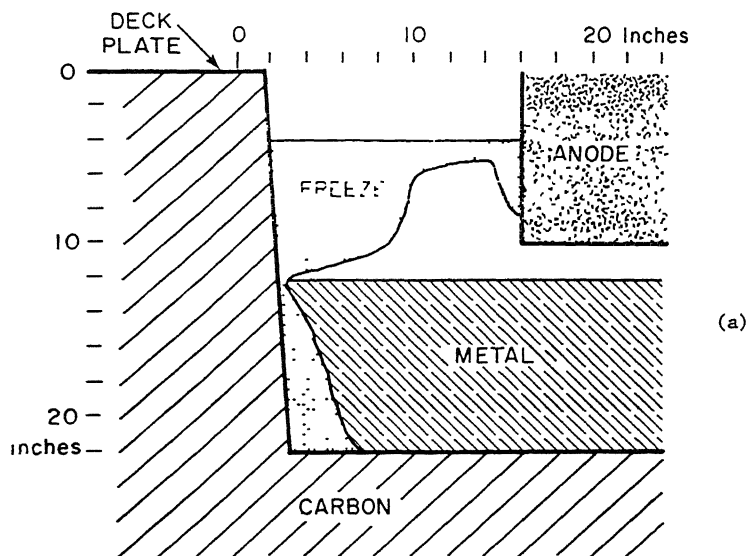


Fig. 2.4 Freeze profiles (a) <150 days (b) >900 days [24].

directed away from the interrupted anode. Their influence on the metal pad deformation is only local because this force field is similar in both bath and liquid metal.

2.3.3 Effect of Anode Geometry

Anode Geometry determines size and shape of the channel/cavity formed between two anodes, and anodes and side walls. Gaps between two anodes, and anodes and side walls are increased as width of anodes decreases. Cross-sectional area of the anodes may be preserved by increasing length of these anodes. Thus if anodes are lengthened into side channels, distance between the anodes and side wall decreases. This is because melt is forced out of the wider slots with a reduced velocity and turbulence level. The result would be a reduction in local heat transfer on the side walls near the slots. At the end walls changes in velocities are similar but turbulence is less affected, hence heat transfer at the end walls is not reduced much as that on the side walls. Anode tilt drastically affects the behavior of the bubble layer so it reduces the anode effect. A tilt of a fraction of a degree is sufficient to induce significant buoyancy driven motion of gas bubbles, which is responsible for anode effect [26,27].

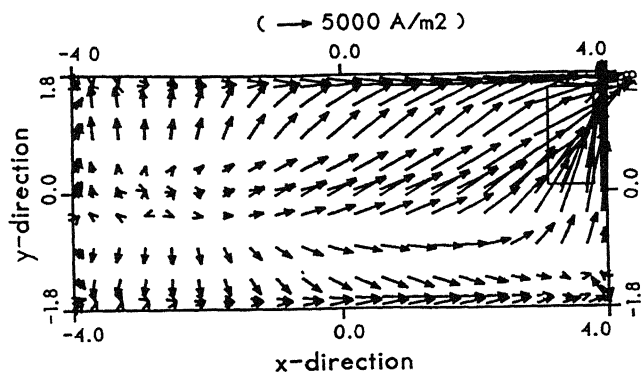
2.3.4 Effect of Anode Cathode Distance (ACD)

Effect of ACD has been investigated by varying spacing between anode surface and cathode face in a full-scale physical model developed by Fortien et al. [27]. Velocity decreases when ACD is reduced. Larger ACD causes a strong damping of the oscillations of metal pad. For the unstable cells ACD is usually increased to reduce the periodic oscillations of the cell voltage.

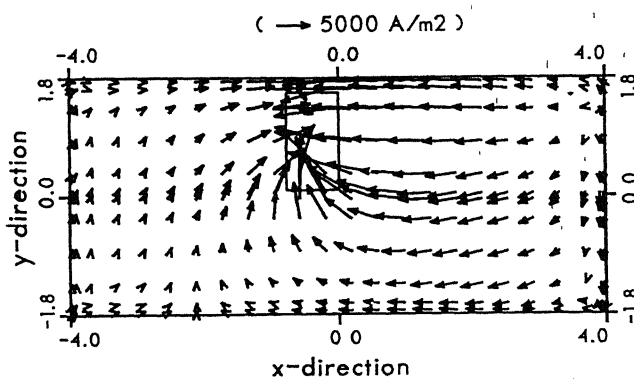
2.3.5 Effect of Ledge Shape

State of ledge plays an important role in determining operating conditions of large aluminium reduction cells. The functions of the ledge are:

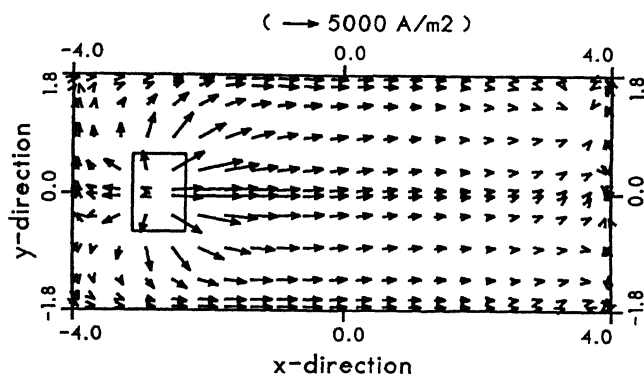
- To help in keeping the metal pad still and thereby maintain stable cell operation and high current efficiency.



(a)



(b)



(c)

Fig. 2.5 Horizontal currents in liquid metal for interrupted anodes: (a) corner anode, (b) middle anode, (c) sludge formation [5].

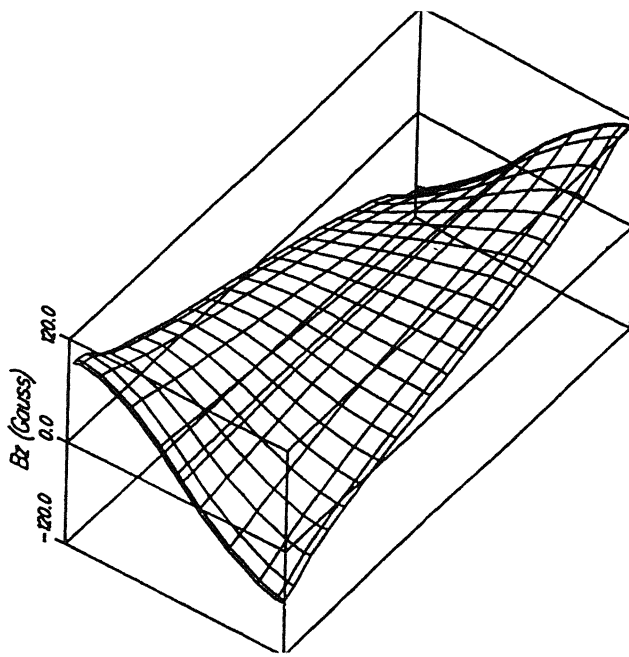
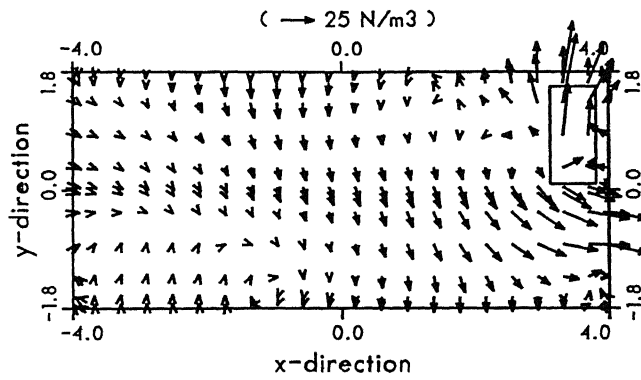
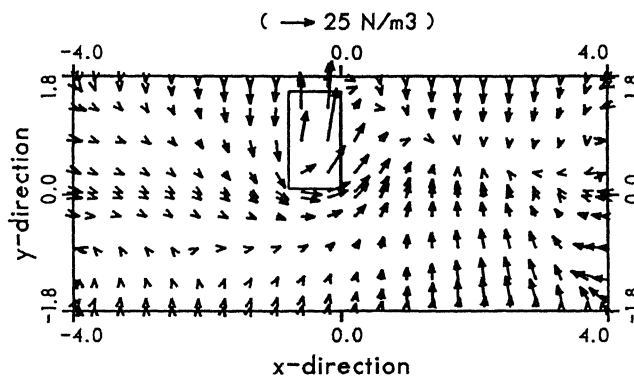


Fig. 2.6 Vertical magnetic flux, case 1: interrupted corner anode [5].



(a)



(b)

Fig. 2.7 Additional horizontal forces in the liquid metal for two cases: (a) due to an interrupted corner anode (b) interrupted middle anode [5].

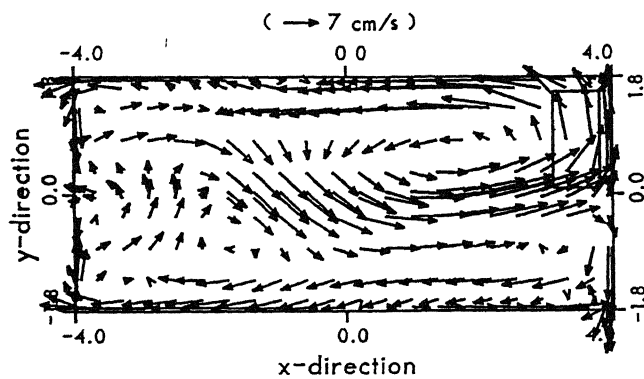
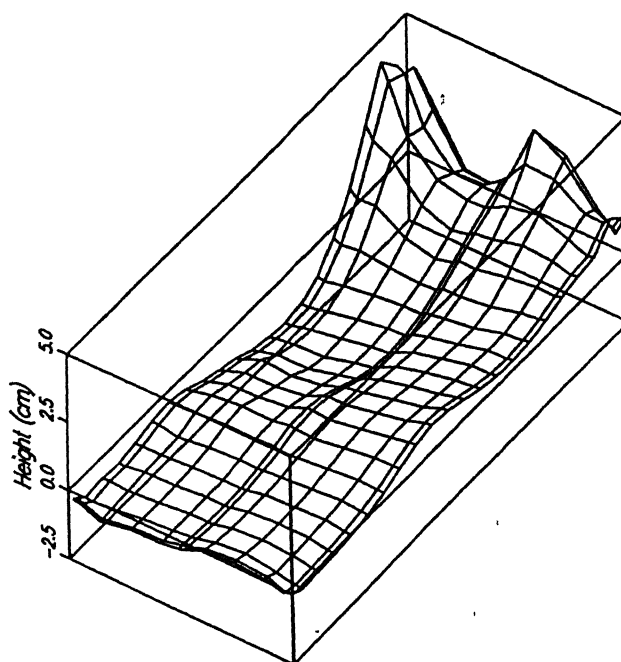
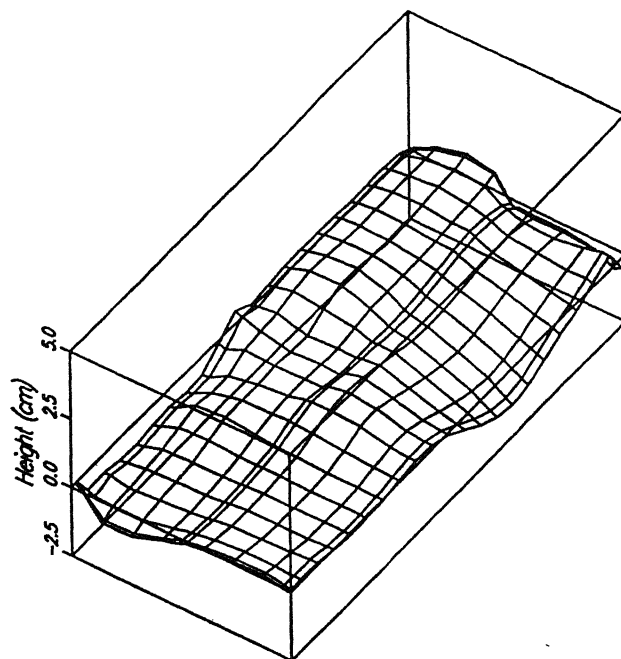


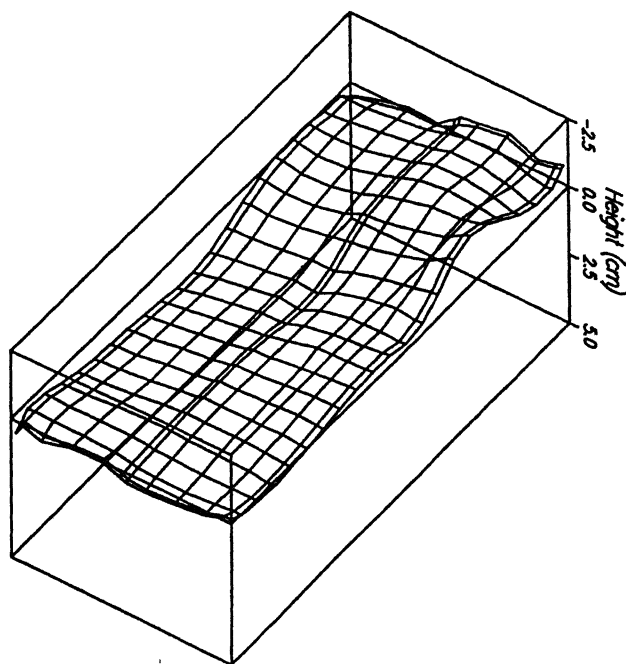
Fig 2.8 Metal velocities in case of interrupted corner anode [5].



(a)



(b)



(c)

Fig. 2.9 Metal pad deformation for interrupted anodes: (a) corner anode (b) middle anode (c) sludge formation [5].

- To ensure that the permanent side wall material is not exposed to erosion by bath and metal pad circulation, especially during periods of cell disturbances, and this gives long side-wall life.
- To allow thermal self-regulation of the cell during periods of excessive power input such as anode effects.

The effect of the ledge profile on cell current efficiency is shown in Fig. 2.10. The highest current efficiency (90%) is obtained when the ledge confines the metal pad to within projected shadow of the anode and sloped steeply down to a line beneath the edge of anode. It has also been confirmed that a good ledge profile stabilizes the metal pad interface for the small and the large cell disturbances [1]. When freeze profile does not limit the metal pad to the anode shadow, the metal surface becomes unnecessarily large and surface extending beyond the anode shadow experiences high circulation speeds of bath in side wall region that are induced by the anode gas flow. This results in lower current efficiency as more metal surface is exposed beyond the anode shadow. It has been found through voltage stability studies that unstable cells generally have ledge profile with lateral toe extending towards the center of cell, as shown in Fig. 2.11. This toe-insulated part of the cathode reduces cathode area, and it is speculated that this creates an increased horizontal component of current flow in the metal/electrolyte interface. This locally reduces inter-polar distance, which results in pot voltage instability and reduced cell current efficiency. Reduction in cathode area also increases cathode current intensity and thus the cathode voltage drops, and also cells voltage drop.

Cell side walls should be designed such that:

- Isotherms in side walls and the cathode blocks give a steep ledge profile within the metal pad; limit the metal pad to the anode shadow; and avoid any lateral ledge extension under the shadow.
- The ledge is as thick as possible so that it can withstand large cell disturbances without leaving the permanent side walls material exposed to erosion by the bath and metal pad circulation.

- Finally, to ensure long side walls life, periods of cell instability should be detected and the cell restored to normal operation as quickly as possible.

2.3.6 Effect of Cell Current

Evans et al. [28] have suggested that a balance between electromagnetic forces, drag forces and pressure forces determine the electromagnetically driven flow in Hall cells. Suggestion lead to conclusions that melt velocity should be proportional to electromagnetic driving forces, and thereby square of cell current. Figure 2.12 shows measured wood's metal velocity, at a point, in the model as a function of current passed through it. If it is assumed that model mimics behavior of the real cell, then the predicted behavior is seen to be correct.

2.3.7 Effect of Bus Bar Design

Velocity and magnetic field have been computed and measured for three different bus bar designs: (i) the end riser design, (ii) the quarter riser design, and(iii) the novel riser design. Bilek et al. [26] have shown that effect of bus bar design change (the quarter riser compared to the end riser) significantly reduces magnitude of MHD force on the electrolyte. However, as the bubble flow dominates, the overall effect is minor. Table 2.3 shows that bus bar design changes have only a small effect on current efficiency because current efficiency is already high, and gas evolution affects the flow profile.

Evans et al. [9] have computed velocities in the metal and electrolyte, as shown in Fig. 2.13 for the three different bus bar designs. Flow in the novel riser design has greater symmetry than that of conventional cells. In the metal pool, the current “fringes”, i.e. there is a tendency for the current to flow outward through cell walls, as well as vertically downward. Since the three designs have identical internal current distributions, there is little variation in stirring of aluminium. In contrast, within the molten electrolyte there is little fringing of current and stirring effects due to internal currents are less significant. This can be seen in Fig. 2.13 where the novel riser design results in more bowing of interface than the end riser design while quarter riser design shows least bowing of the three designs. Current efficiencies of three riser designs are

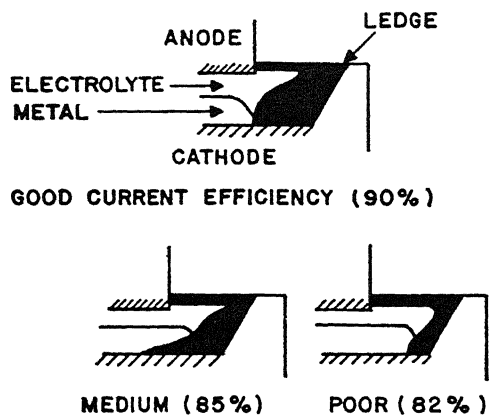


Fig. 2.10 Ledge profile verses cell current efficiency [1].

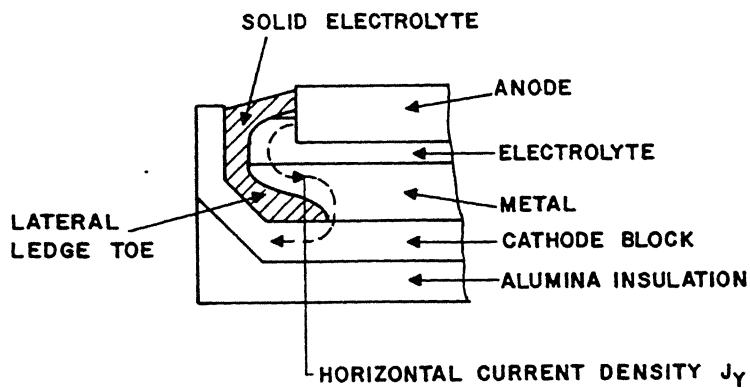


Fig. 2.11 Effect of ledge lateral toe on current flow [1].

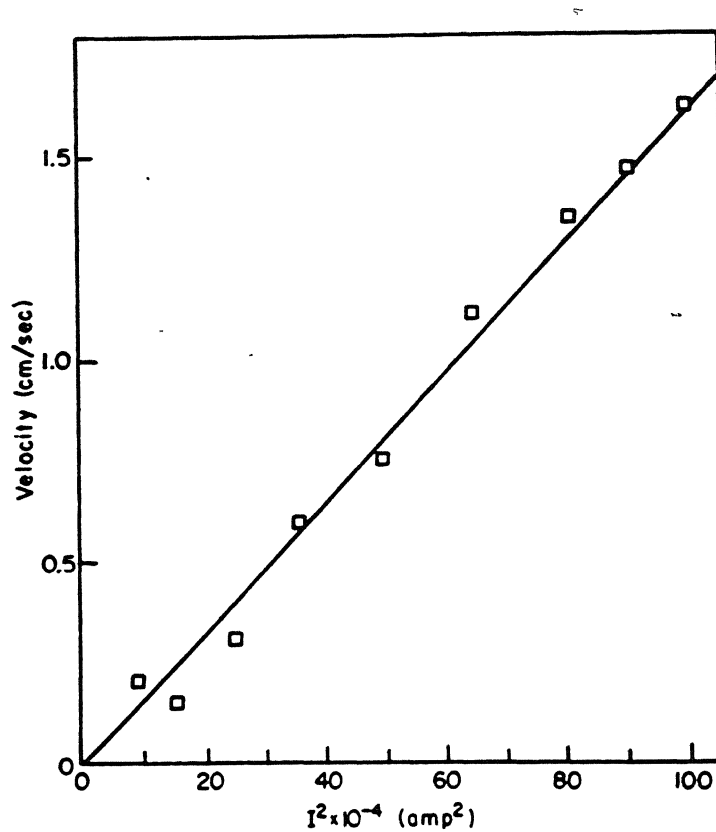


Fig. 2.12 Measured velocity at a point in the Wood's metal verses the square of the current through the model [28].

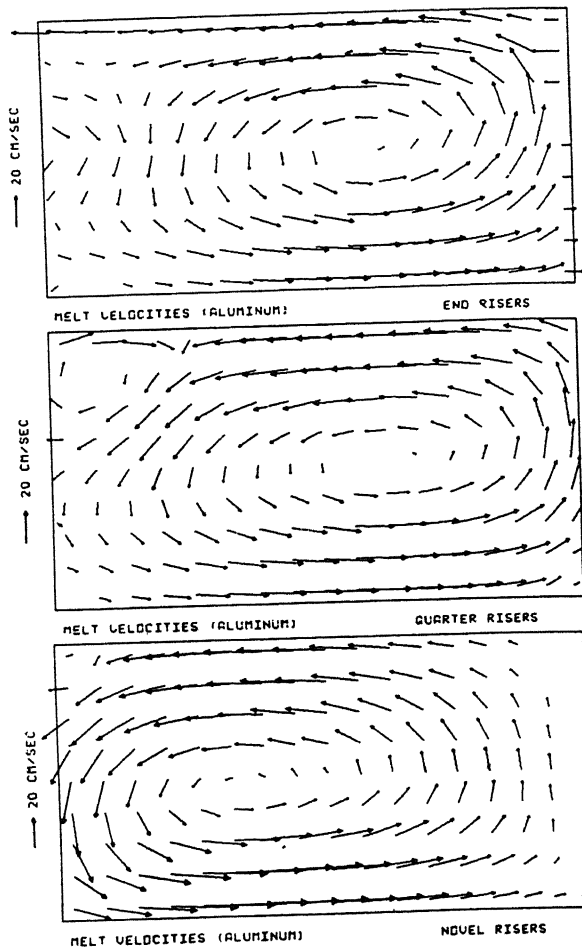


Fig. 2.13 Computed metal velocities for three cells differing only in design of their risers [9].

given in Table 2.3. It appears that the complex circulation pattern of the end riser cell, with its high velocity gradients, results in more turbulence in the electrolyte, a greater transport of aluminium and lower current efficiency, than the quarter riser or novel riser designs. The novel riser design does not yield a current efficiency significantly different from that of the quarter riser design.

Anode bus and anode rods make a substantial contribution to magnetic field within the cell in contrast to cathode (“ring”) bus, as these conductors are not shielded by steel shell of the cell. It might be conjured that cell performance is improved by shielding the anode bus. Model predicts that the shielding is effective in case of the end riser cells but reduces current efficiency of the quarter riser cell. It is stressed that absolute values of stirring forces are not significant as far as velocity and current efficiency are concerned, but rather their variations. Thus, while screening the anode bus reduces total magnetic field in all cases, in case of quarter riser design it simultaneously enhances its variation a well.

Table 2.3 Computed current efficiencies for various cell modifications [9].

Bus Bar Design	Unshielded Anode Bus and Rods	Shielded bus, Unshielded Rods	Shielded bus, Shielded Rods
Quarter riser	93.8 %	92.9 %	94.9 %
End riser	88.6 %	90.3 %	92.7 %
Novel riser	93.4 %	93.4 %	95.5 %

Tabereaux et al. [29] have measured velocities in both Soderberg and prebake reduction cells using iron rod desolution technique.

Results for different cells are shown below:

VS Soderberg cell:

The following trends in the metal pad circulation patterns are evident as in Fig 2.14:

- One large clockwise metal flow pool.
- Metal velocities are uniform near the center of the cell.

- The highest and lowest metal velocities occur near the corner of the cell.

HS Soderberg Cell:

Metal pad velocities measured at various locations in 100 kA HS Soderberg cell (end-to-end) are shown in Fig. 2.15. The following trends in the metal pad circulation patterns are evident:

- There is one major counterclockwise metal flow pool.
- Anomalies or differing metal flows at some locations are thought to be caused by an excessive accumulation of the muck in the cathode cavity of the cell.

End Riser Prebake Cells:

150 kA Prebake Cell: Results of metal velocities measurements in a 150 kA prebake cell with the end anode riser bus are shown in Fig. 2.16. The following trends of metal pad circulation patterns are evident:

- Two major metal circulation pools are evident as shown in Fig. 2.16. Metal flows from center of the cell toward ends of the cell, on downstream side of the cell. Metal circulates around ends of the cell toward side wall on the upstream side of the cell.
- The highest metal pad velocities are generally found on the upstream side of the cell as the metal approaches side walls after passing around the end of the cell. The lowest metal pad velocities are generally found in the center of the cell as two metal pools converge.

76 kA Prebake Cell: Results of metal velocities measurements in a 76 kA prebake cell with the end riser bus are shown in Fig. 2.17. The following trends in the metal pad circulation patterns are evident:

- Four major metal circulation pools are observed as shown in Fig. 2.17. In the center work area of the cell, the metal flows to both ends of the cell. At the ends of the cell, the metal circulates around the ends towards the center of the cell on both the upstream and downstream sides of the cell.

- The highest metal pad velocities are generally found near ends of the cell as the metal approaches the side wall after passing ends of the cell. The lowest metal velocities are found near the center of the cell as the metal pools converge.

Quarter Riser Prebake Cells:

150 kA Prebake Cell: Results of metal velocities measurements in a 150 kA prebake cell with the end riser bus are shown in Fig. 2.18. The following trends in the metal pad circulation patterns are evident:

- Four major metal circulation pools are observed as shown in Fig 2.18. In the center of cell the metal flows across the cell from downstream to upstream side of the cell. On upstream side of the cell, the metal flows from the center towards the quarter riser where the metal flows across the cell from upstream to downstream sides of the cell.
- The highest metal velocities are generally found along the upstream side of the cell and the lowest velocities are found on the downstream of the cell.

Each design of reduction cell has a different and distinctive metal circulation pattern. The lowest metal pad velocities are found near the center of the cell where the metal pools generally converge.

Computed and measured velocities and magnetic fields in a Kaiser cell of the 185 kA cell are shown in Fig. 2.19[9].

2.4 INSTABILITY IN ELECTROLYTE/METAL INTERFACE

Continuous measurements of the cell voltage, anode current and magnetic field during quasi-stable and unstable operations, demonstrate typical interface deformation mode [30]. A large DC current (50 ~200 kA) passes through the system and generates a strong magnetic field. The flux density reaches 200~300 Gauss at its highest location in high current cells. Thus, the major force acting on the melts is a body force generated by the internal electrical current and magnetic field. Three possible waves are investigated [31].

2.4.1 Types of Metal Pad Waves

2.4.1.1 Capillary Wave: The surface tension of liquid aluminium contacting molten cryolite is around $\beta = 0.52 \text{ N/m}$. So the capillary constant for surface becomes [31]:

$$A = [2\beta/g(\rho_2-\rho_1)]^{1/2} = 0.023 \text{ m}$$

where ρ_1, ρ_2 are densities of the bath and metal, respectively.

This length is much smaller than a typical cell dimension, indicating that the wave is a ripple on the interface surface, and plays a minor role in slow fluid motion with a wavelength over a 1 m.

2.4.1.2 Short Period Wave: When the anode-cathode separation which characterizes cell operation is extremely small in a localized area, or there exists a shorting of current between the anode and liquid metal in the small area, a sharp downward spike of voltage on the continuous cell voltage recording chart is obtained. Period of this spike varies from a couple of seconds to 20 seconds. It appears that the mechanism of this motion is related to the intense localized electrical current. This local current concentration in the molten bath disperses when current flows into highly conducting liquid metal. It is known that such a concentrated electrical current generates a circumferential magnetic field, which interacts with current and generates a pinch force. The dependency of the period on current density is shown in Table 2.4.

Table 2.4 Dependency of period on current density[31].

Local current density (Amp/cm ²)	1	2	4	6	8	10
Period (sec)	20.9	10.5	5.2	3.5	2.6	2.1

2.4.1.3 Long Period Wave: This wave is essentially an internal gravity wave. In an aluminium reduction cell, the electromagnetic force perturbs this wave. Thus, a pair of coupled equations, one for motion and another for electrical potential distribution describes the wave motion and current distribution.

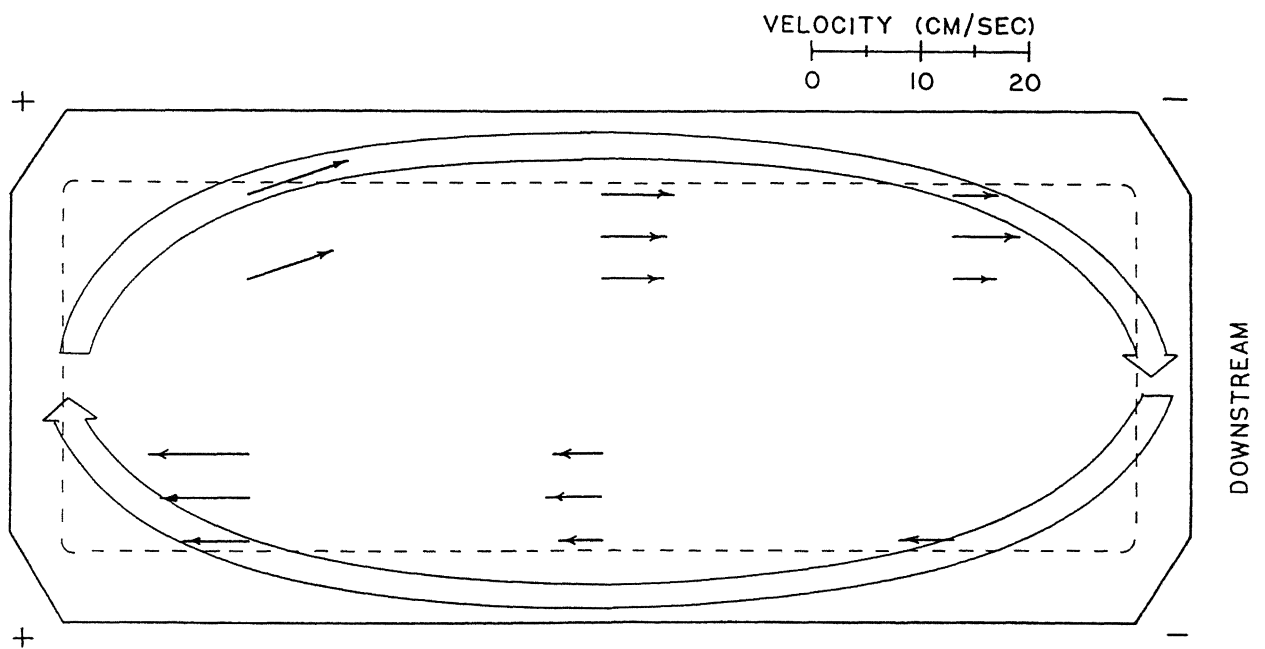


Fig. 2.14 Metal flow velocities in 110kA V.S. Soderbreg cell [29].

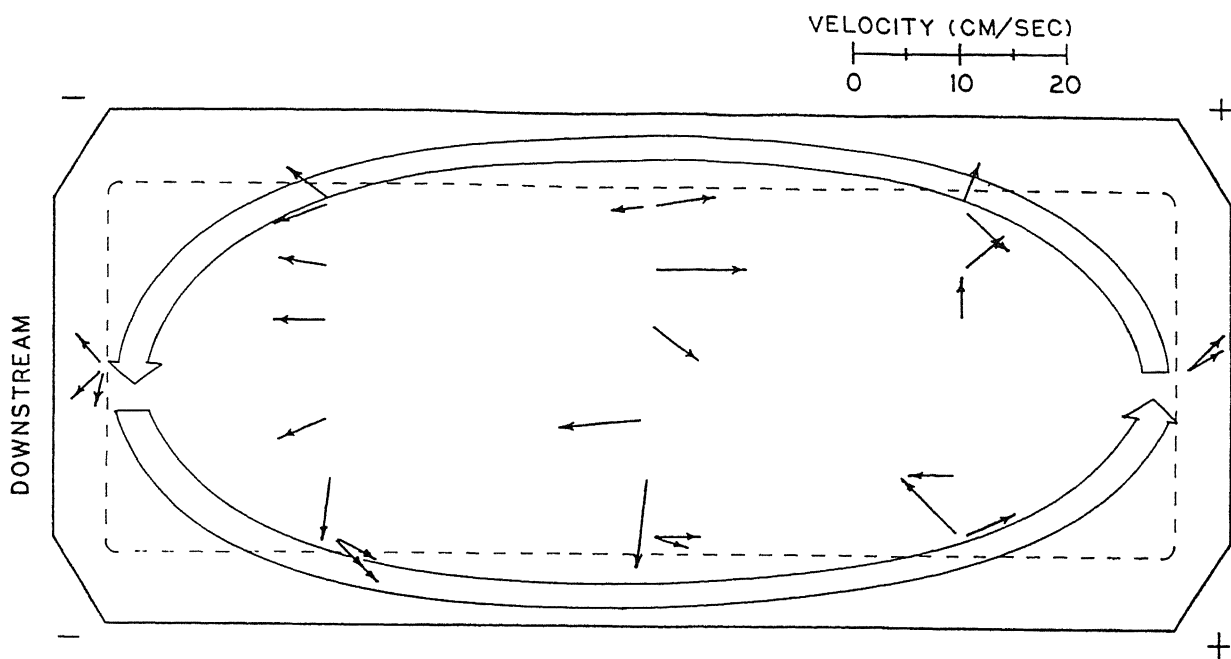


Fig. 2.15 Metal flow velocities in 100kA H.S. Soderbreg cell [29].

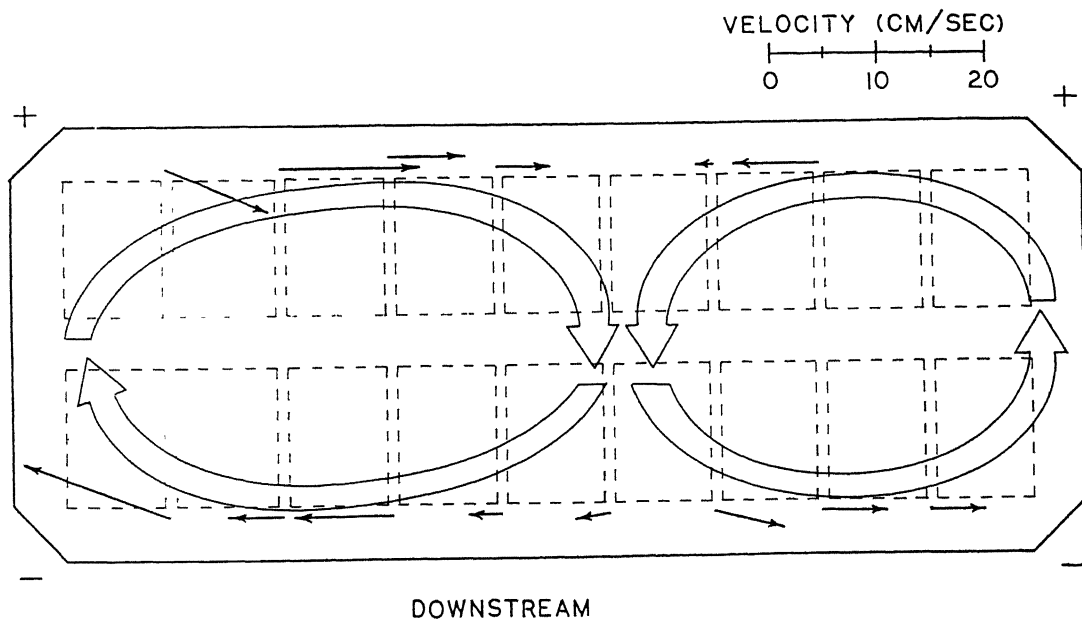


Fig. 2.16 Metal flow velocities in 150 kA end riser prebake cell [29].

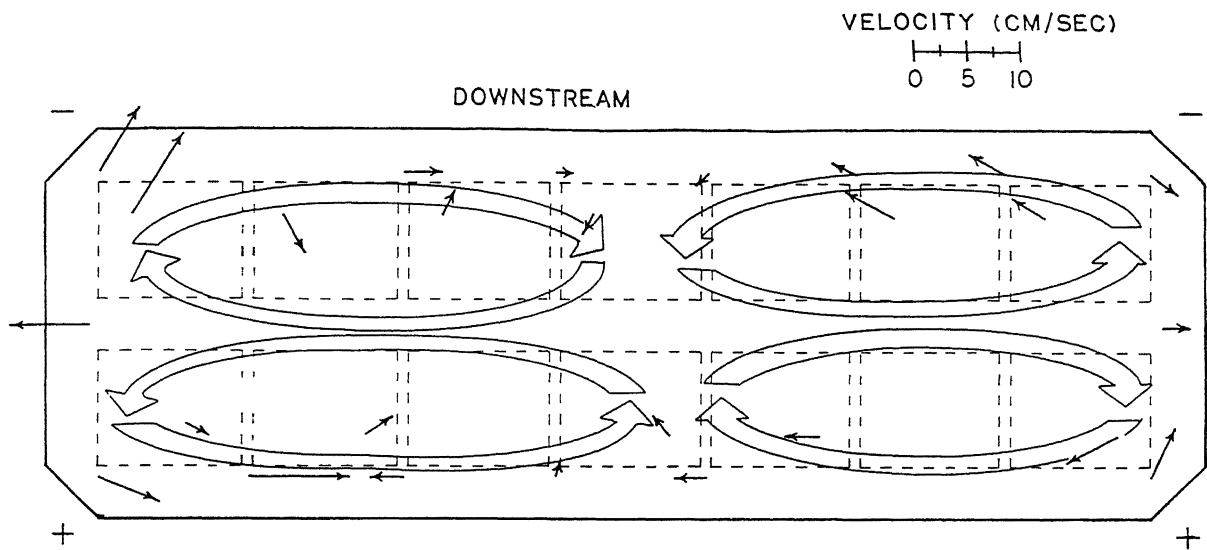


Fig. 2.17 Metal flow velocities in 76 kA prebake cell [29].

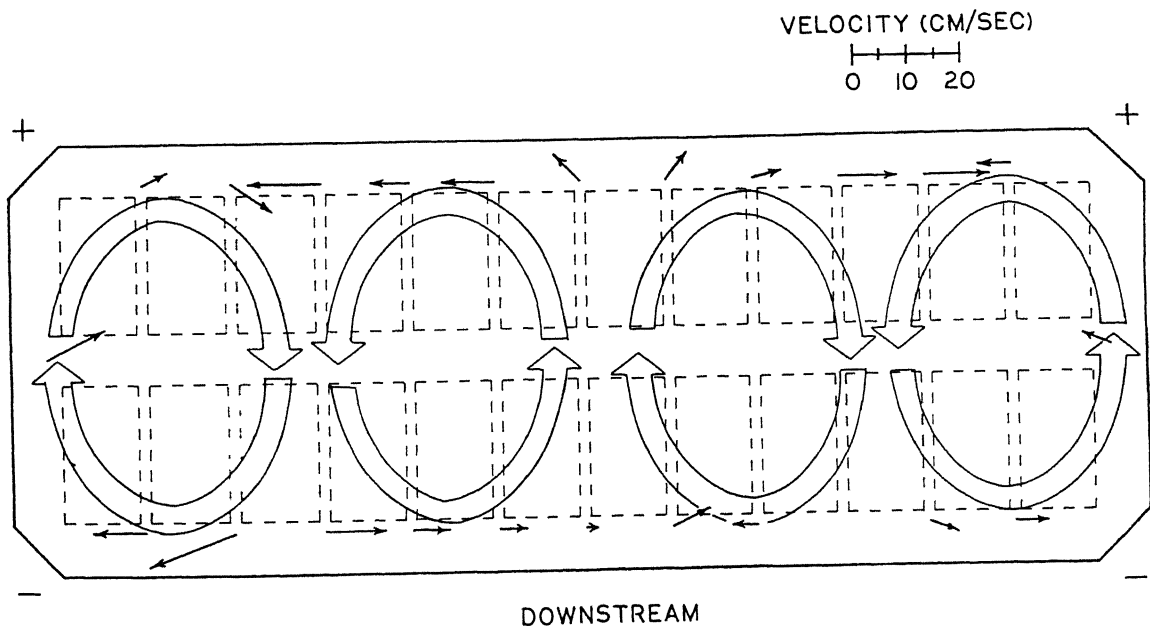


Fig. 2.18 Metal flow velocities in 150 kA quarter riser cell [29].

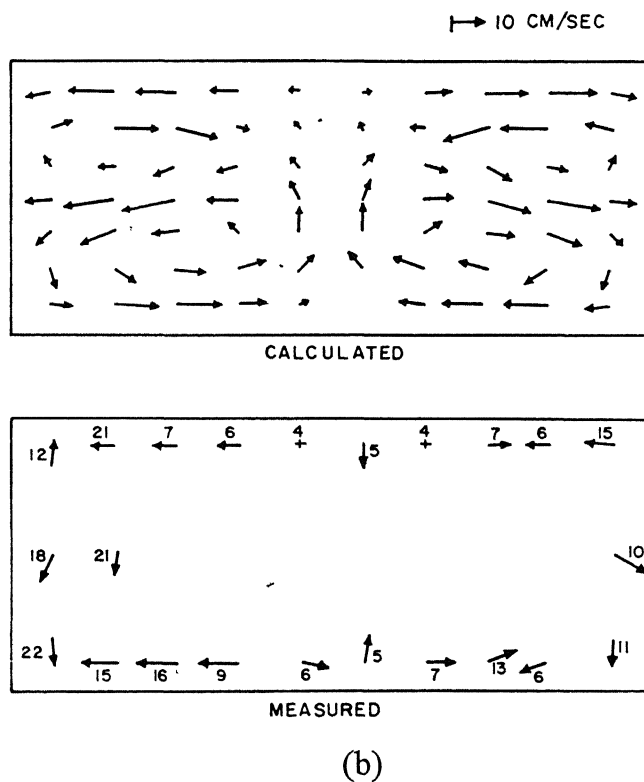
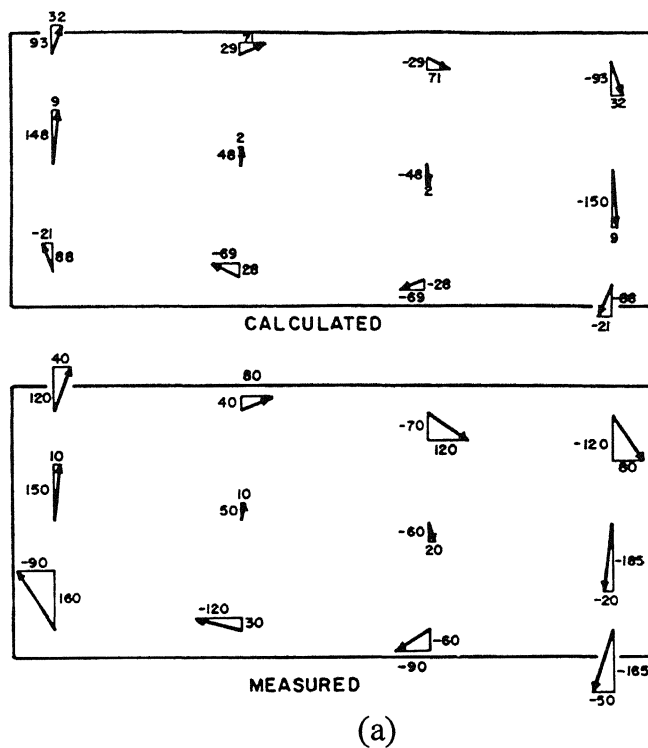


Fig. 2.19 Computed and measured (a) magnetic fields (b) and velocities within molten aluminium of the 185 kA Kaiser cell [9].

2.4.2 Application of Interface Wave Analysis in Pot Development

It is obvious from the above analysis that the vertical magnetic field is a major source of perturbation. This vertical component also generates a convex interface surface in the end riser pot by interacting with horizontal current in liquid metal. Thus, a practical requirement for the best bus arrangement is to reduce this vertical component. Distribution pattern of magnetic field is more important than the maximum intensity of the field, because the stability, or in other words, the melt flow in a cell depends more on curl of magnetic field rather than its magnitude. This fact indicates a possibility of increasing the pot stability in existing reduction line without major alterations in the bus bar arrangement. Observations made by researchers indicate that under certain circumstances, the electrolyte/metal interface may be stationary. This state comes about when the oscillations are damped out completely. In the fluids, both the viscosity and the electrical resistance provide damping. It is found that the electromagnetic damping effect is stronger than the viscous damping effect [31].

The discussion above leads to the conclusion that the deformation of the cryolite/aluminium interface is greatly affected by horizontal currents in the aluminium. It, thus follows that cell design, which minimizes such currents, should yield flat interface.

2.5 PRINCIPLE OF VELOCITY PROBE

The velocity probe developed by Ricou and Vives [32] operates on the principle that a magnetic field generates an electric field (i.e. a voltage gradient) within a conductor moving through the MF. The MF is generated in the probe by a small permanent magnet, and voltage gradient is sensed by the exposed tips of copper leads immersed in the conductor flow past the magnet.

According to the Faraday's law of electromagnetic induction, the induced emf equals the rate of change of magnetic flux.

$$\text{Induced emf} = e = \int \mathbf{E} \cdot d\mathbf{l}$$

where \mathbf{E} is induced electric field. This electric field is non-electrostatic in origin. The emf produced by a conductor moving in a magnetic field (wood's metal works as moving conductor in model cell) is given by

$$e_m = \mathbf{v} \times \mathbf{B} \cdot \mathbf{l}$$

where \mathbf{v} is velocity, \mathbf{B} is magnetic field produced by probe's magnet, and \mathbf{l} is separation between two tips of probe. The above equation may also be written as:

$$e_m = vBl \sin \theta$$

where θ is angle between velocity and magnetic field.

The velocity probe is responding to two voltage gradients. The first of these is the voltage gradient produced by metal movement in the probe's magnetic field and the second is the voltage gradient resulting from the passage of current through the melt; the former is only a few percent of the latter. The emf due to current flow is given by applying the Ohm's law.

$$e_i = R \cdot i$$

where R is electrical resistance of metal between two tips of probe, and i is current component parallel to line connecting the probe tips.

The velocity probe also gives some zero error value, known as cell constant, which may be generated by instrument or by thermal effect or by natural convection of melt or a combination of the three factors. Thus the net emf between the tips is a sum of all three emfs

$$e_{\text{net}} = e_c + e_i + e_m$$

$$e_{\text{net}} = a + b \cdot i + c \cdot i^2$$

where a , b , and c are constant parameters.

2.6 CONCLUDING REMARKS

Many researchers have developed mathematical models to compute thermal profiles, current distribution, magnetic field, fluid velocity, and electrolyte/metal interface topography of Hall-Heroult cell. But these models are not complete without validation by the experimental results. Some researchers, with very few alternative of

operating variables and designs, have measured velocities in actual Hall cells. The measurement of magnetic field in an actual cell is a difficult task due to the high operating temperature, which the Hall probe can not withstand. Hence, the alternative is a low temperature simulated model of the Hall cell. Banrjee et al. [33] and Lee et al. [28] have measured velocity and magnetic field in low temperature simulated Hall cells using wood's metal as a single fluid. Though the experimental data are not always sufficient to validate the mathematical models, they provide valuable insight into the behavior of real cells. The existing models may be valuable building blocks from which a complete comprehensive model can eventually be constructed to predict the magneto-hydrodynamics in operating Hall cells. The present investigation involves a detailed experimental study to generate data for various operating conditions and design parameters.

PRESENT INVESTIGATION AND ITS SCOPE

In present scenario, aluminium industry has higher energy consumption rate, 12.9 kWh/kg, against the theoretically possible value of 6.2 kWh/kg of aluminium produced. Main reasons for lower energy efficiency are directly related to higher voltage drops in different parts of the cell. The poor magneto-hydrodynamic (MHD) design of the cell is also responsible for increase in energy efficiency by producing excessive turbulence at the metal/electrolyte interface.

One important challenge before the cell operators and technology experts is to get a microscopic look of the factors, which are responsible for the metal/electrolyte interface oscillations, and then set the operating conditions with feasible economical changes in the cell such that the oscillations are the least. The oscillating interface causes short-circuiting of the anode and the metal pad, which creates major problems, like erosion of the cathode carbon refractory by friction as well as by carbon dissolution, and melting of protective ledge. These factors are also responsible for reducing energy efficiency of the cell.

In the past, several investigators have attempted to investigate the interfacial phenomena occurring in the cell using direct/indirect experimental methods, as well as, the approach of mathematical modeling to predict temperature and current distributions, magnetic field, velocities, and topography in the cell. Often trial and error methodologies involving frequent changes in the cell design, specially the bus bar design and other operating conditions have been used. Mathematical modeling approach suffers due to non-availability of experimental data to validate them. Thus, there is a need for generating reliable experimental data.

The Department of Science and Technology (DST) has sponsored a research project to study the magneto-hydrodynamics in the electrically driven melt flow in general, and in Hall-Heroult cell, in particular. Magneto-hydrodynamic studies essentially

involve mathematical modeling of cell phenomena to predict current distribution, temperature profile, magnetic field and velocities in the metal and the electrolyte as a function of the various operating variables. To validate the mathematical model developed in this project appropriate experimental data are to be generated. A laboratory scale low temperature simulated Hall cell has been constructed to collect experimental data related to the current, magnetic field, and velocity distributions.

Thus, the present investigation essentially involves a laboratory scale low temperature simulated Hall cell which is run under conditions closer to those normally employed during aluminium extraction to study the effect of various designed and operating parameters on current distribution, magnetic field and fluid flow. The laboratory scale low temperature simulated model of Hall cell employs wood's metal as a single fluid (m.p. $\cong 70\text{ }^{\circ}\text{C}$) which simulates the electrolyte in the actual cell. The present investigation consists of several parts as given below.

- The simulated Hall cell, only half portion of an actual Hall cell, having 1/10 size of an actual industrial cell has been designed and fabricated. It is having six anodes arranged in two rows operating at a total current of about 500 Amp (current density of about 0.9 Amp/cm^2), very close to the current density employed in Hall cells (0.7 to 1.2 Amp/cm^2).
- Temperature distribution is measured with the help of a thermocouple. Current distribution in the cell is estimated from the measured value of emf drops between two points.
- Magnetic field is measured for different operating conditions with varying current density, anodes configuration, anode cathode distance (ACD), and bus bar design change. The two bus bar designs used here are: (i) the end riser design, and (ii) the quarter riser design. The magnetic probe based on Hall effect is used. It is capable of measuring all the three components of magnetic field simultaneously.
- The fourth component of this study involves designing and fabrication of a two-direction velocity probe, and establishing a calibration procedure. The concept

used for the velocity probe is based on Faraday's law of electromagnetic induction. The probe design used here is similar to the one used by Ricou and Vives [32]. Some modifications however have been incorporated to improve the quality of measurements. The calibration apparatus consists of a rotating pot, the speed of rotation of which is precisely known.

- Measurement of velocity in the melt is carried out using the velocity probe at several locations under different operating conditions.

It is hoped that the data generated in these experiments will be useful for validating the mathematical model being developed to predict the cell magneto-hydrodynamics.

EXPERIMENTAL SETUP AND PROCEDURE

4.1 EXPERIMENTAL SETUP OF SIMULATED LOW TEMPERATURE HALL-HEROULT CELL

As discussed in previous chapters, the mandate in this investigation has been to measure the thermal distribution, current distribution, magnetic field, and velocities in a laboratory scale low temperature multi-anode Hall cell. A simulated model of Hall cell, in which, the electromagnetically driven flow occurring in an actual cell can be simulated, has been constructed. The model is approximately one-tenth scale and half portion of a cell, designed for the maximum total current supply of about 550 Amps. It contains molten wood's metal, which is driven in horizontal re-circulating flow by electromagnetic forces. Consequently, the simulated model is imperfect in the sense that it contains only one liquid (wood's metal) which moves under the influence of electromagnetic forces with no effect of the gas bubbles evolved at the anode. The other imperfection is that it simulates only an isolated cell whereas the actual cells are the members of the pot-lines. It is believed that behavior of each cell affects the functioning of the adjacent cells in the same pot-lines or adjacent pot-lines.

4.1.1 Components of the Simulated Cell

The schematic representation of simulated multi-anode Hall cell is shown Fig. 4.1. The major components of this cell are:

1. Inner stainless steel tank
2. Anode assembly and bus bars
3. Cathode collector bars
4. Heating system to melt wood's metal

4.1.1.1 Inner Stainless Steel Tank: The inner stainless steel tank simulates the carbon-lined cavity of Hall cell. The tank, which is made by welding the stainless steel

sheets of thickness 1.5 mm, has cavity dimension of 31X 31X10 cm³. Slots are cut on longer sides of the cell so that the collector bars welded at the base of the tank can pass through these, as shown in Fig. 4.1.

4.1.1.2 Anode Assembly and Bus Bars: Six stainless steel blocks (12 X 8 X 6 cm³) representing anodes are suspended in the tank as shown in Fig. 4.2. The blocks have a centrally threaded hole in which the copper rod of 1.0 cm diameter, simulating the anode rod, is tightened. Figures 4.3a and 4.3b are showing top views of bus bars attached to anodes for two different bus bar designs. Copper bus bars running across the top of the cell have threaded hole to which the threaded portion of the copper rod is fitted. Wood strips, as shown in Fig. 4.2, support the anode bus bars. Directions of current flow, in the conductors, are shown schematically in Figs. 4.4a and 4.4b. The positive terminal of the power supply is connected to the anode bus bar through a 0.5 cm thick copper strip.

4.1.1.3 Cathode Collector Bars: Cathode collector bars are made of 0.5 cm thick copper strips. Six copper strips, three on each side are welded on to the inside bottom of the inner tank and pass through the slots of dimensions (2.5 X 0.5 cm²) cut on longer walls of the tank. The collector bars are arranged in such a manner that these are lying below the center of the suspended anodes as shown in Fig. 4.1.

4.1.1.4 Heating System for the Cell: Banarjee and Evans[33] used hot water to melt wood's metal and maintain it in molten state. They employed two-tank arrangement in which the annular space between the tanks was filled up with hot water. To avoid any leakage of current from the inner tank (which represented the cell cavity) to the outer tank, an insulated layer was provided at the outer surface of the inner tank. This insulator made heat transfer from hot water to wood's metal difficult requiring several hours to melt wood's metal.

In the present design, the heating system is based on the hot air circulation, which is quite efficient. It takes much less time (only couple of hours) to completely melt the metal. Since there is no direct contact between the inner and outer tanks, there is no

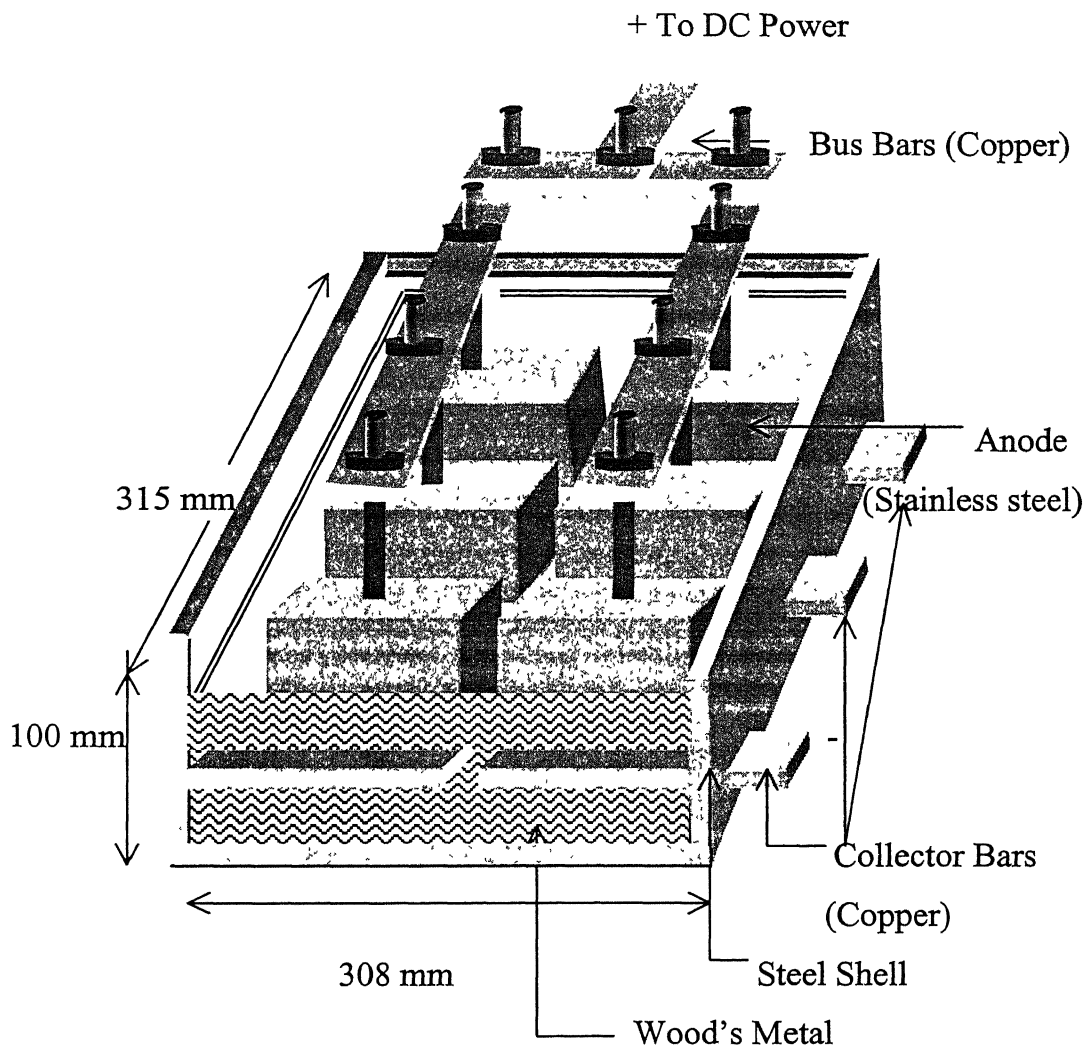


Fig 4.1 Schematic diagram of low temperature simulated Hall-Heroult cell.

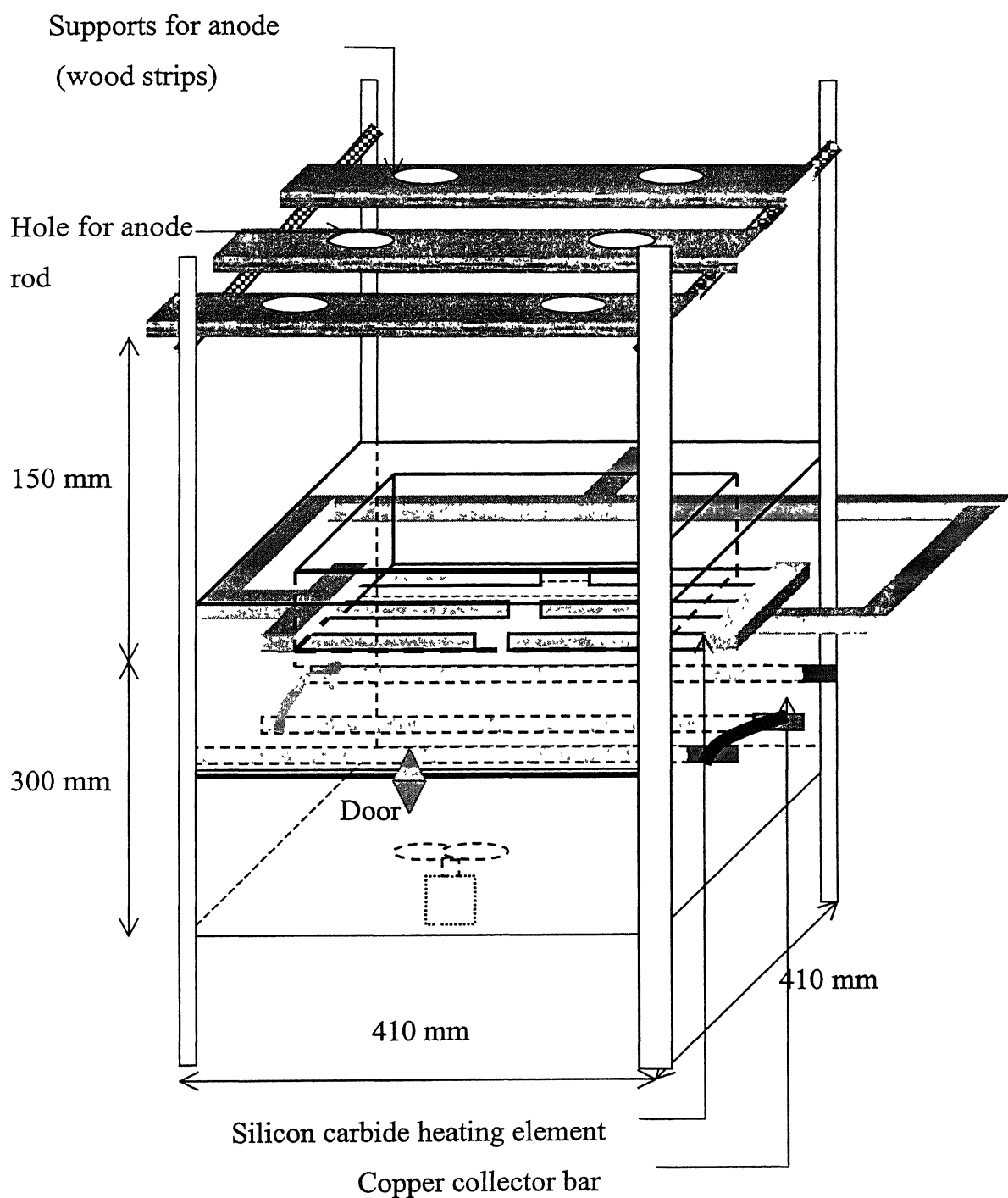


Fig. 4.2 Schematic diagram representing the cell and the heating system assembly.

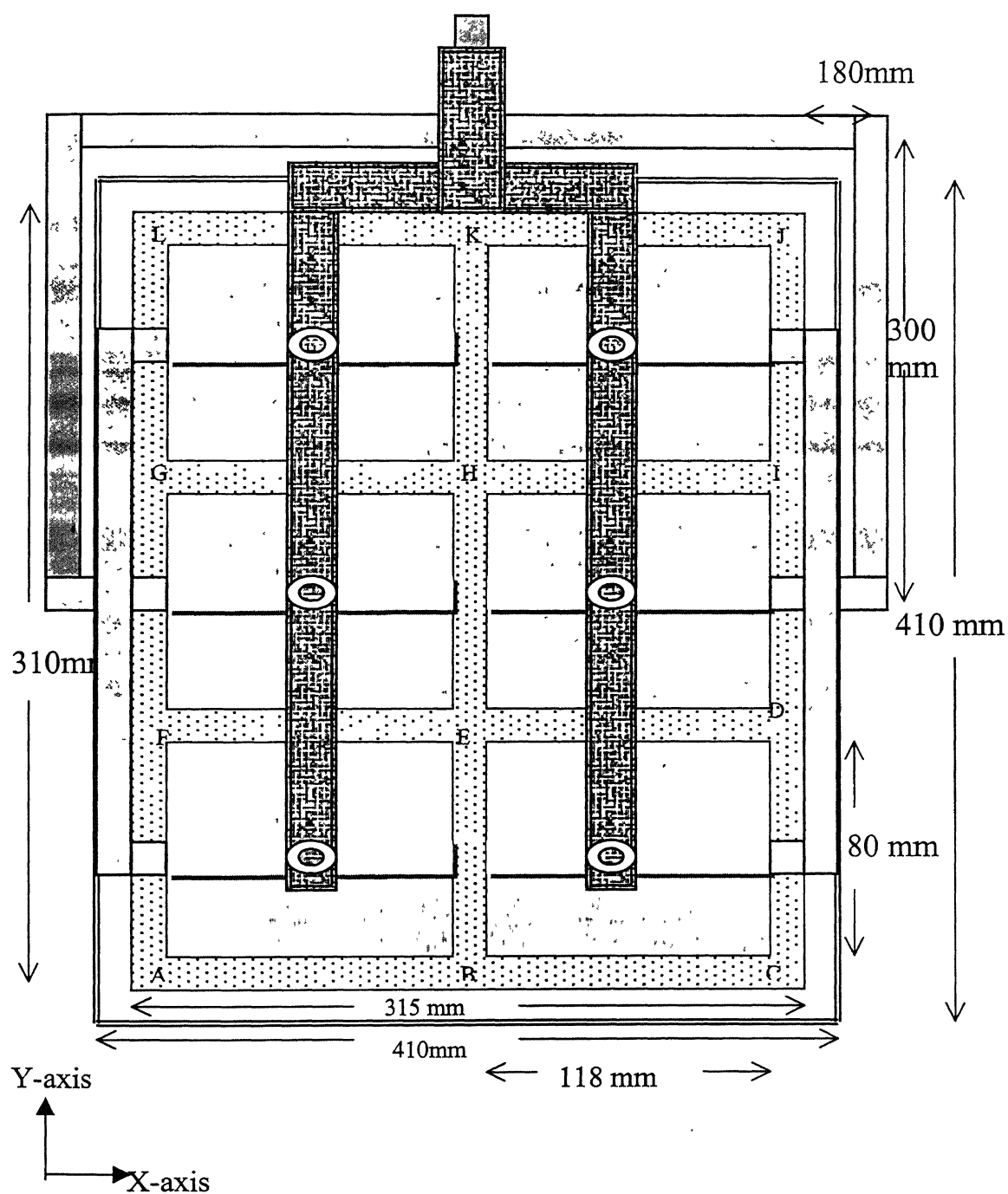


Fig. 4.3a Top view of bus-bars attached to anodes for end riser design.

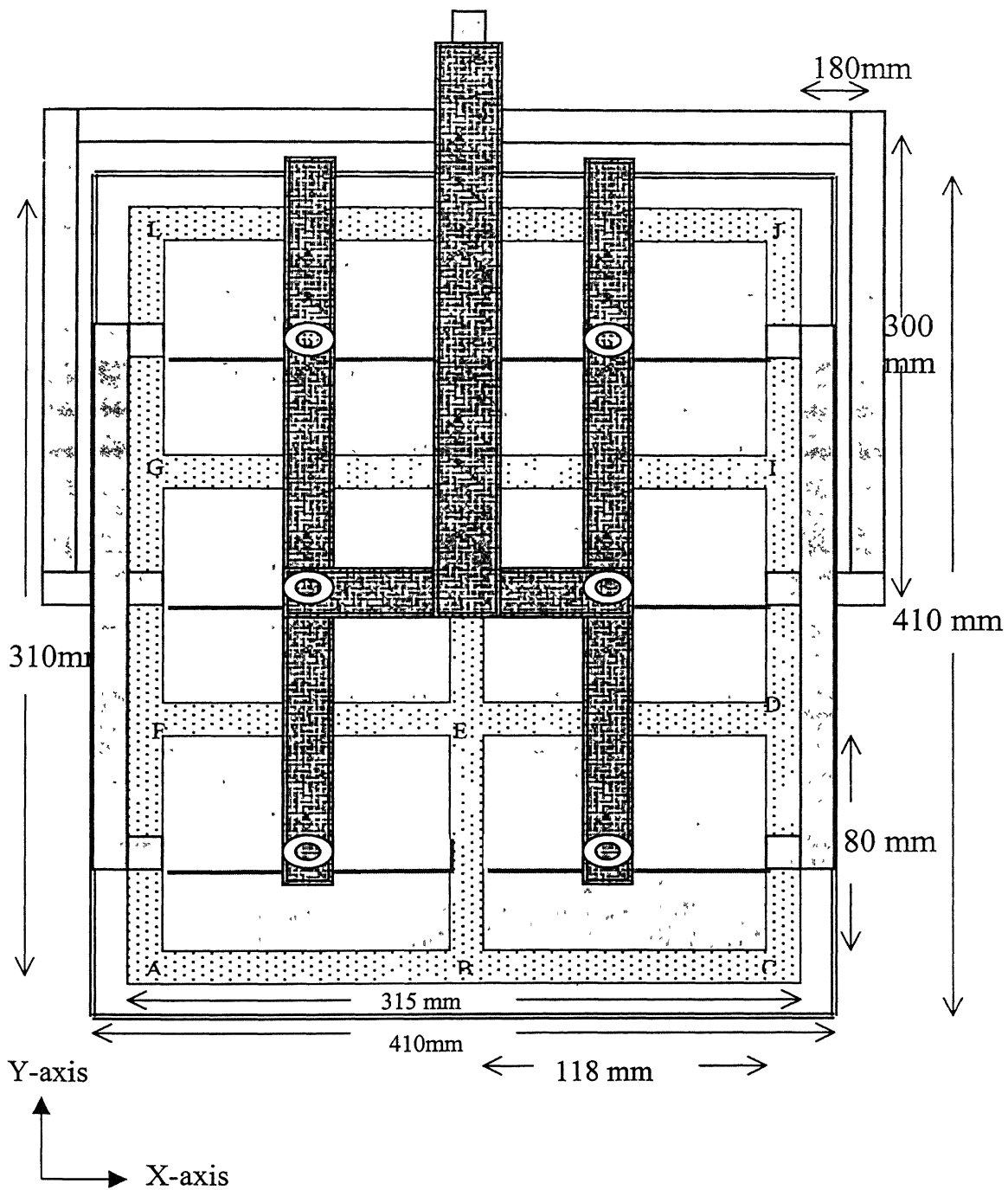


Fig. 4.3b Top view of bus-bars attached to anodes for quarter riser design.

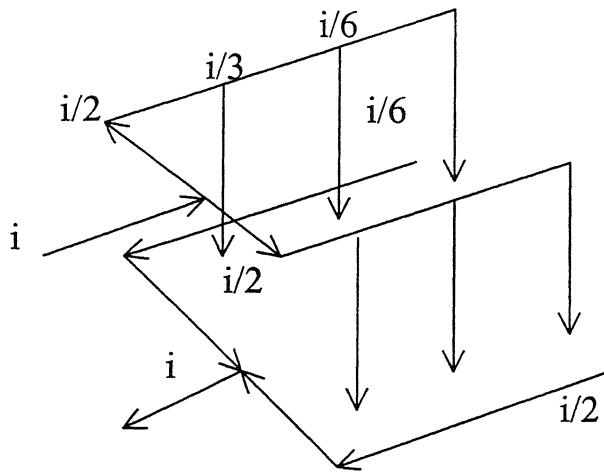


Fig 4.4a Schematic drawing of the end riser design.

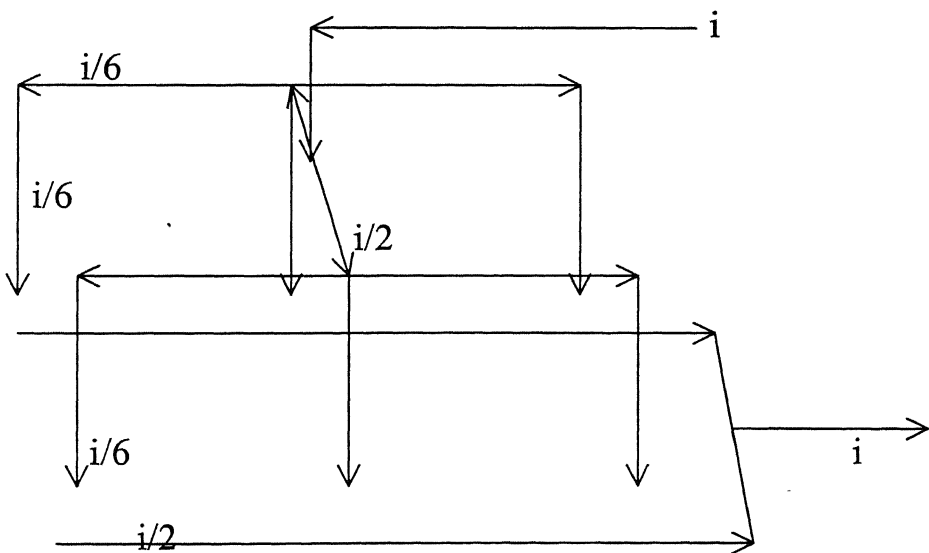


Fig. 4.4 b Schematic drawing of the quarter riser design.

need of providing an insulating film on outer surface of the inner tank. Three silicon carbide heating elements, spanning the width of the tank, are fixed in series in the annular space between the two tanks. These rods pass through three holes made across two sides of the outer tank, and are placed 10 cm below the bottom of the inner tank. An air-circulating fan is also fitted at the bottom of the outer tank, which provides fast and uniform heating, as shown in Fig. 4.5.

The multi-anode cell is placed inside the heating chamber, supported by four rods (diameter 2.0 cm) welded at the base of the outer tank as shown in Fig. 4.5. At top ends of the rods, mild steel pieces of $3 \times 4 \text{ cm}^2$ are also welded to give good support to the inner tank which may contain a heavy load of more than 50 kg of wood's metal. Rectangular Teflon sheets of $4 \times 5 \times 0.5 \text{ cm}^3$ are fitted at the top of mild steel pieces to avoid any current leakage from the inner tank to the outer tank. To sort out any problem in the heating chamber, a door is provided to have an access to it, as shown in Fig 4.2. To minimize the heat losses to the surrounding from the heating chamber, the side walls of heating chamber are insulated by asbestos cloth. Asbestos sheets cover the gap between the inner and the outer tank, which prevents the heat losses from the top surface.

4.1.1.5 Materials Used in the Cell: Wood's metal, used as the simulating liquid for the bath, is selected because of its high electrical conductivity and low melting point (m.p.= 70°C). The properties of wood's metal are given in Table 4.1.

Stainless steel is chosen to simulate the carbon anodes. Copper strips are used as collector bars. The ratios of the electrical conductivities of the electrolyte and anode, and cell lining and collector bars in the model and real cells are given in Table 4.2.

4.1.2 Power Supply

Current is passed through the cell by a DC power supply Model # 6681A (0-8 V/0-580 A) of Flewwlett Packed, US Make. The power supply could be used both in the constant current as well as the constant voltage modes.

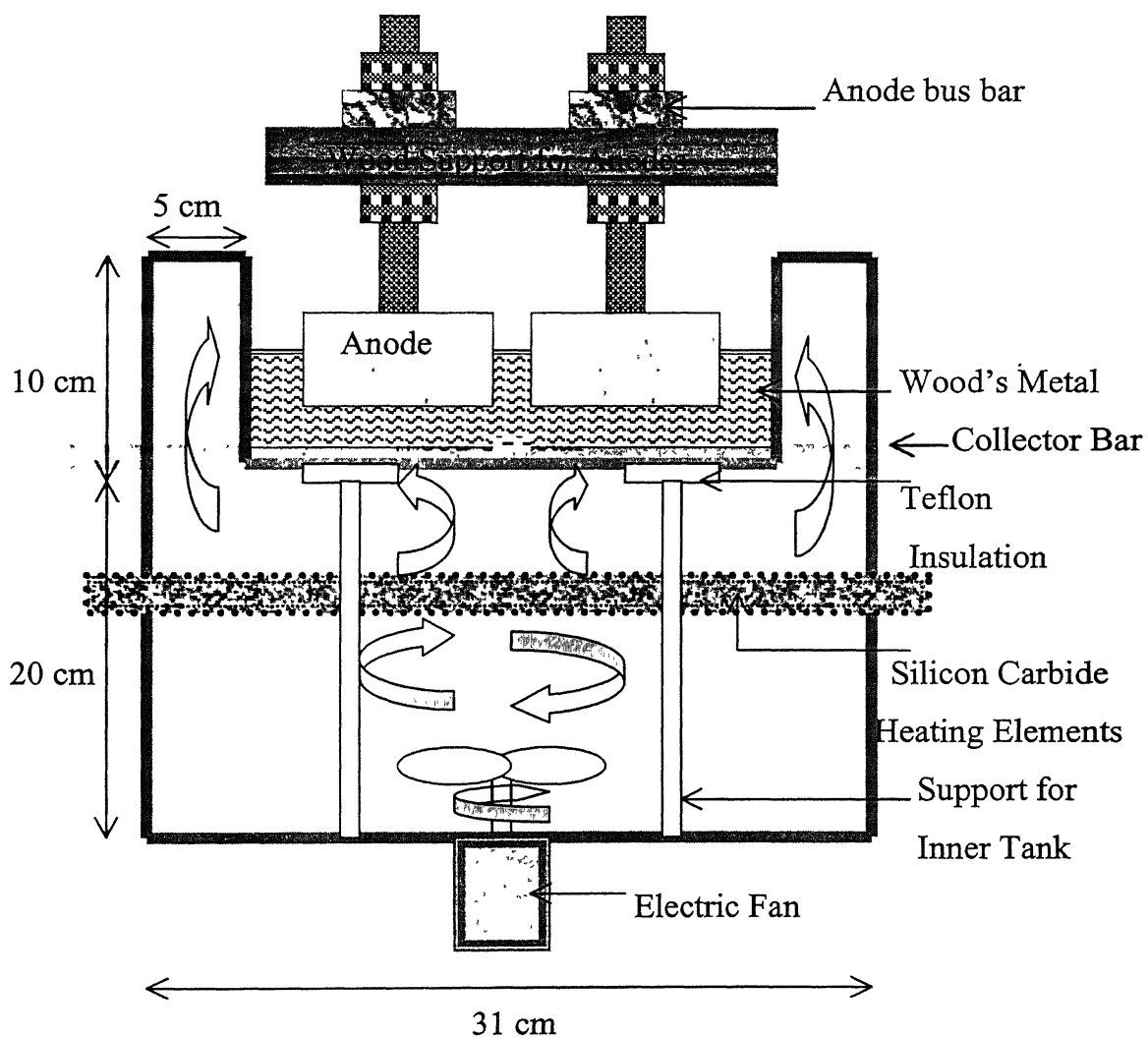


Fig. 4.5 Heating system based on circulation of hot air.

Table 4.1. Properties of Wood's metal [32]

1. Composition: - Bi = 50.0 %
Pb = 25.0 %
Sn = 12.5 %
Cd = 12.5 %
2.Melting Point: - 70 °C
3.Metal Density: - 10.7 gm/cm ³
4.Metal Viscosity: - 1.7 cp
5.Electrical conductivity: - $9 \times 10^5 \text{ ohm}^{-1} \text{ m}^{-1}$
6.Magnetic Permeability: - $1.26 \times 10^{-6} \text{ H/m}$

☉ All properties are at 110 °C.

Table 4.2. Ratios of Electrical Conductivities [33]

Model	
Wood's metal/stainless steel	0.37
Stainless steel/copper collector bars	0.044
Real Cell	
Electrolyte/carbon lining	0.014
Carbon lining/steel collector bars	0.056

4.1.3 Temperature Control of the Cell

Bath temperature is controlled manually by controlling current input to the heating elements through a variac. Temperature is measured using an alumel-chromel thermocouple (TC). The tip of the thermocouple (TC) is protected from damage by enclosing it in a stainless steel tube.

4.1.4 Current Measuring Instrument

Current flow in various conductors is measured using a True RMS Clamp-meter # DM DCM 39 (0-1000 Amp), India make. Current density within the melt is measured

by measuring the emf drop between two points with the help of copper conductors. The methodology is described latter in this chapter.

4.1.5 Magnetic Field Measuring Instrument

Magnetic field is measured using a Gauss meter model # 9640 (0.1 G to 30 kG), F W Bell, Orlando, Florida, USA make. The Gaussmeter is attached to the three-axis probe, which is based on Hall effect. Accuracy of the system, as claimed by the manufacturer, is 0.275 G.

4.1.6 Design and Construction of Velocity Probe

The principle of the probe is described in Chapter 2. Initially, the probe was constructed, based on by Ricou and Vives [32] design in which four copper conductors of diameter one mm are passed through a Teflon cylinder, which has four 1.5 mm diameter holes parallel to the length of the cylinder. The tips of these conductors surround a small permanent magnet as shown in Fig. 4.6. The problem with this design is that fluid flow between the tips is not smooth because the magnet inserted between the conductors protrudes out and interferes with the flow. This design gives half 'S' curves for velocity verses emf plots, instead of straight lines. This design is modified, by inserting the magnet inside the Teflon cylinder, as shown in Fig. 4.7. This results in an unhindered smoother fluid flow with calibration curves, which are approximately straight lines.

4.1.7 Design and Fabrication of Calibration Set-up

The apparatus used for calibration of the velocity probe is depicted in Fig. 4.8. It consists of a circular pot of diameter 16.0 cm and depth 7.0 cm, which is filled with wood's metal. A large circular pot filled with the water surrounds the inner pot. The water is heated up, which, in turn, heats up and melts wood's metal. An electric motor, the speed of which is controlled by a variac, gives circular motion to the inner pot. The speed of the rotation of the pot is precisely measured. It is assumed that melt contained in the pot rotates with the same rotational speed as that of rotating pot.

4.2 EXPERIMENTAL PROCEDURE

As already mentioned, experimental measurements are broadly divided into four categories:

1. Temperature measurements.
2. Current density measurements.
3. Magnetic field measurements.
4. Velocity measurements.

After about two and half-hour of switching on the external heat source, the metal bath melts down and attains a uniform temperature. At around 80 °C the whole bath is in fully molten state. The Gaussmeter and the two Nano-voltmeters are also switched on well before the actual measurements are made to allow enough time to stabilize. Power supply to the cell is switched on at least 10 minutes before the actual measurements, and current is set at a pre-specified value, which depends on current density at which the experiment is to be conducted. Current is equalized in all anodes as far as possible by adjusting positions of the nuts on the anode bars.

4.2.1 Temperature Measurements

Temperature has been measured using chromal-alumel thermocouple with accuracy of about 1 °C. Temperature is measured at twelve different locations indicated by 'A' to 'L' in Fig. 4.9.

4.2.2 Current Density Measurement

Current flow in various bars is measured with the help of True RMS Clamp-meter. It gives the amount of current flow in each conductor. The current density measurement in the molten metal is a difficult task and can not be measured directly. An indirect method is used to measure the current density by applying the Ohms law. Horizontal component of current density is measured by measuring the emf drops in two horizontal directions i.e in X and Y both directions. The emf drop is measured by using two sets of conductors each having two conductors. One set of tips is parallel to X-axis and other is perpendicular to it i.e. parallel to Y-axis measured in x and y directions

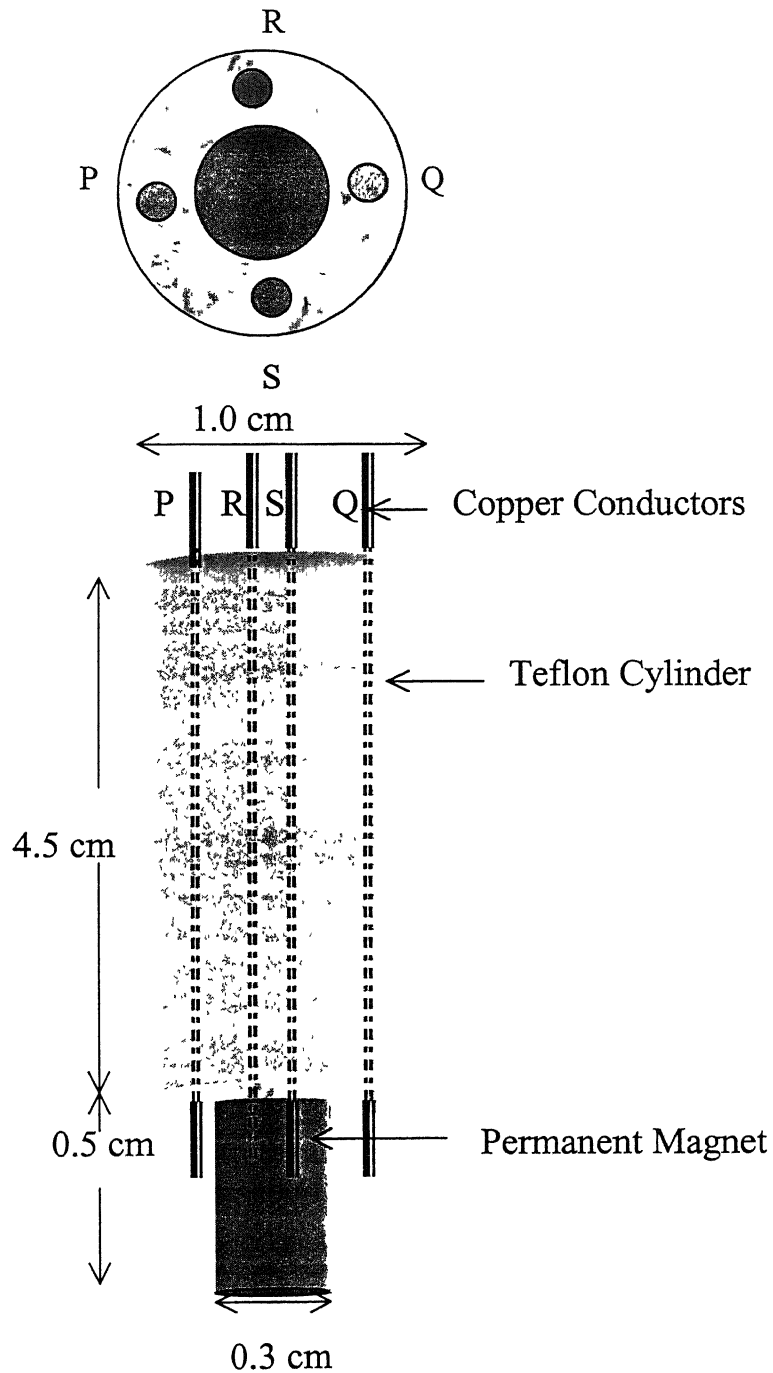


Fig. 4.6 Schematic diagram of the velocity probe as used by Banerjee and Evans[33].

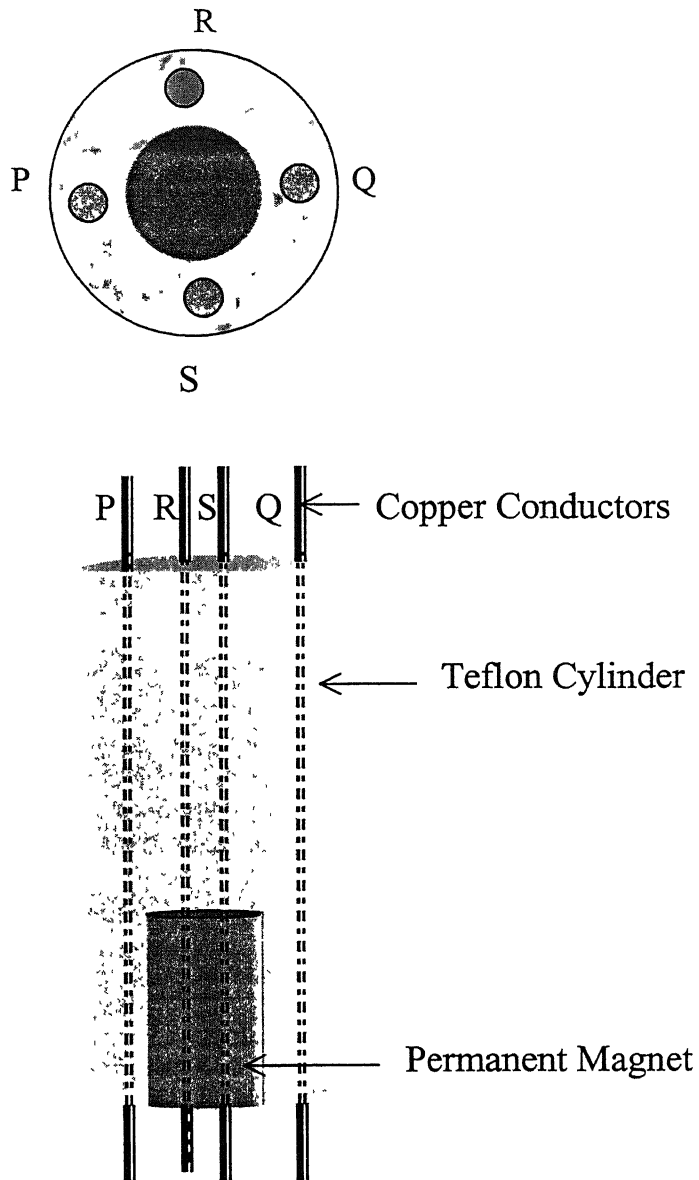


Fig. 4.7 Schematic diagram of the modified velocity probe used for measuring velocity.

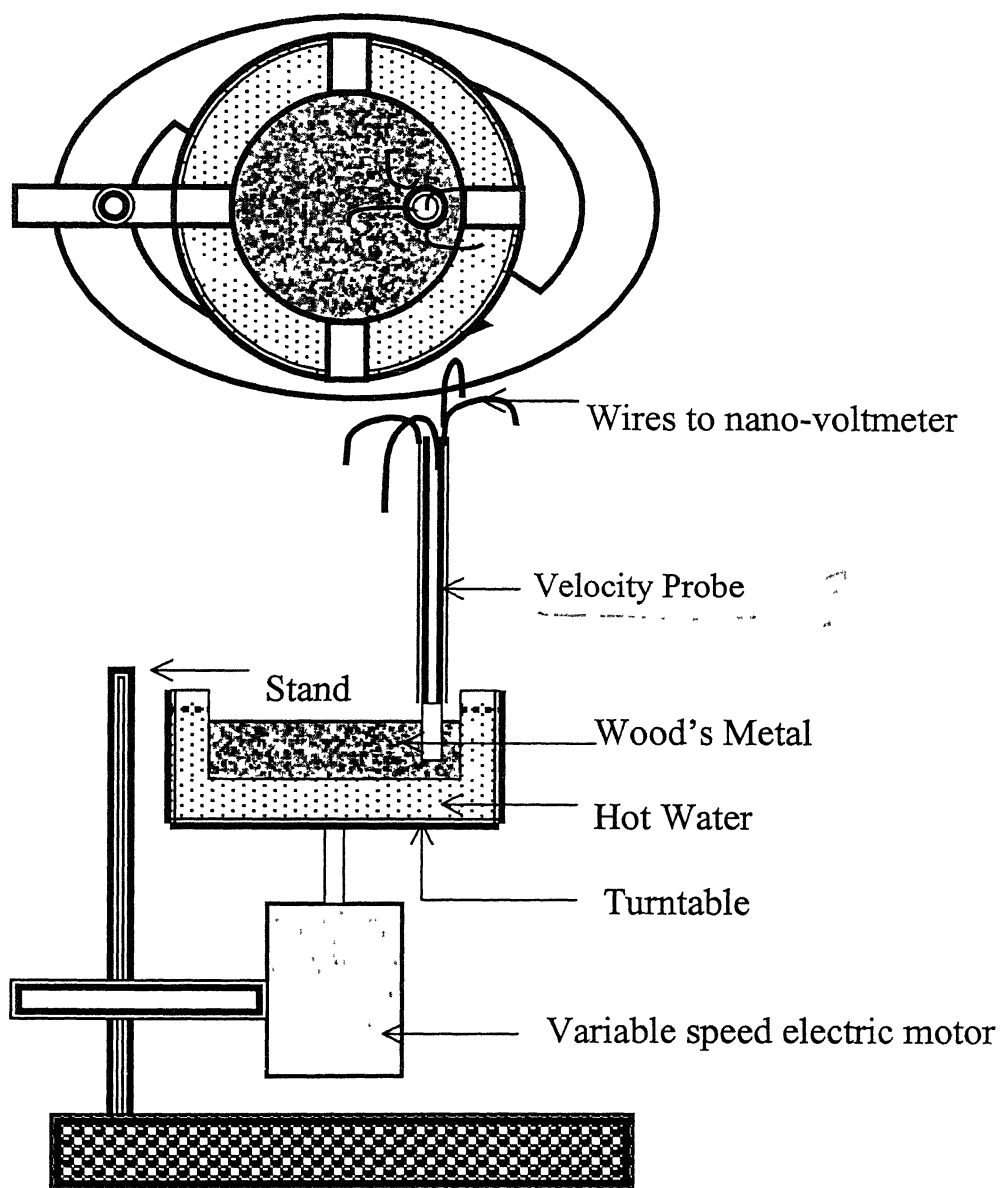


Fig. 4.8 Calibration set-up used to calibrate velocity probe.

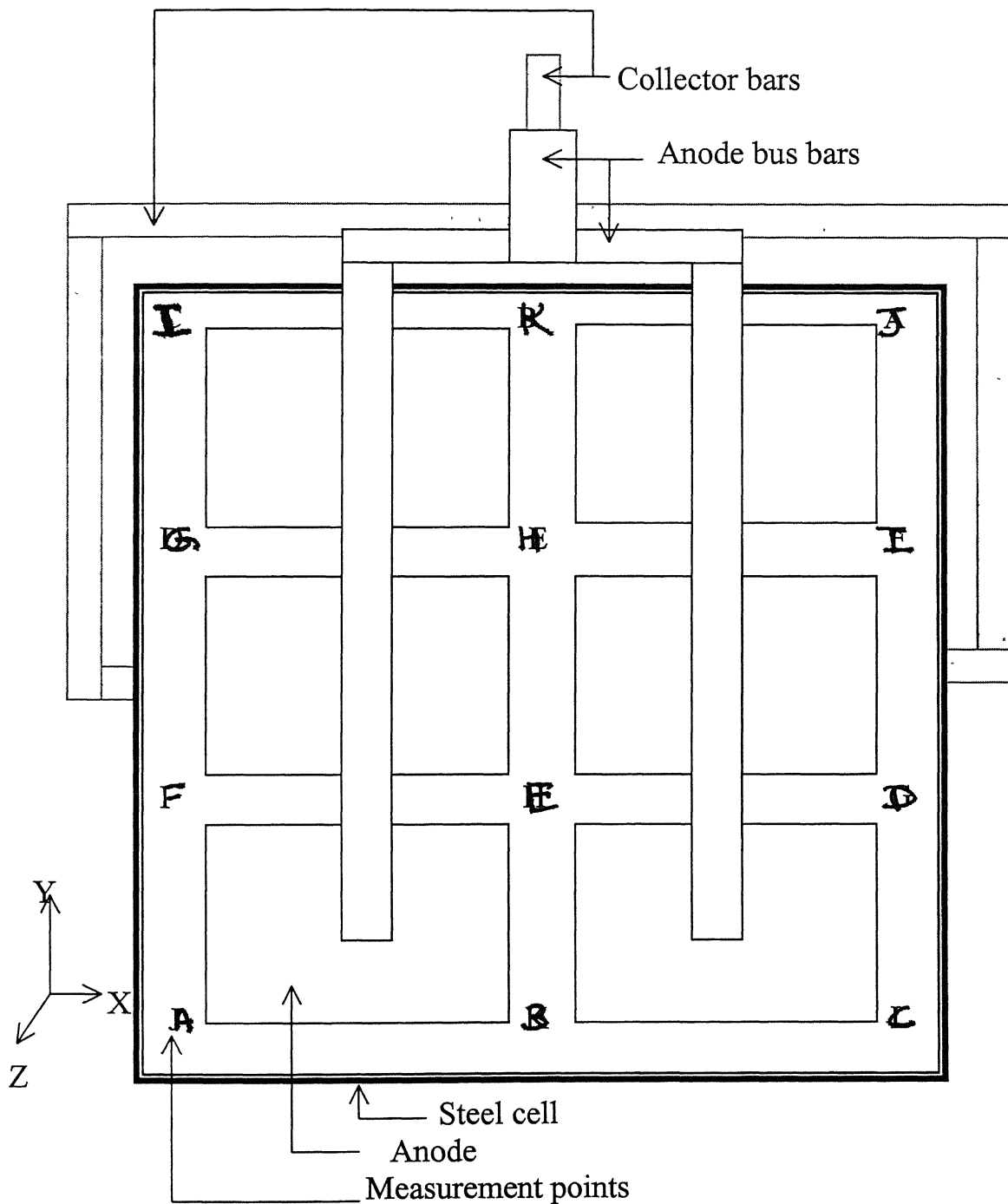


Fig. 4.9 Points 'A' to 'L' on which measurements are made.

current density respectively.

As applying the Ohms law:

$$E=i*R \quad (4.1)$$

where i is current flow, E is emf drop, and R is resistance of the conductor.

The resistance of a conductor is given by:

$$R=\rho*(l/A) \quad (4.2)$$

where ρ is resistivity of the conductor, l is length of the conductor, and A is area of the conductor.

Here wood's metal behaves as a conductor, l is length between two tips, and A is assumed area. From Eqs. 4.1 and 4.2. The current density between parallel to set of tips is:

$$\text{Current density} = i/A = E / (\rho*l) \quad (4.3)$$

Resistivity of molten metal is 1.1×10^{-6} ohm-m, distance between two tips is 6 mm, and E is emf sensed by nano-voltmeter across the tips.

$$\text{Current density (Amp/cm}^2\text{)} = 15000* E \text{ (volt)} = 15*E \text{ (mv)}$$

Current density has been measured at all twelve locations of the cell indicated by 'A' to 'L' as in Fig. 4.9 for different operational conditions.

4.2.3 Magnetic Field Measurements

Magnetic field measurements are made in the wood's metal at pre-specified depth at all twelve points from 'A' to 'L' in all three directions with the help of the Hall probe. To protect the probe against heat or any corrosive damage, it is enclosed in a refractory tube. These experiments are repeated at various current densities, ACDs, cold anode cases, and bus bar designs.

4.2.4 Velocity Measurements

4.2.4.1 Calibration of Velocity Probe: Both the modified and the unmodified probes have been calibrated using the set-up shown in Fig. 4.8. The motor is maintained at a low speed by controlling the applied voltage through a variac. Rotational speed of the motor is varied between 8 to 14 rpm. The emf generated at a particular location due

to fluid flow is recorded using two nano-voltmeters. The distance of the probe is varied from the center to outer periphery of the pot in steps of 0.5 cm. The velocity of the melt just underneath the probe tips in the tangential direction is calculated by recording the speed of the motor and the distance of the probe from the center of the pot.

$$\text{Velocity beneath the probe tips} = 2\pi \cdot d \cdot N / 60 \text{ cm/sec}$$

where d is distance from center of rotating pot in cm, N is speed of motor in rpm.

Velocity (cm/sec) verses e.m.f. (mv) plots for the two designs of the probe are shown in Figs 4.10 and 4.11. While the former is for the unmodified probe design, the latter is for the modified probe. The intercepts and the slopes for modified probe are given in Table 4.3.

Table 4.3 Slopes and intercepts of the calibration lines for the modified probe design.

Set of Tips of probe	Slope (mv/cm)	Intercept (mV)
PQ	0.00117	-0.0014
RS	0.00074	-0.0012

4.2.4.2 Velocity measurements: As described in Chapter 2, the velocity probe senses three emfs in switched on condition of the power supply. These are:

1. The emf sensed by the probe with zero current supply to the cell and with no forced flow of the melt - this may be termed as the cell constant emf
2. The emf due to current flow in the melt
3. The emf due to the melt flow

Thus, the total emf (E_{net}) is the sum of three emfs

$$E_{\text{net}} = a + b \cdot i + c \cdot i^2 \quad (4.4)$$

where a, b, and c are constant parameters.

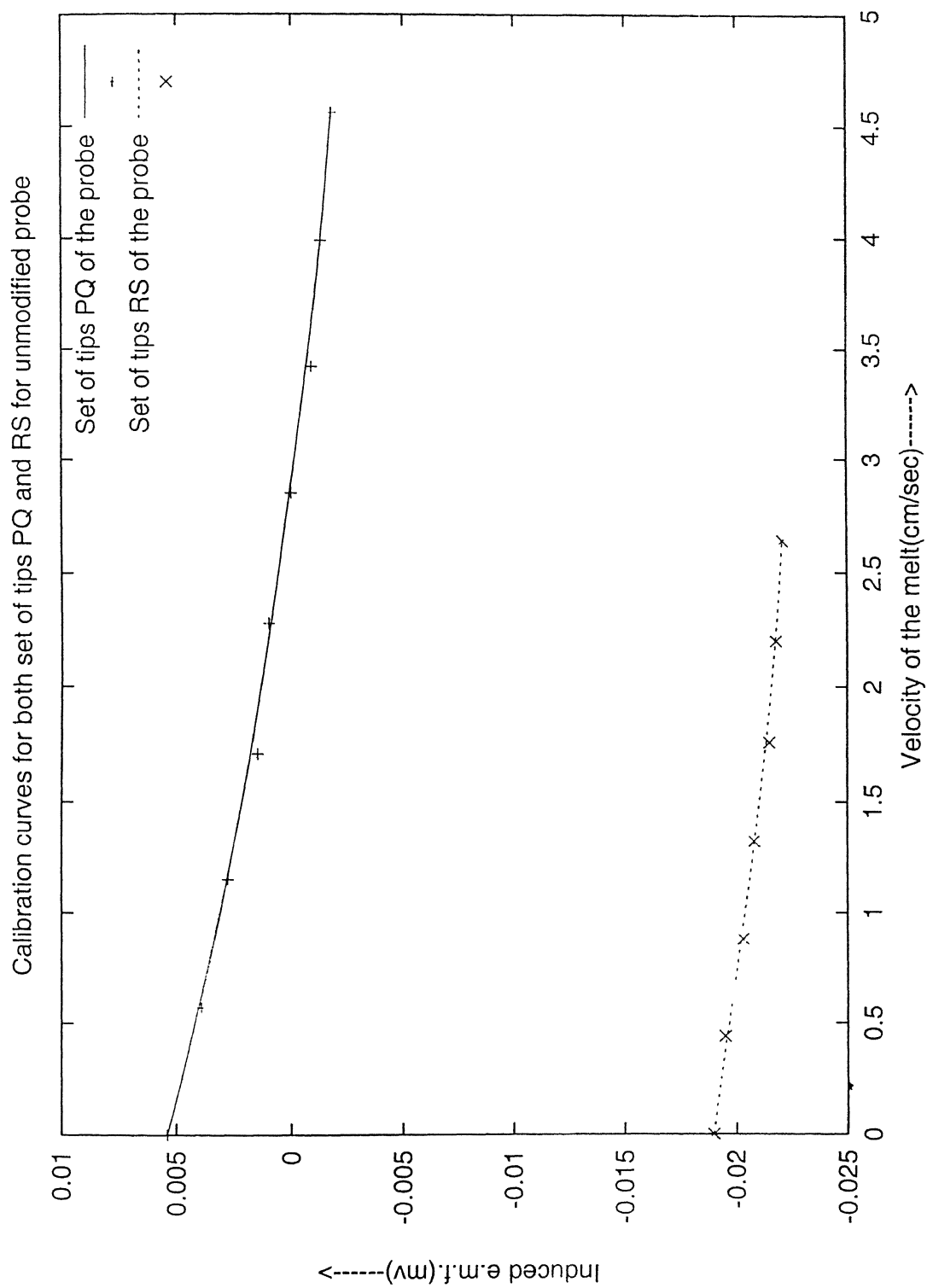


Fig. 4.10 Calibration plots for the unmodified velocity probe for both set of tips PQ and RS.

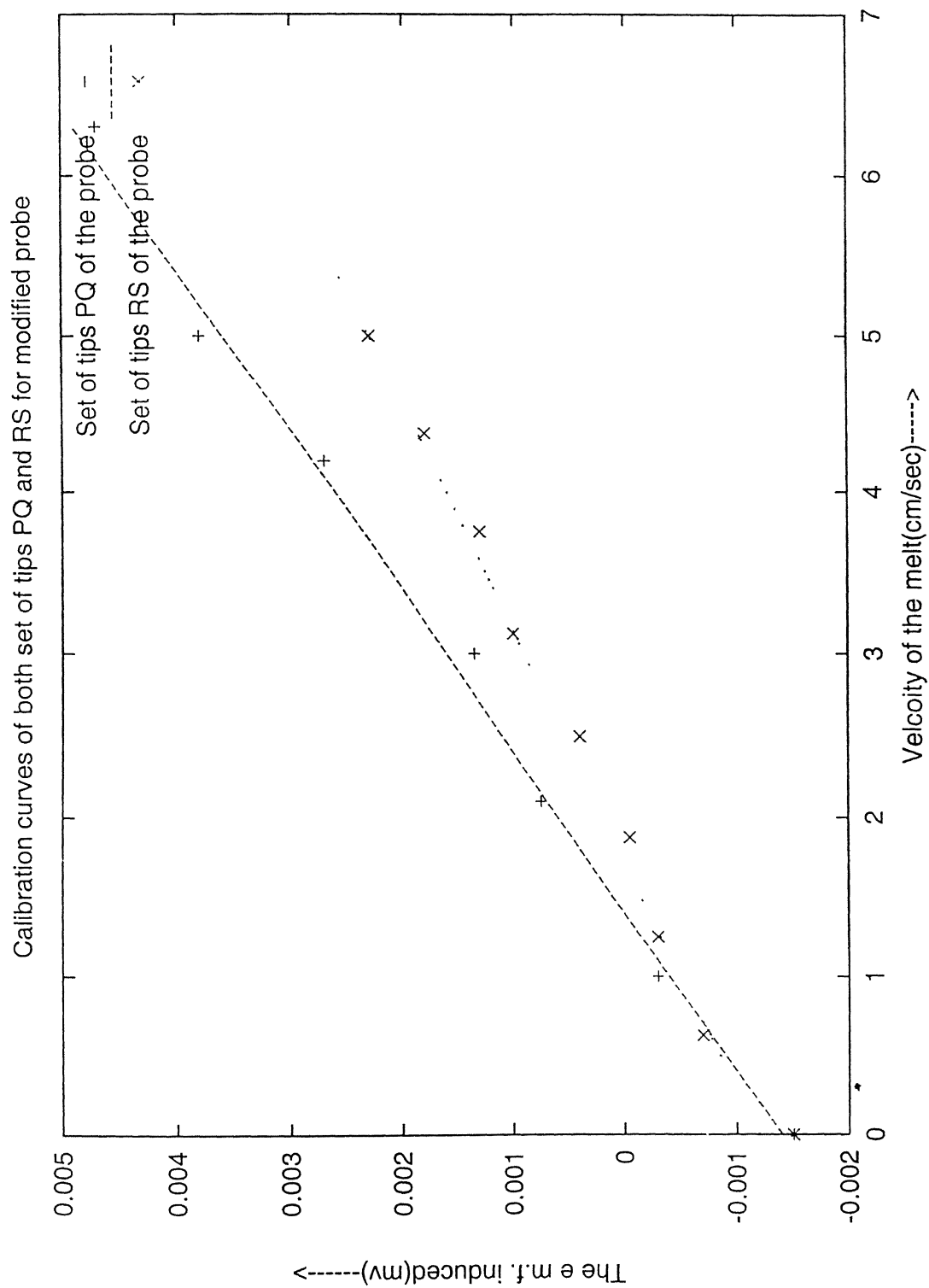


Fig. 4.11 Calibration plots for the modified velocity probe for both set of tips PQ and RS

Banrjee and Evans [33] did not perhaps note that the presence of the cell constant emf. They employed the technique in which they switched off the power supply. Under this condition, the emf developed by the current flow disappears as soon as the current flow is stopped, while the emf generated by the melt flow diminishes to zero only over a period of several tens of seconds as the wood's metal is gradually brought to rest by the drag forces. Hence under the switched off condition, the net emf recorded by the probe is taken to be the emf due to the melt flow. Thus, in the emf verses time plot, the extrapolated value of the emf at zero time (i.e the time when the current is switched off) corresponds to the emf induced by the melt flow under the normal operating conditions.

It may be pointed out that this technique of velocity measurement has a few experimental difficulties:

- The cell constant part (term 'a' in Eq. 4.4), which may have a substantial contribution to the total emf, as shown in Tables 4.4-4.6, is ignored. It is evident that 'a' is a function of position and temperature.
- Large fluctuations are recorded during the measurements, which create difficulty in accurate estimate of melt velocity.

To surmount these difficulties/limitations, a modified technique has been adopted in the present investigation. In this technique, the net emf at a given position is recorded under the switched on condition of the power supply. A methodology, for estimating the constant parameters, a and b in Eq. 4.4 independently, is evolved. Once these constants are known, the contribution arising due to the melt flow is estimated by difference. The method of estimating a and b is described below.

The probe is fixed at a point with the support of a stand. E_{net} at a given probe position is measured as a function of current flowing through the melt. Current is varied from 0 to 550 Amp in steps of 50 Amp without disturbing the probe. The time interval between the two consecutive steps is kept about 5-7 minutes to allow the liquid motion in the cell to be stabilized. Two nano-voltmeters are used to record the emfs generated across the probe's tips, PQ and RS. This gives two-direction flow measurement of the melt.

Table 4.4 Constant part of readings with position and temperature for tips PQ of probe.

Temperature (°C)	Point A (mv)	Point C (mv)	Point G (mv)	Point J (mv)
90	0.001407	0.000916	0.000958	0.000987
100	0.001558	0.001330	0.000416	0.000856
110	0.001630	0.001545	0.000236	0.001442

Table 4.5 Constant part of readings with position and temperature for tips RS of probe.

Temperature (°C)	Point A (mv)	Point C (mv)	Point G (mv)	Point J (mv)
90	0.004237	0.004995	0.005067	0.004218
100	0.004899	0.004670	0.004998	0.003210
110	0.005594	0.005638	0.006912	0.004855

Table 4.6 Constant part of emf with temperature for point A.

Temperature °C	Tips PQ(mv)	Tips RS(mv)
78	0.000814	0.003046
81	0.000894	0.003150
83	0.000981	0.003433
86	0.001078	0.003519
88	0.001304	0.004001
90	0.001407	0.004237
93	0.001437	0.004510
95	0.001481	0.004661
98	0.001518	0.004778
100	0.001558	0.004899
102	0.001586	0.005108

The PQ tips correspond to one axis (X-axis) and the RS tips correspond to the other (Y-axis). Thus, the probe measures the velocity in two normal horizontal directions simultaneously.

The net emf generated across the one set of probe tips, which is the summation of the three emfs, is schematically shown in Fig. 4.12.

Differentiating Eq. 4.4 with respect to i

$$dE_{\text{net}}/di = b + 2c*i \quad (4.5)$$

At $i = 0$,

$$(dE_{\text{net}}/di)_{i=0} = b \quad (4.6)$$

The value of parameter 'a' is found by extrapolating, E_{net} verses i curve for $i=0$, i.e.,

$$(E_{\text{net}})_{i=0} = a \quad (4.7)$$

Thus, the e.m.f. generated by the melt flow is

$$E_{\text{melt flow}} = (c*i^2) = E_{\text{net}} - (E_{\text{net}})_{i=0} - (dE_{\text{net}}/di)_{i=0} * i \quad (4.8)$$

The coefficients of Eq. 4.4 are calculated by fitting a parabolic equation to the experimental data by employing the least square error method. The values of these parameters are given in Table 4.7 for different locations of the cell for one experiment. As it is evident, the values are position dependent. The flow chart of the algorithm used, and the program structure are given in **Appendix A**.

Figures 4.13 and 4.14 show fitted curves, the tangents at zero current supply, and the cell constant parts at two different locations in the cell. While Fig. 4.13 shows the y component of velocity at location 'H', Fig. 4.14 shows x component of velocity at location 'B'. Figure 4.13 shows that the polarities of emfs generated by the current flow and the melt flow are same so that the slope of the curve is constantly increasing with increase in current. But in case of Fig. 4.14, the polarities are in the reverse direction, resulting in decreasing slope with increase in current input to the cell.

Table 4.7 Values of constant parameters at different positions of the cell, when E_{net} is in mv and current is in Amp.

Point	Axis X (PQ tips)			Axis Y (RS tips)		
	a	b	c	a	b	c
A	0.000793	2.2×10^{-4}	1.79×10^{-9}	0.001729	-1.09×10^{-4}	7.26×10^{-9}
B	0.000987	5.5×10^{-4}	-2.31×10^{-9}	0.000004	1.72×10^{-4}	-0.42×10^{-9}
C	0.000487	2.8×10^{-4}	-2.79×10^{-9}	0.000170	0.23×10^{-4}	3.65×10^{-9}
D	0.000294	12.7×10^{-4}	1.41×10^{-9}	-0.001074	2.2×10^{-4}	0.47×10^{-9}
E	-0.00154	14.2×10^{-4}	-12.4×10^{-9}	-0.000161	0.72×10^{-4}	4.68×10^{-9}
F	0.000371	1.9×10^{-4}	-6.9×10^{-9}	-0.000387	-0.74×10^{-4}	2.92×10^{-9}
G	0.000773	-3.4×10^{-4}	11.7×10^{-9}	-0.000457	0.11×10^{-4}	-1.01×10^{-9}
H	0.000843	-2.26×10^{-4}	0.72×10^{-9}	-0.001006	1.12×10^{-4}	-8.67×10^{-9}
I	0.001354	-2.33×10^{-4}	-4.27×10^{-9}	-0.001183	1.32×10^{-4}	1.32×10^{-9}
J	0.001328	-1.6×10^{-4}	1.01×10^{-9}	-0.001819	3.5×10^{-4}	-1.46×10^{-9}
K	0.000564	-1.58×10^{-4}	1.79×10^{-9}	0.001256	0.31×10^{-4}	-4.77×10^{-9}
L	0.000530	-0.6×10^{-4}	0.99×10^{-9}	-0.001377	-0.54×10^{-4}	-2.93×10^{-9}

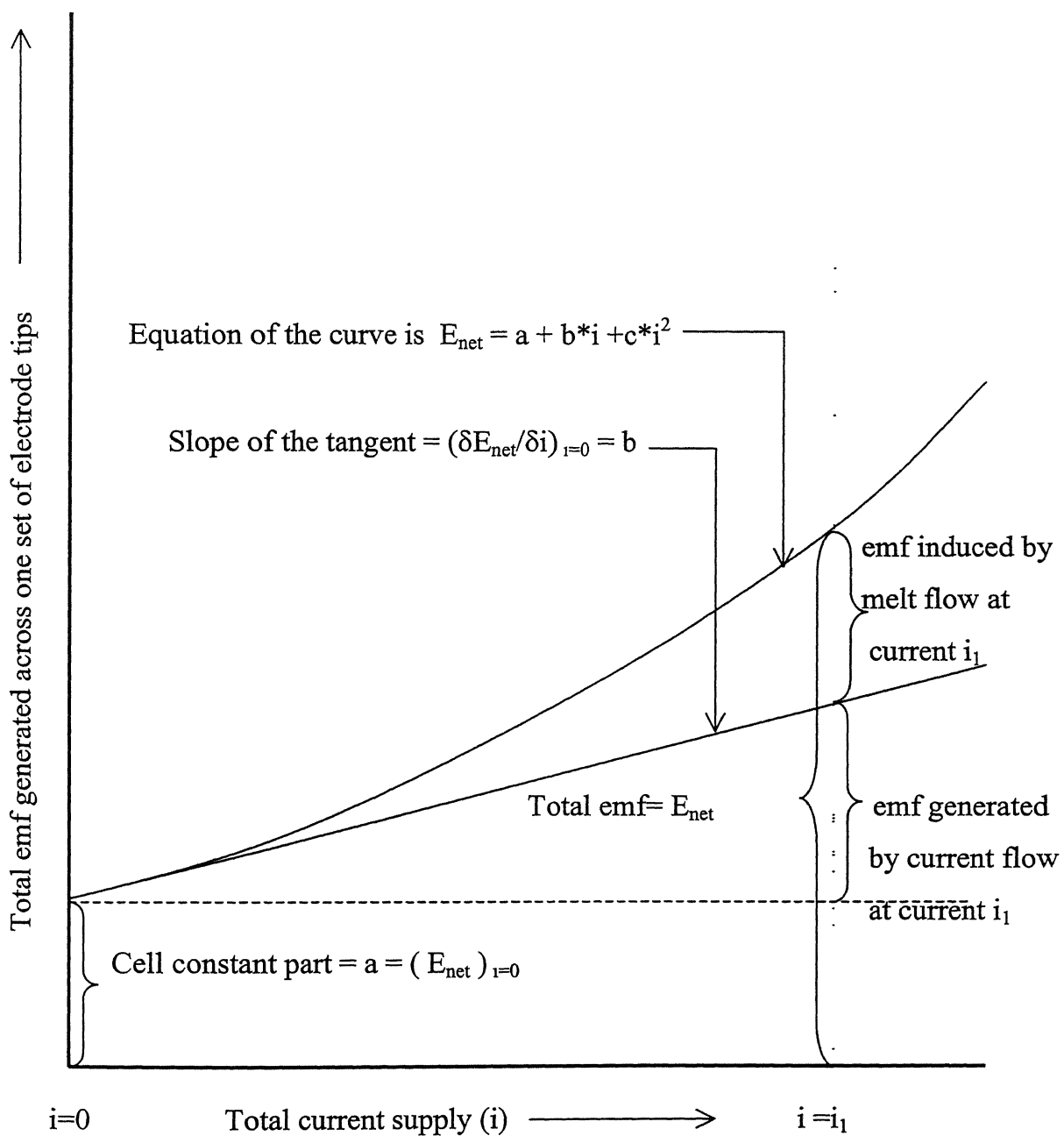


Fig. 4.12 Schematic representation of various parts of net emf.

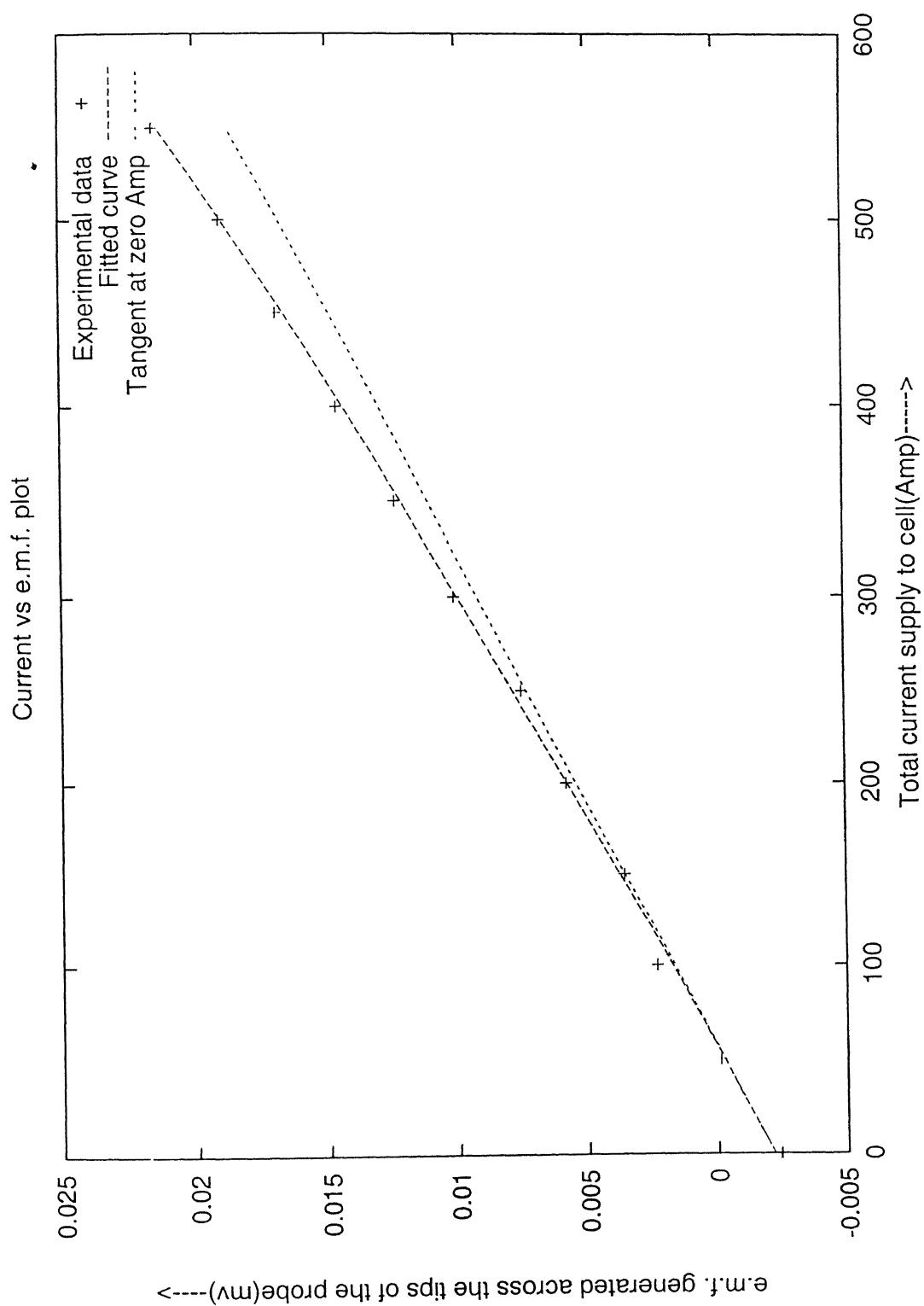


Fig. 4.13 Current verses emf plot, when the emfs generated by the melt flow and drop in the same direction.

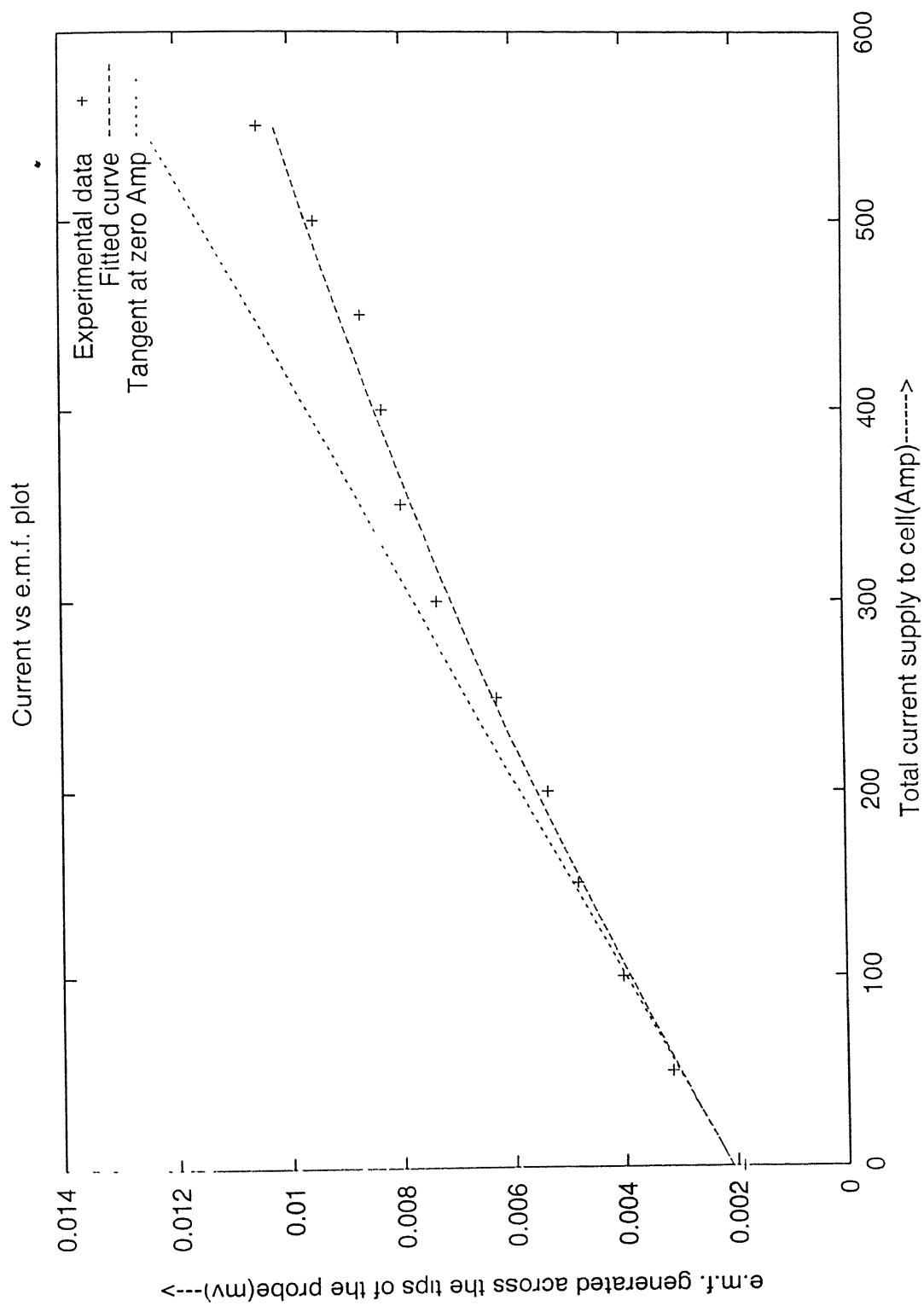


Fig. 4.14 Current verses emf plot, when the emfs generated by the melt flow and drop in the opposite direction.

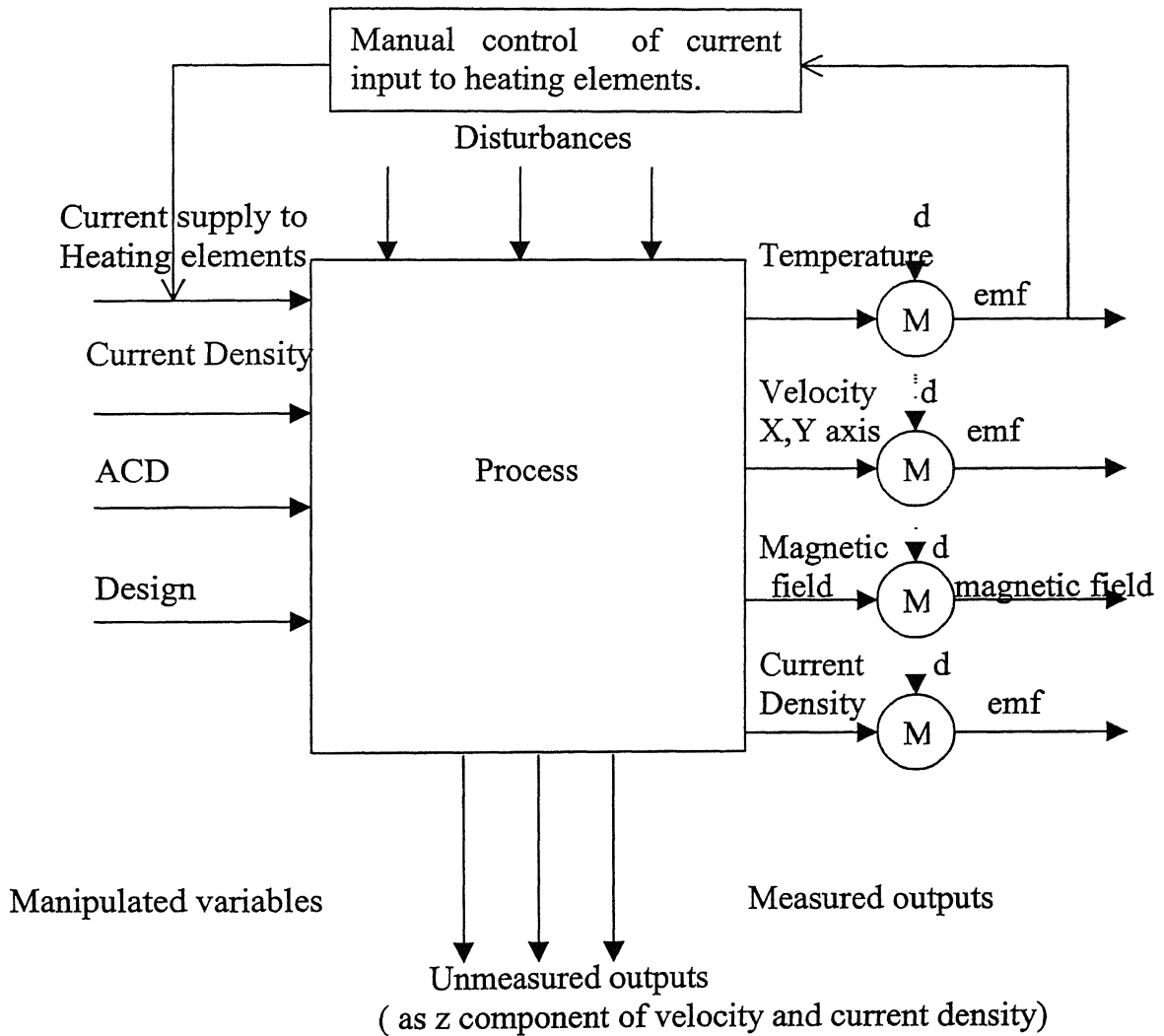
Chapter 5

RESULTS AND DISCUSSION

In each set of experiments, magnetic field, velocity, and current distribution are measured at positions marked 'A' to 'L' in Fig. 4.9. Effects of changing ACD, current input, unbalanced anode system, design of bus bars have been observed on magnetic field, current and velocity distributions. Current input in each set of experiments is varied from 0 to 550 Amp in steps of 50 Amp. ACD is varied from 1.0 to 2 cm in steps of 0.5 cm. While in one set of the experiments one corner anode is removed, the middle anode is replaced in another set of experiments. Two bus bar designs have been employed: (i) the end riser design, and (ii) is the quarter riser design. Wall to anode distance has been maintained the same in all experiments. Process variables and their ranges examined in this investigation are given in Table 5.1. A block diagram of the process representing various inputs and outputs is given in Fig. 5.1.

Table 5.1 Process variables and their ranges investigated in various set experiments.

Sr. No.	Variables	Ranges/Types
1.	Total Current Input	0-550 Amp in steps of 50 Amp
2.	Current Density	0 to 0.96 A/cm ²
3.	Anode Cathode Distance	1.0, 1.5, 2.0 cm
4.	Anode Positions	All anodes placed at prescribed positions One anode removed from the middle row One anode removed from the corner.
5.	Bus Bar Design	End Riser Design. Quarter Riser Design.



- (M) Measuring instrument (i.e thermocouple, velocity probe, Hall probe)
- d disturbances (error in measurement or noise of instrument)

Fig. 5.1 Block diagram of process representing various inputs and outputs.

5.1 REPRODUCIBILITY EXPERIMENTS

Reproducibility of the experiments is verified for the velocity, current density, and magnetic field measurements. Current density within the melt, as recorded on two different days, is shown in Figs. 5.2 and 5.3. Upto about 20 % variations is observed. The primary cause of this variation is that it is extremely difficult to maintain the same input current distribution in anodes in any two different experiments.

The result of magnetic field recorded on three different days under the same experimental conditions reported in Table 5.2. There is upto about 20 % variation in results. These variations are also due to the differences in input current distribution in anodes on three different days.

Velocity has been measured on three different days, as shown in Table 5.3, under identical experimental conditions. Variation in results is up to about 25 %.

Table 5.2 Magnetic field (Gauss) recorded in identical experiments on three different days.

Point	Day 1			Day 2			Day 3		
	Bx	By	Bz	Bx	By	Bz	Bx	By	Bz
A	0.1	1.0	3.2	-0.2	0.8	3.2	0.2	0.8	3.5
B	-1.0	0.5	0.6	-1.1	0.6	0.6	-1.1	0.4	0.3
C	-1.3	0.0	-3.3	-1.4	0.7	-3.1	-1.0	-0.2	-3.8
D	-0.8	-1.0	-2.6	-1.3	-1.0	-2.4	-0.6	-1.4	-2.9
E	0.5	-0.4	0.6	0.2	-0.4	0.6	0.7	-0.4	0.1
F	0.9	0.4	1.9	0.7	0.6	1.9	0.6	0.2	1.8
G	4.1	-1.1	-3.6	4.2	-0.8	-3.0	3.5	-1.3	-3.7
H	3.6	-3.0	1.1	3.5	-2.5	1.2	2.9	-2.6	0.8
I	2.3	-4.5	6.8	2.1	-4.4	6.7	1.3	-5.0	6.0
J	4.1	-2.4	10.3	4.2	-2.1	11.0	3.4	-3.0	11.0
K	4.7	-3.9	1.3	5.1	-4.4	1.6	4.2	-4.6	1.3
L	2.4	-2.3	-8.7	2.6	-2.5	-8.4	2.3	-3.0	-8.4

Current Density $\cong 0.9 \text{ A/cm}^2$

ACD = 1.0 cm

Current Density in Melt

(A/cm^2) \longrightarrow

1 A/cm^2
 \longleftrightarrow

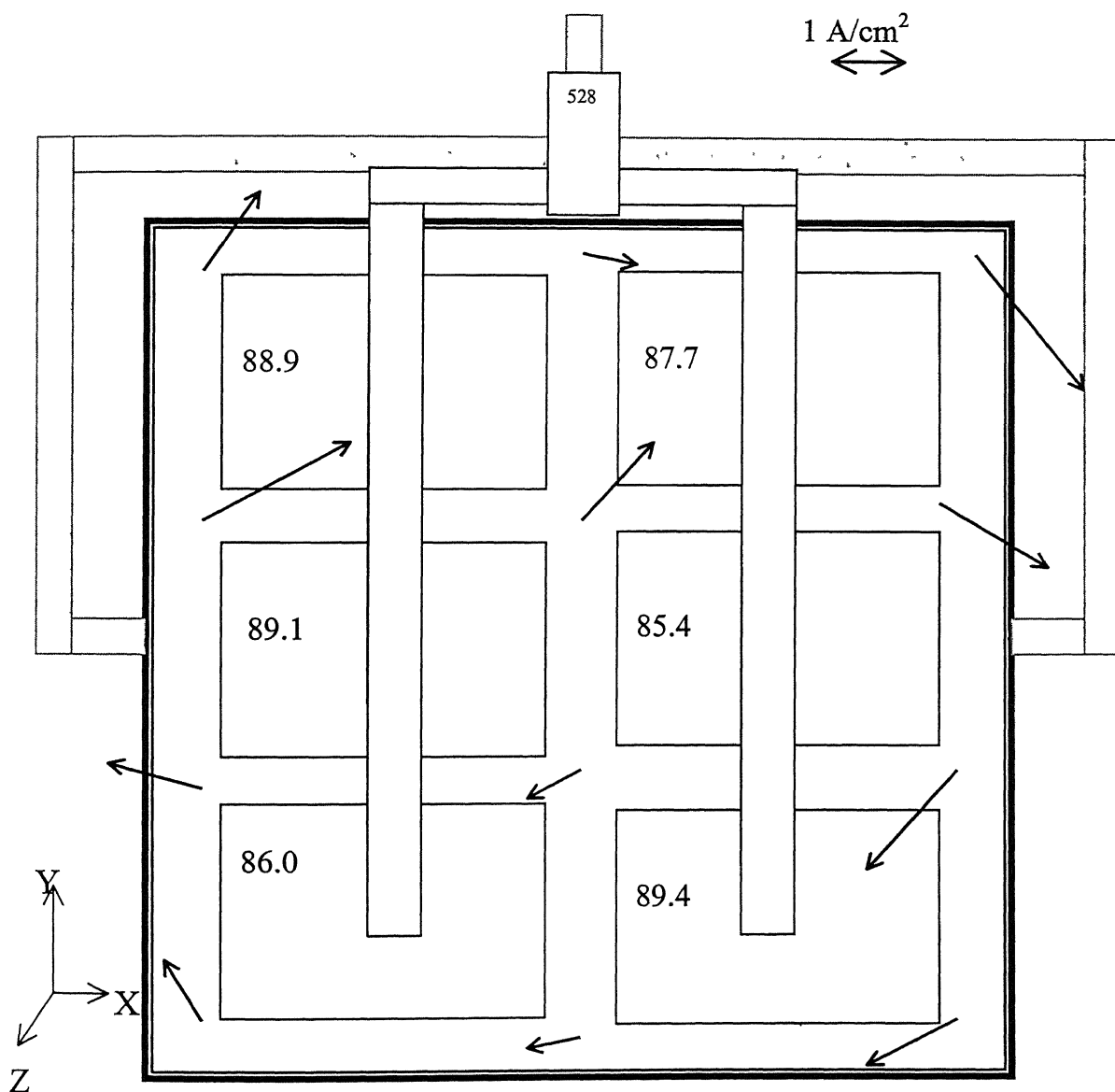


Fig. 5.2 Measured horizontal components of current densities.

Current Density $\cong 0.9 \text{ A/cm}^2$

ACD = 1.0 cm

Current Density in Melt

(A/cm^2)

1 A/cm^2

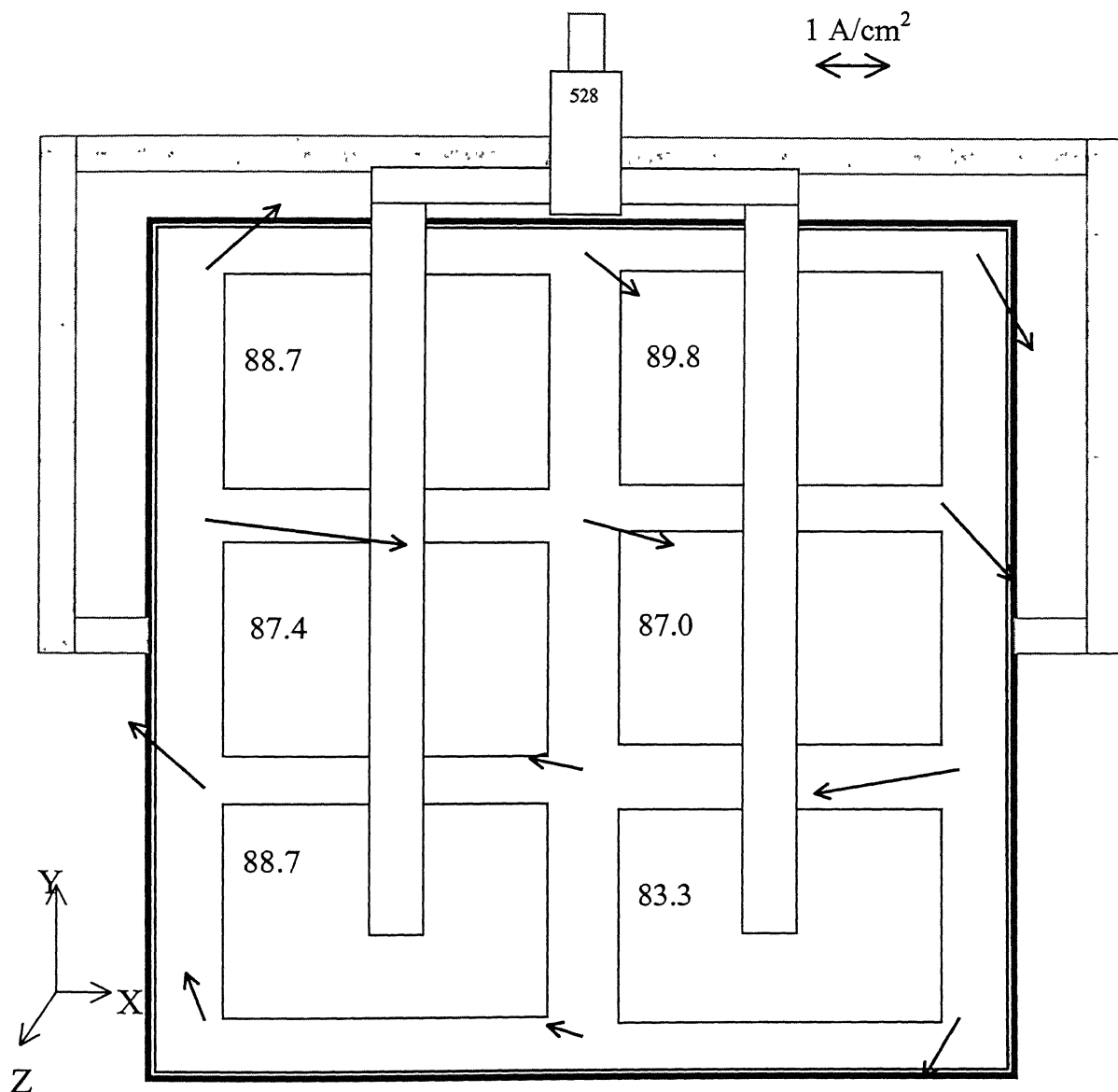


Fig. 5.3 Measured horizontal components of current densities.

Table 5.3 Horizontal velocities as measured on three different days under identical experimental conditions.

	Day 1	Day 2	Day 3
Point	Resultant	Resultant	Resultant
A	0.6 cm/sec	0.6 cm/sec	1.0 cm/sec
B	1.0 “	0.7 “	1.3 “
C	1.4 “	1.2 “	1.3 “
D	0.9 “	1.7 “	0.9 “
E	0.8 “	0.7 “	1.0 “
F	1.0 “	0.9 “	1.4 “
G	0.6 “	1.2 “	1.4 “
H	1.0 “	1.4 “	0.8 “
I	1.0 “	1.1 “	1.0 “
J	1.5 “	1.2 “	1.8 “
K	1.2 “	1.7 “	1.3 “
L	1.6 “	1.7 “	1.3 “

5.2 THERMAL DISTRIBUTION

Temperature, as recorded at different locations of the cell from points ‘A’ to ‘L’, is reported in Fig. 5.4. The maximum variation in temperature within the cell is 3 °C. It is not showing any specific trend. Temperature becomes more uniform when the cell is in the switched on mode of the power supply, due to convective mixing within the melt.

5.3 CURRENT DISTRIBUTION

Horizontal components of current density within the melt are measured, as described in Chapter 4, at all locations from ‘A’ to ‘L’. The effects of the various parameters are investigated.

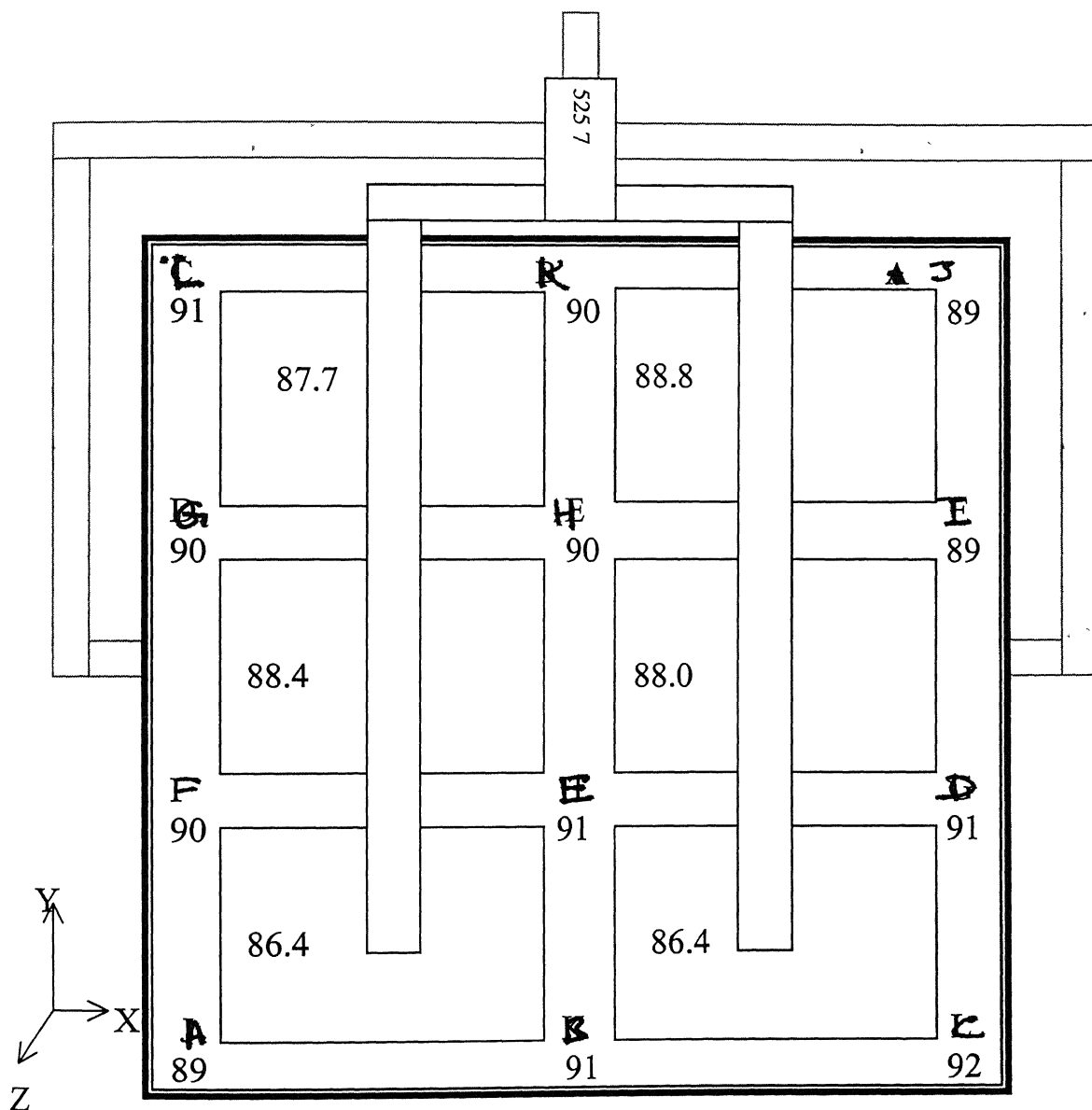


Fig. 5.4 Temperature distribution in simulated cell at mid height of the melt

5.3.1 Effect of Anode-Cathode Distance (ACD)

The horizontal components of current density are measured for three different ACDs (1.0, 1.5, and 2.0 cm) with other conditions remaining the same in the three experiments. As expected, the horizontal components of current are substantially decreasing with increase in ACD, as shown in Figs 5.2, 5.5 and 5.6. Horizontal current about the symmetry plane, i.e for points 'B', 'E', 'H' and 'K' are very less compare to that at other locations of the cell. Since the horizontal currents are responsible for high oscillations at the electrolyte/metal interface, increase in ACD damps the interface oscillations.

5.3.2 Effect of Total Current Input to the Cell

As shown in Figs. 5.7, and 5.8, the horizontal components (x and y) of current at points 'A', 'B', 'C', 'D' linearly vary with increase in total current input simply following the Ohm's law. It is to be noted the variations of X component at point B (Fig. 5.7) and Y component at point A (Fig. 5.8) have the negative slope of the linear curve indicating that the current flow is the reverse direction.

5.3.3 Effect of Cold Anode

Anodes in Hall cells are replaced every 10 to 20 days; typically, one anode would be replaced every day. When a new anode, which is at room temperature, is introduced into a cell, it is usual for this "cold anode" to carry little current until it heats up. Electrolyte freezes onto the anode. The frozen electrolyte being a poor conductor must melt off before the significant passage of current through this anode begins. The maldistribution of current caused by introducing the cold anode has long been thought to disturb the cell. The upset in the cell has been simulated by removing an anode from the anode assembly. As shown in Figs. 5.3, 5.9, and 5.10, horizontal current flows in reverse direction at a few points, which surround the cold anode, as compared to the 'base' case. This may be the primary cause of disturbances in the cell by the cold anode.

Current Density $\cong 0.9 \text{ A/cm}^2$

ACD = 1.5 cm

Current Density in Melt

(A/cm^2)

1 A/cm^2

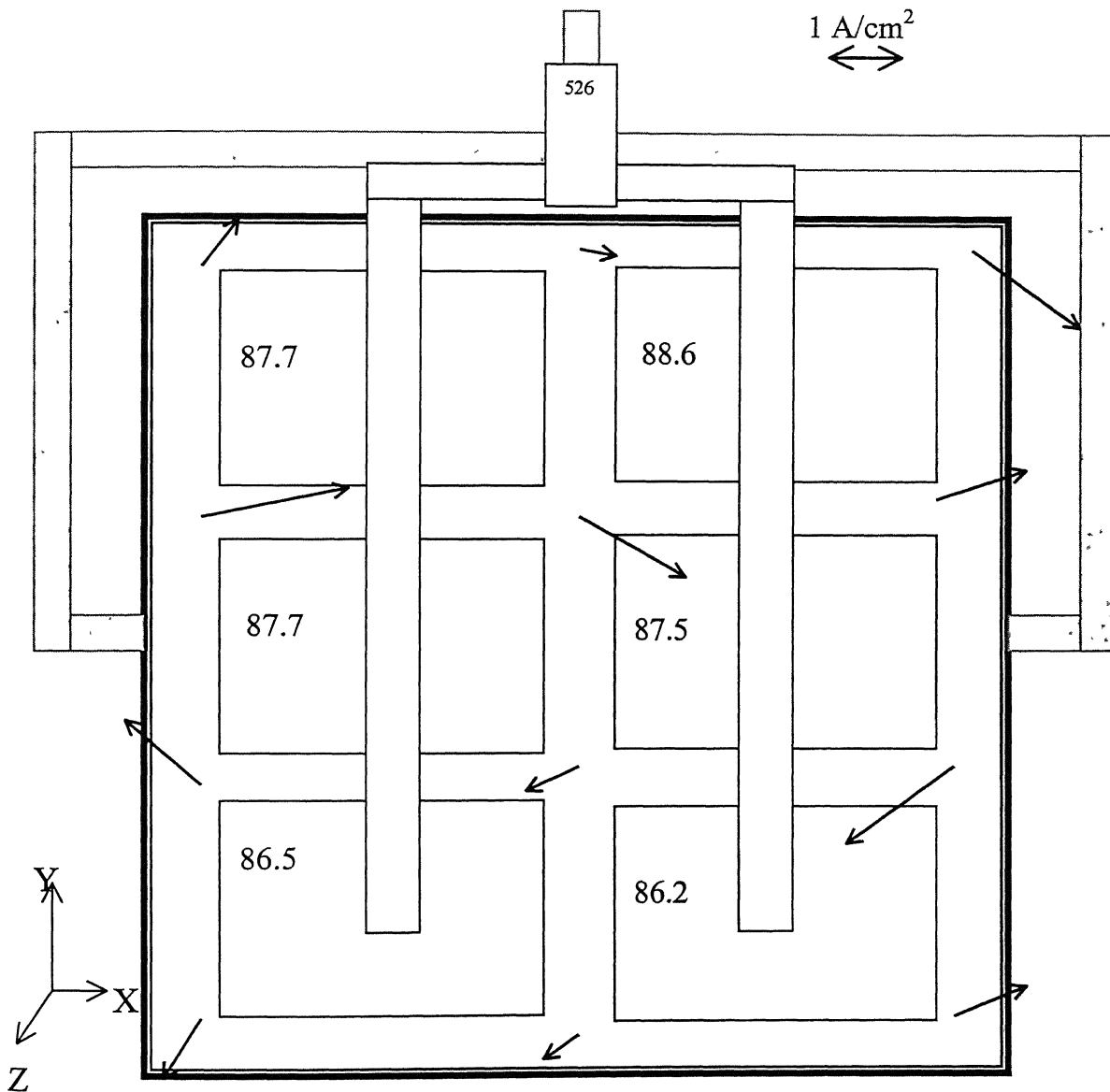


Fig. 5.5 Measured horizontal components of current densities.

Current Density $\cong 0.9 \text{ A/cm}^2$

ACD = 2.0 cm

Current Density in Melt

(A/cm^2)

1 A/cm^2

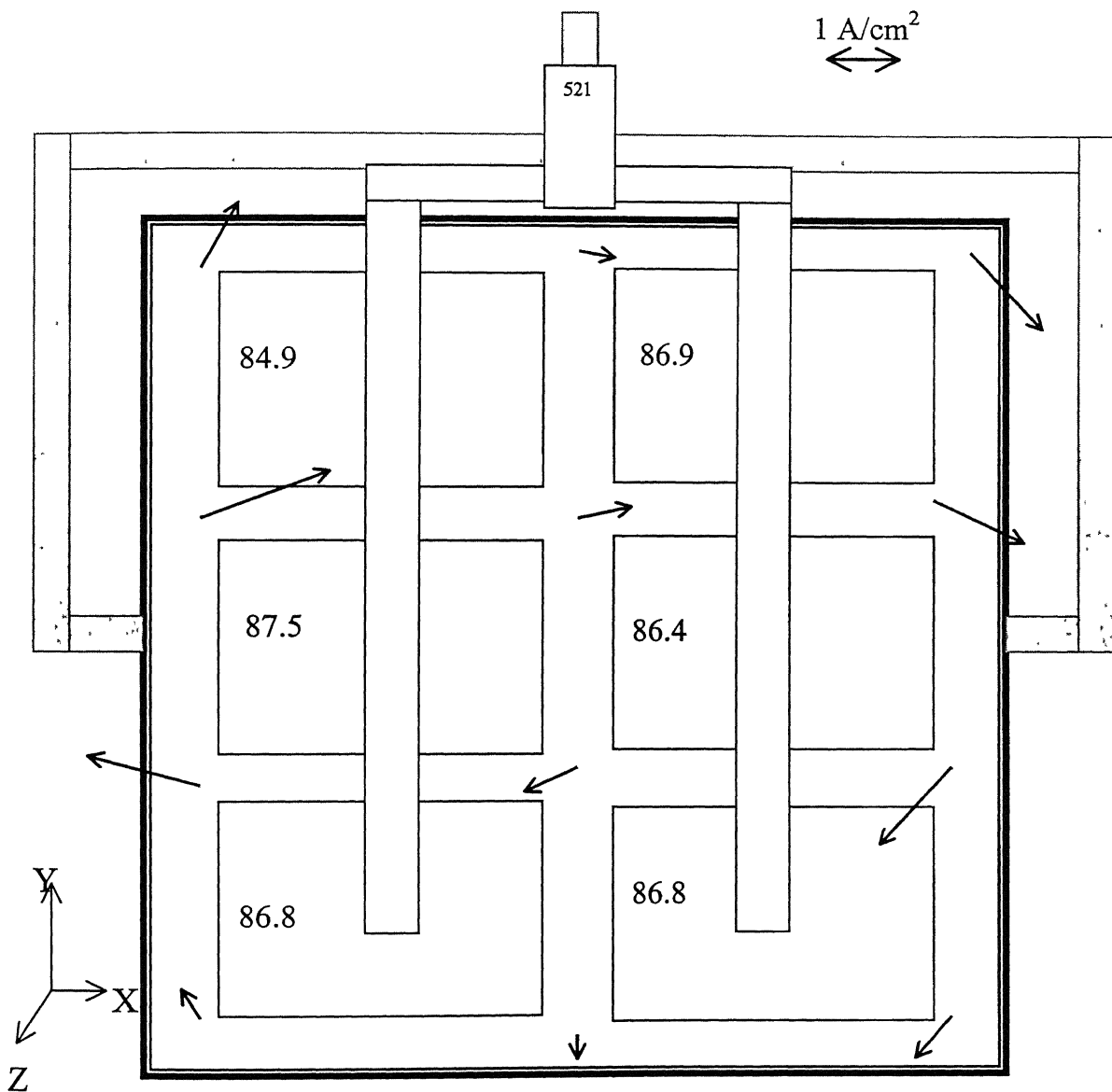


Fig. 5.6 Measured horizontal components of current densities.

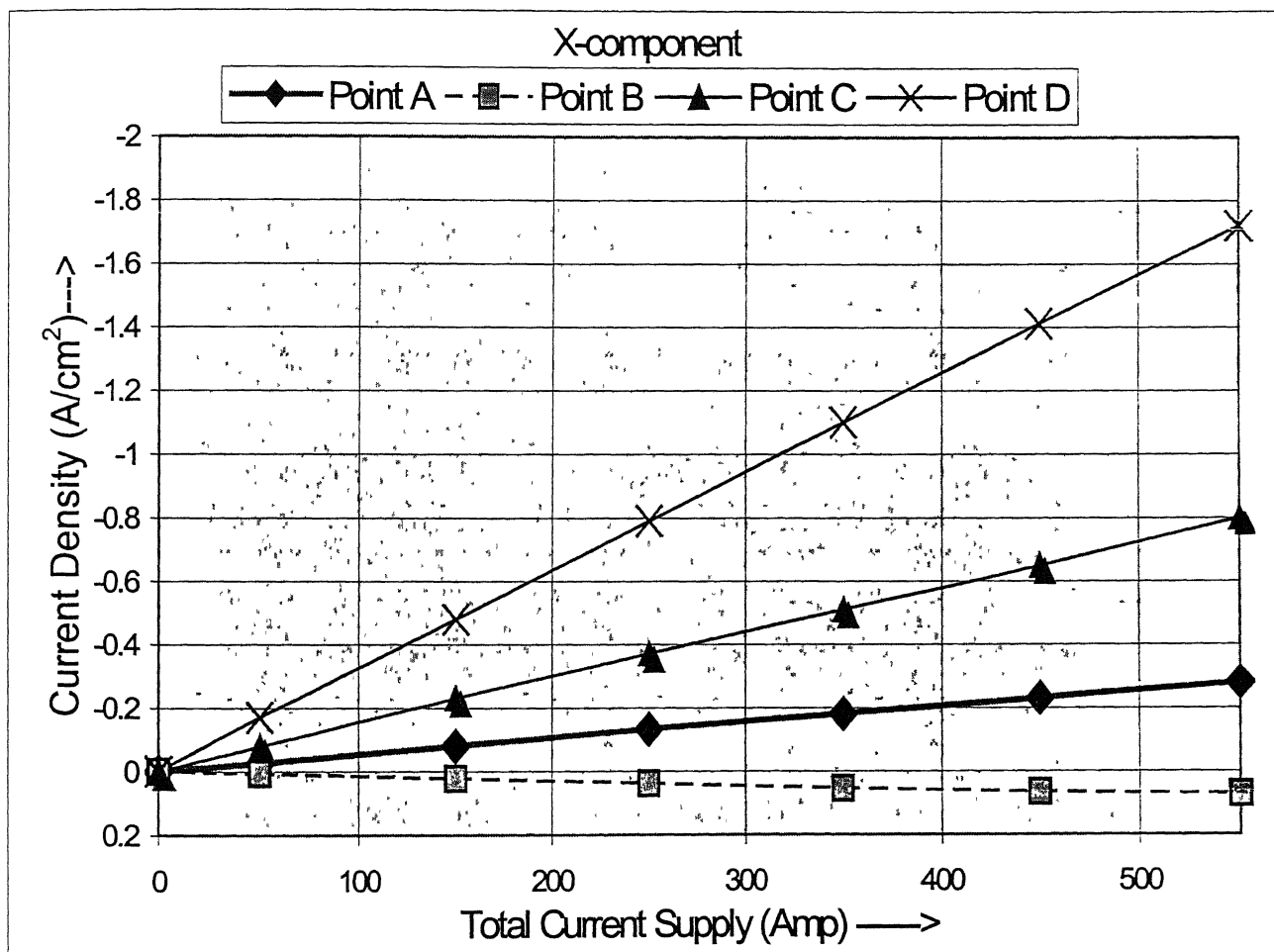


Fig. 5.7 Current density components within the melt with variation in current input.

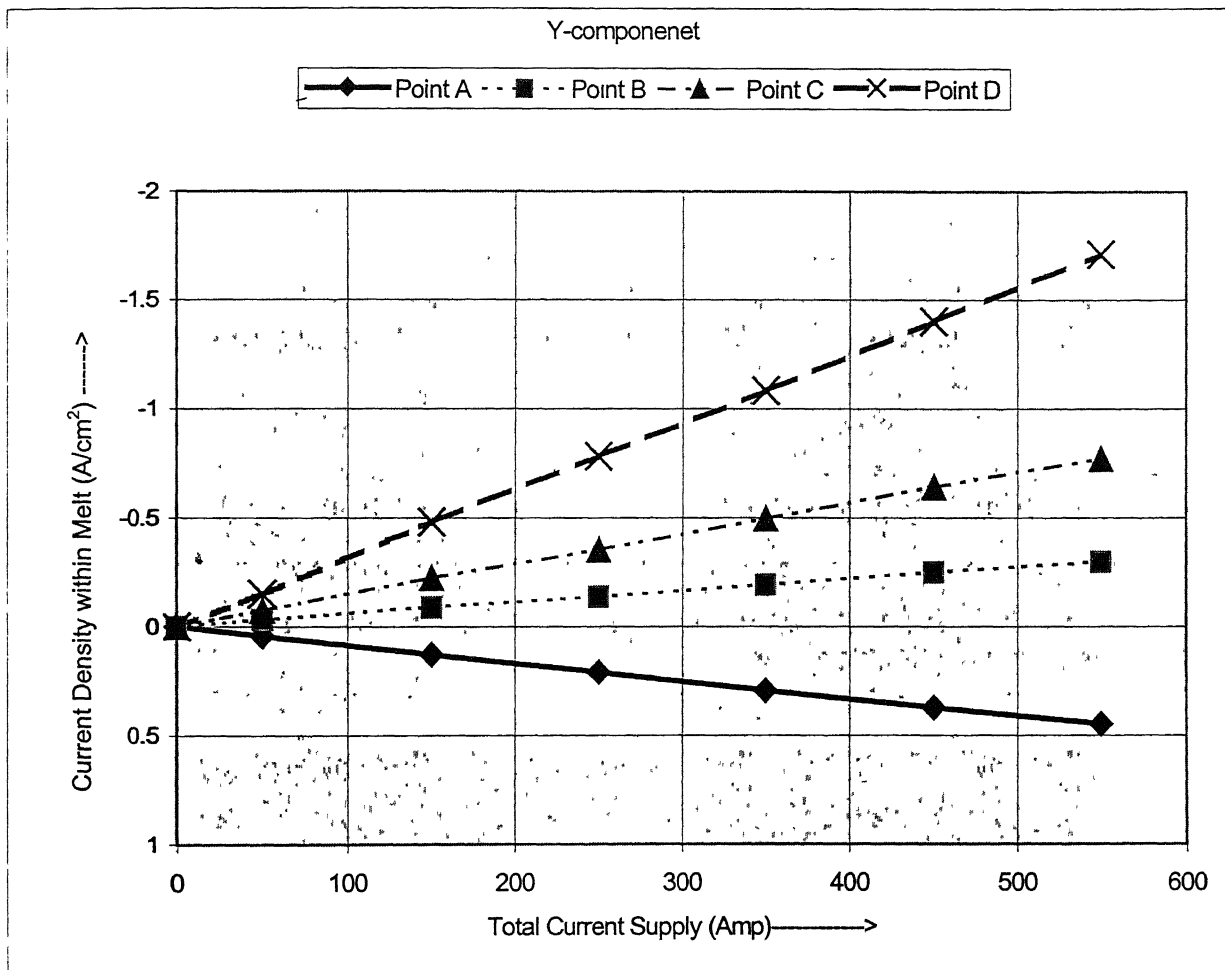


Fig. 5.8 Current density components within melt with variation in current input.

Current Density $\cong 1.08 \text{ A/cm}^2$

ACD = 1.0 cm

Current Density in Melt

(A/cm^2)

1 A/cm^2

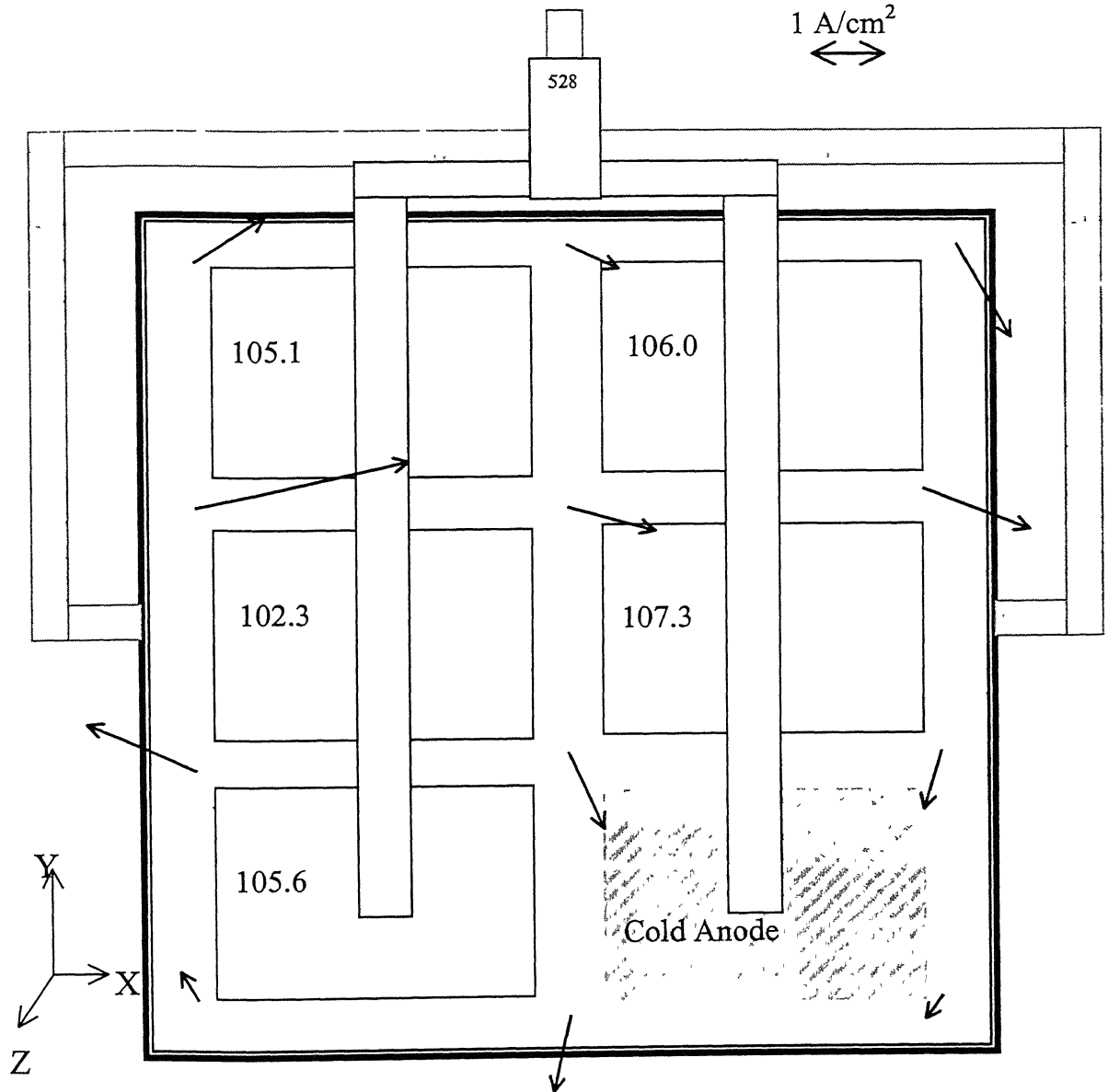


Fig. 5.9 Measured horizontal components of current densities for corner cold anode.

Current Density $\cong 1.08 \text{ A/cm}^2$

ACD = 1.0 cm

Current Density in Melt

(A/cm^2)

1 A/cm^2

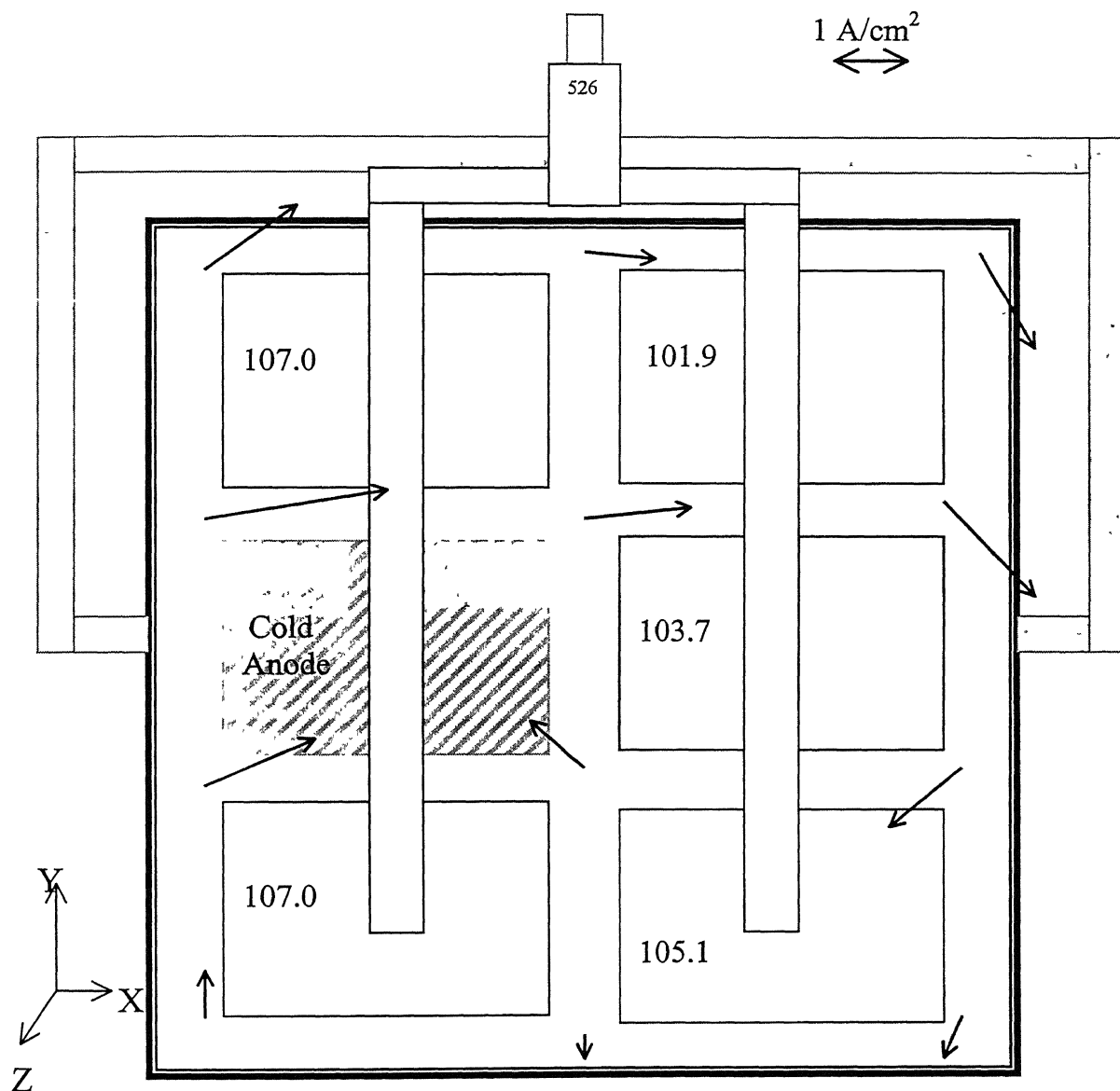


Fig. 5.10 Measured horizontal components of current densities.

5.4 MAGNETIC FIELD DISTRIBUTIONS

The convention followed in drawing the vertical magnetic field is that if the Broken Arrow is clockwise with respect to the solid arrow, the field is upward; if anti-clockwise, the field is downward. As expected, the overall horizontal components (B_x and B_y) of the magnetic field are approximately clockwise, following the right hand rule at most points barring a few exceptions. At current entry side, the vertical component (B_z) is much higher due to high current flow in anodic bus bars in the end riser design. The magnitude of vertical component of magnetic field (B_z) in the quarter riser design is significantly lower than the end riser design, as expected from the designs of bus bars. The overall magnetic field in the quarter riser design is lower than that in the end riser design. Magnetic field in the quarter riser design is approximately 90° anti-clockwise as compare to the end riser design. The reason for 90° anti-clockwise rotation of magnetic field is that while the current flows in the same direction in anodic and cathodic bus bars in the quarter riser design, in the end riser design the flow is in the opposite direction in the cathodic and anodic bus bars.

5.4.1 Effect of Current Density

As shown in Figs. 5.11, and 5.12, magnetic field increases linearly with increase in current density. Table 5.4 also shows the same trend. This is conformity with Biot-Savert law, which states that the magnetic field is directly proportional to the current supply.

5.4.2 Effect of Anode-Cathode Distance (ACD)

The ACD variation has only little effect on magnetic field, as shown in Figs. 5.12, and 5.13, respectively for two different ACDs.

5.4.3 Effect of Cold Anode

Current distribution in the cold anode case changes due to sharing of current of the cold anode by the remaining anodes. Magnetic field near the vicinity of the cold anode changes substantially as compared to the other parts of the cell, as shown in Figs. 5.11, 5.14, and 5.15. Vertical components of magnetic field are lower in the cold anode case

as shown in Figs.5.14, and 5.15. The patterns are more or less clockwise, that is the same as in the 'base' case. Compare to the 'base' case, horizontal component of magnetic field rotates 60-80° anti-clockwise in the cold anode case. There is a substantial change in magnetic field in immediate vicinity of the cold anode, the pattern is anti-clockwise in this portion of the cell, as shown in the Figs 5.14, and 5.15. The likely reason for this behavior is the absence of anode bar current in the cold anode case.

Table 5.4 Variation of magnetic field(Gauss) with current density. ($Z=0.5\text{cm}$)

Point	Current Density 0.5 A/cm ²			Current Density 0.7 A/cm ²			Current Density 0.9 A/cm ²		
	Bx	By	Bz	Bx	By	Bz	Bx	By	Bz
A	0.0	0.5	2.1	-1.0	0.5	2.6	-0.2	0.8	3.2
B	-0.4	0.2	0.1	-0.6	0.4	0.2	-1.1	0.6	0.6
C	-0.6	-0.2	-2.1	-0.8	-0.3	-3.2	-1.4	0.7	-3.3
D	-0.3	-0.2	-1.4	-0.2	0.5	-2.3	-1.3	-1.0	-2.6
E	0.5	-0.2	0.0	1.1	0.8	1.4	0.2	-0.4	0.6
F	0.3	0.2	0.6	0.5	0.5	1.4	0.7	0.6	1.9
G	2.3	-0.4	-1.2	2.6	-1.5	-2.2	4.2	-0.8	-3.6
H	1.5	-1.4	0.8	2.6	-2.7	0.8	3.5	-2.5	1.1
I	1.8	-2.1	3.3	2.0	-2.9	5.2	2.1	-4.4	6.8
J	2.3	-0.9	5.5	3.0	-2.2	8.0	4.2	-2.1	10.3
K	2.7	-1.9	1.0	3.3	-2.8	2.4	5.1	-4.4	1.3
L	2.5	-1.2	-4.0	2.8	-1.5	-5.2	2.6	-2.5	-8.7

5.4.4 Effect of Height from Base of the Cell

To investigate the effect of melt depth (height from the base of the cell) on magnetic field, the measurements have been made at three horizontal planes at different heights: $Z=0\text{ cm}$ (base of the cell), $Z=1.75\text{ cm}$ (mid plane of the melt), and $Z=3.5\text{ cm}$ (top of

ACD = 1.0 cm

Current density $\cong 0.9 \text{ A/cm}^2$

$Z = 0.5 \text{ cm}$

—————→ Horizontal component

- - - - -→ Vertical component

1 Gauss

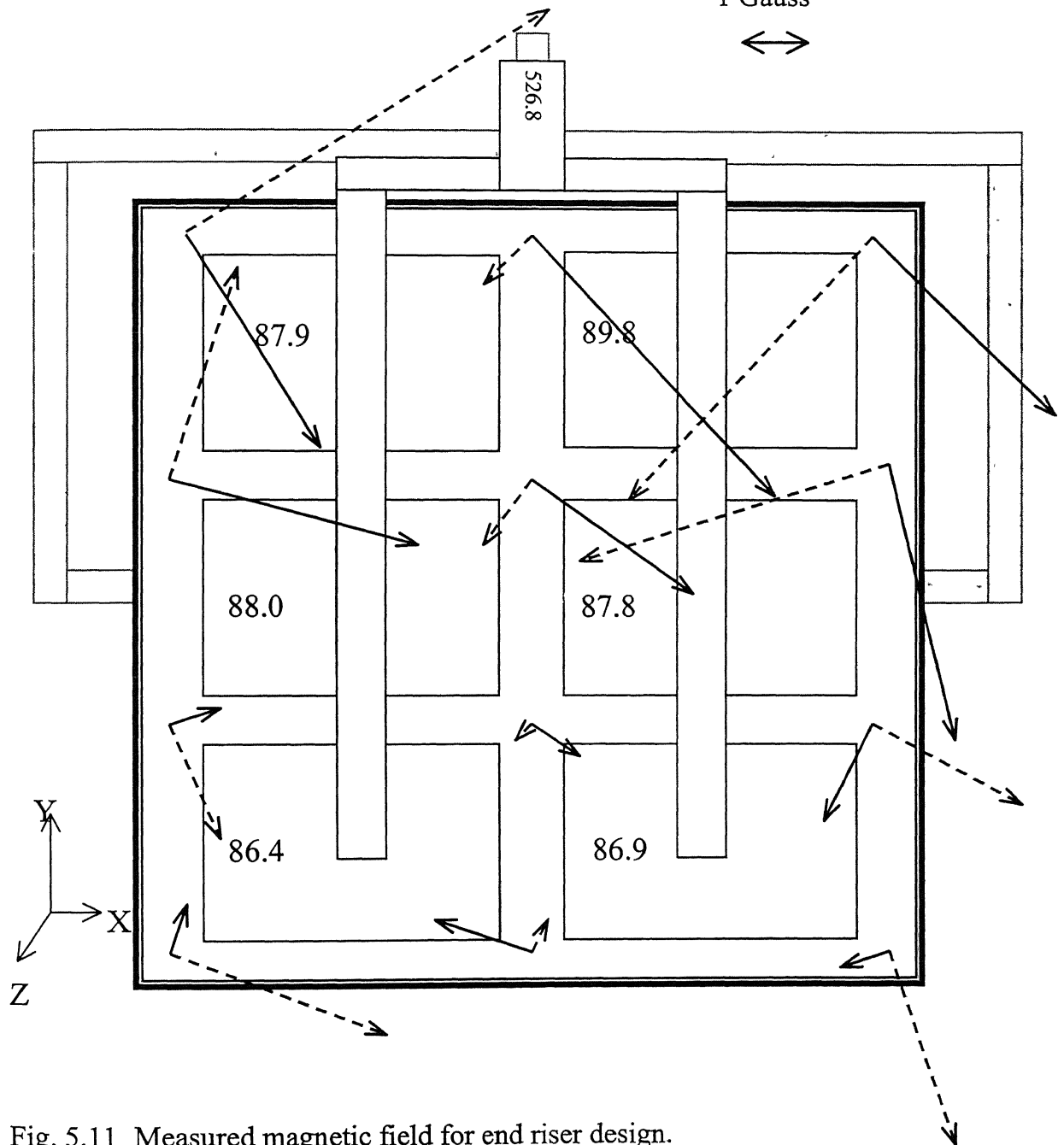


Fig. 5.11 Measured magnetic field for end riser design.

ACD = 1.0 cm

Current density $\cong 0.5 \text{ A/cm}^2$

$Z = 0.5 \text{ cm}$

—————→ Horizontal component

- - - - -→ Vertical component

1 Gauss

↔

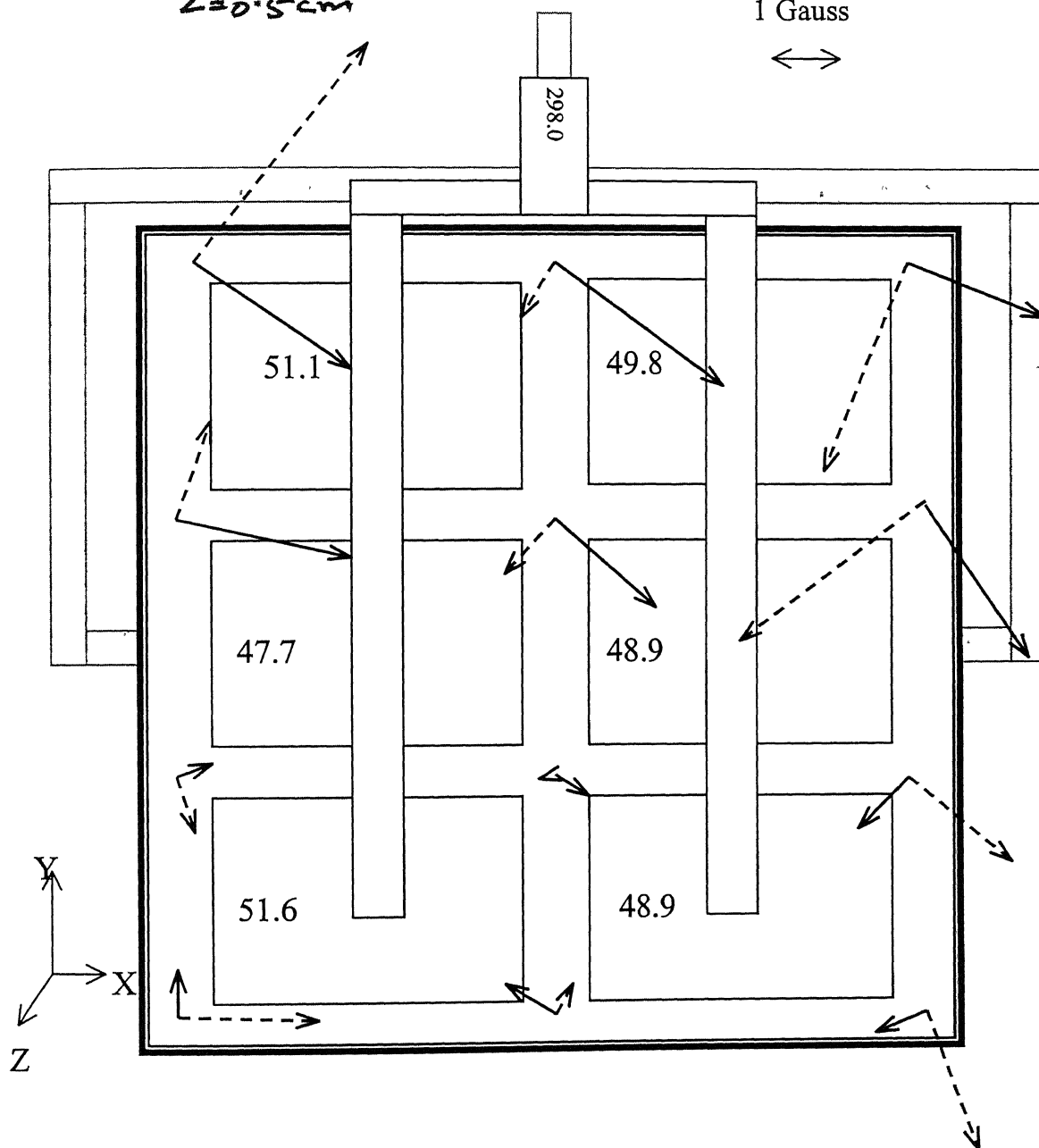


Fig. 5.12 Measured magnetic field for end riser design.

ACD = 2.0 cm

Current density $\cong 0.5 \text{ A/cm}^2$

$Z = 10 \text{ cm}$

—→ Horizontal component

- - - - -→ Vertical component

1 Gauss

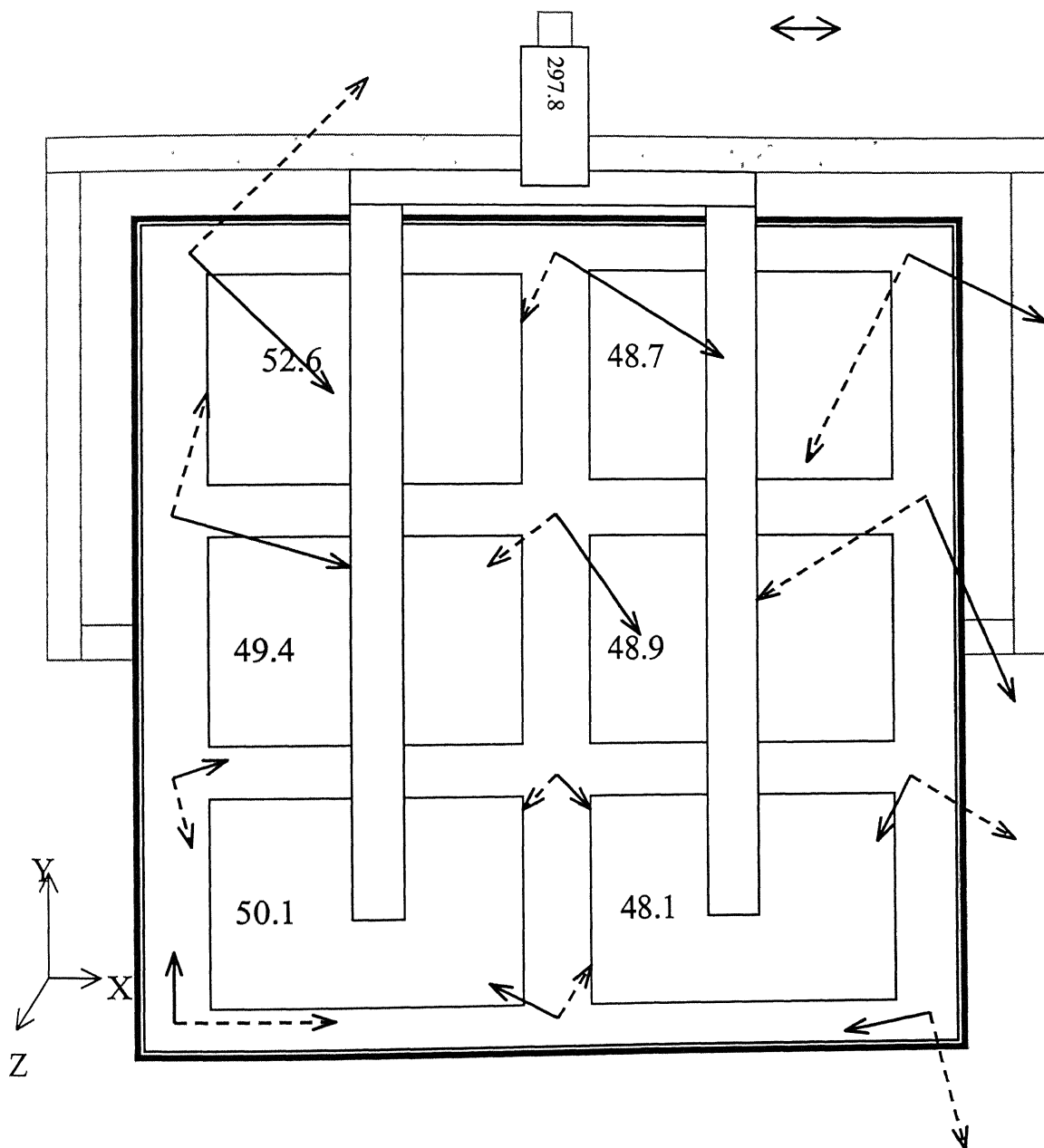


Fig. 5.13 Measured magnetic field for end riser design.

ACD = 1.0 cm

Current Density $\cong 1.08 \text{ A/cm}^2$

$Z = 0.5 \text{ cm}$

—————> Horizontal component

- - - - -> Vertical component

1 Gauss

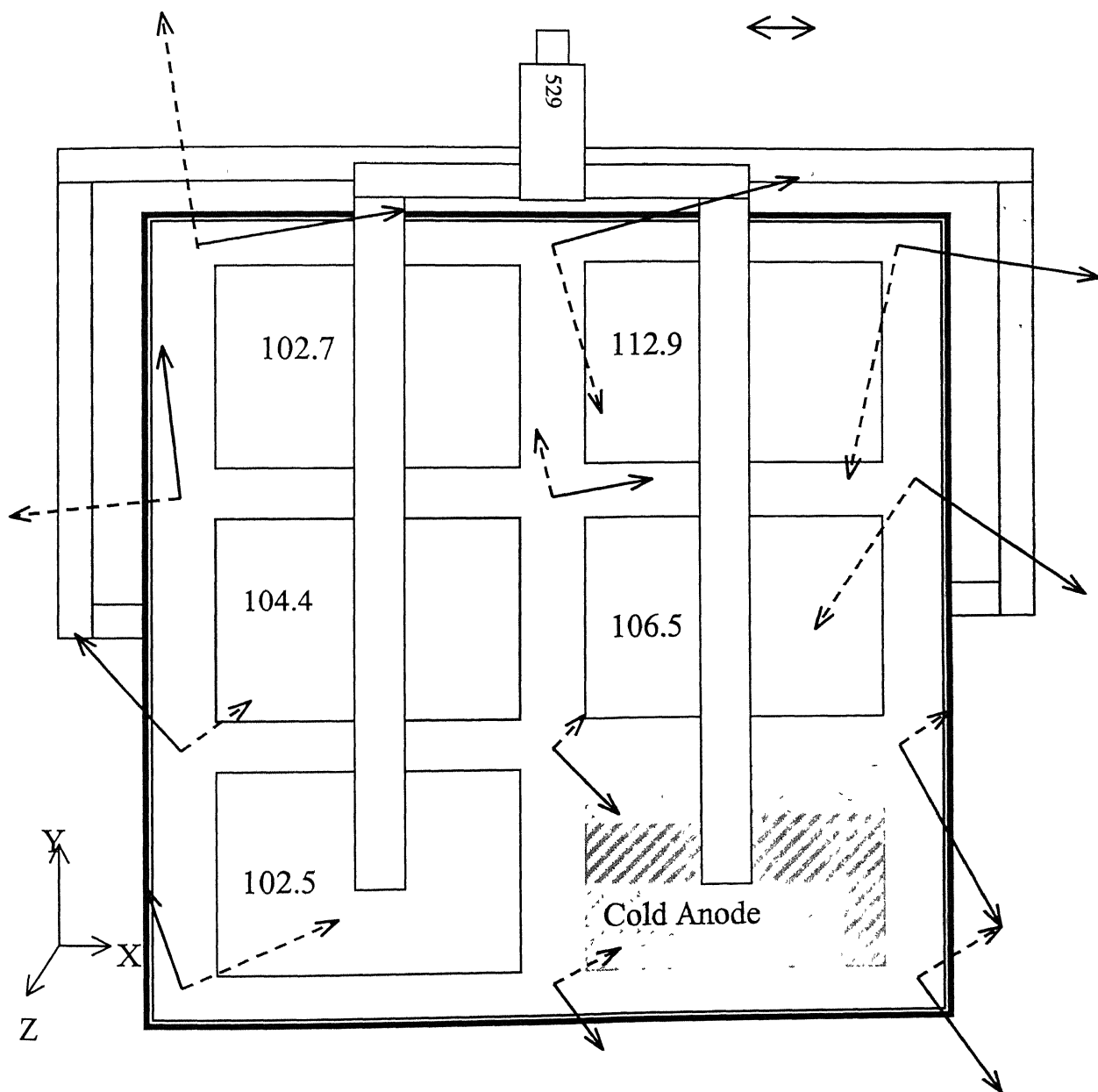


Fig. 5.14 Measured magnetic field for corner cold anode case.

ACD = 1.0 cm

Current density $\cong 1.08 \text{ A/cm}^2$

$z = 0.5 \text{ cm}$

—————→ Horizontal component

- - - - -→ Vertical component

1 Gauss

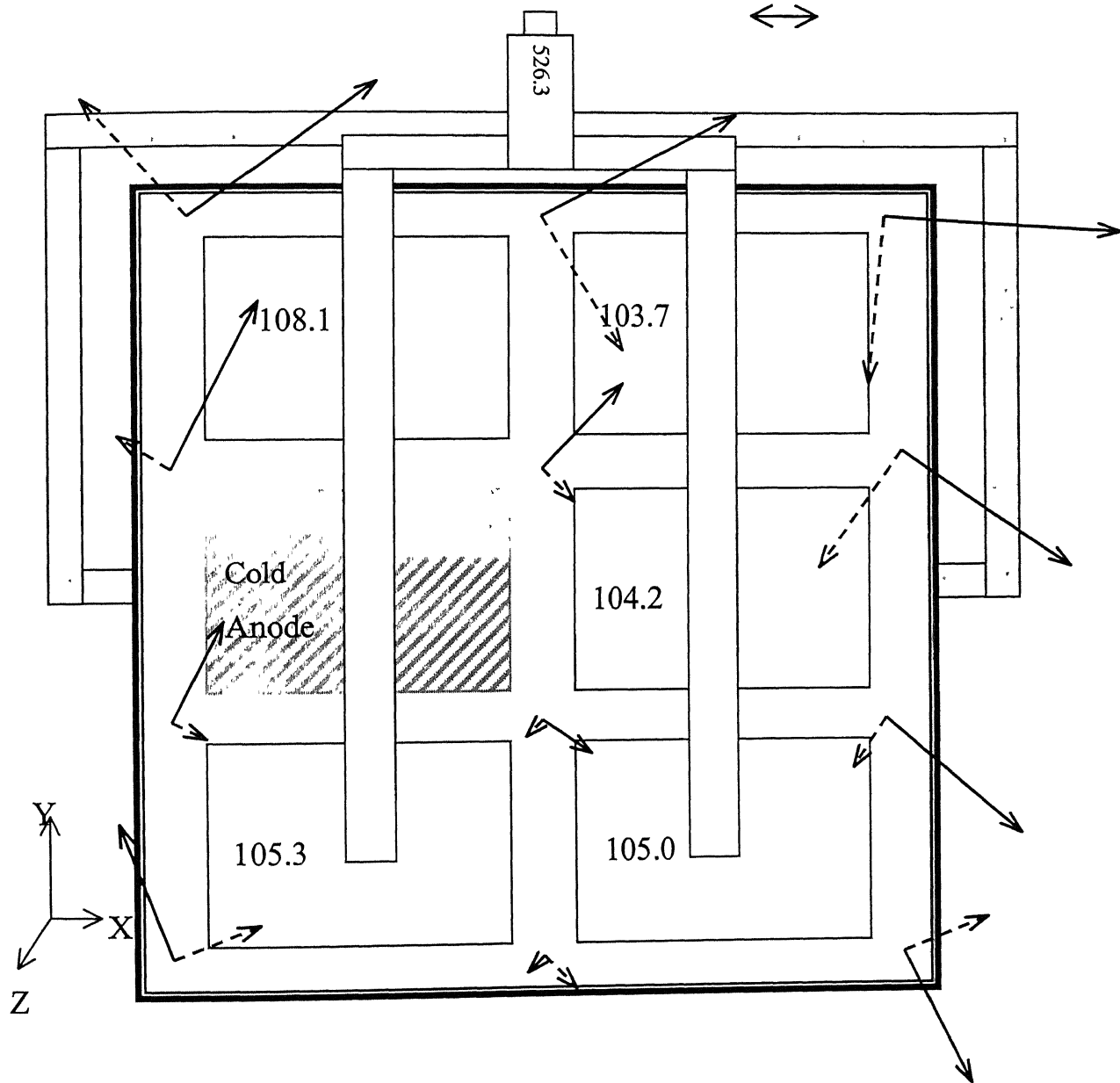


Fig. 5.15 Measured magnetic field for middle cold anode case.

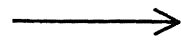
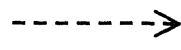
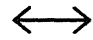
the melt). Current density in all the three experiments is kept at 0.9 Amp/cm^2 , and the ACD is 1.0 cm. The results are shown in Figs. 5.16-5.18. Horizontal component of magnetic field increases with increase in distance from the base of the cell. Vertical component of magnetic field, however, decreases with increase in distance from the base of the cell. The reason for this trend is that by thumb rule magnetic field is in the form of a circular loop around a conductor. At $Z=0$, the Z-axis is tangential to the field produced by the cathode collector bars. This gives large vertical but small horizontal magnetic fields. But when the height increases the Z-axis is not tangential to the magnetic field produced and magnitude of the vertical component decreases and horizontal component increases.

5.4.5 Effect of Bus Bar Design

As mentioned above, the two designs are investigated here: one is the end riser design, and the other is quarter riser. Measured magnetic fields are shown in Figs. 5.11, 5.14, and 5.15 for the end riser design, and in Figs. 5.19, 5.20, and 5.21 for the quarter riser design. Distribution of magnetic field in the quarter riser design is such that it gives low magnetic field as compared to that in the end riser design. Magnetic field is approximately 90° anti-clockwise in the quarter riser design as compared to the end riser design. Further, magnetic field in the quarter riser design is more uniform than that in the end riser design. Magnetic field components, near the current entry side, are much higher than the other side in end riser design. The reason for this is that current flows in the anode bus bar and the collector bar are in the opposite directions, which make constructive situation for magnetic field in that portion. In case of the quarter riser design, vertical component of magnetic field is much lower than that in the end riser design. This is due to the fact that the current flows in the anode bus bar and the collector bar in the quarter riser design are in the same direction, which makes destructive situation for magnetic field at mid plane. Other reason for this behavior is that the current flows in the anodic bus bars have low magnitudes in the quarter riser design than that in the end riser design. The repositioning of bus bars not only results in a change of current distribution but also reversing the direction of current flows,

ACD = 1.0 cm

Current density $\cong 0.9 \text{ A/cm}^2$

 Horizontal component
 Vertical component
 1 Gauss 

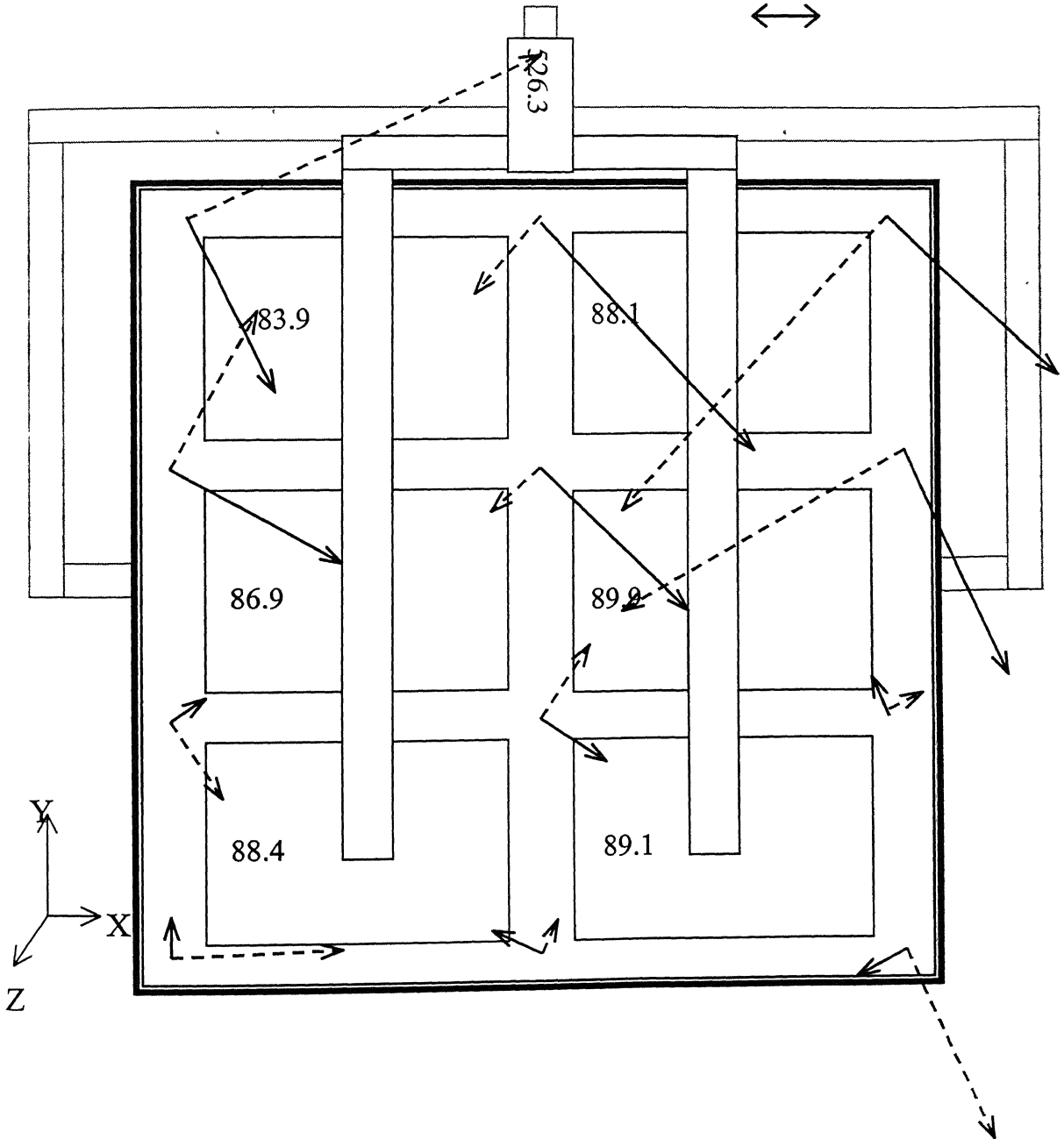


Fig. 5.16 Measured magnetic field at $Z=0 \text{ cm}$ (base of the cell) for the end riser design.

ACD = 1.0 cm

Current density $\cong 0.9 \text{ A/cm}^2$

—————> Horizontal component

- - - - -> Vertical component

1 Gauss

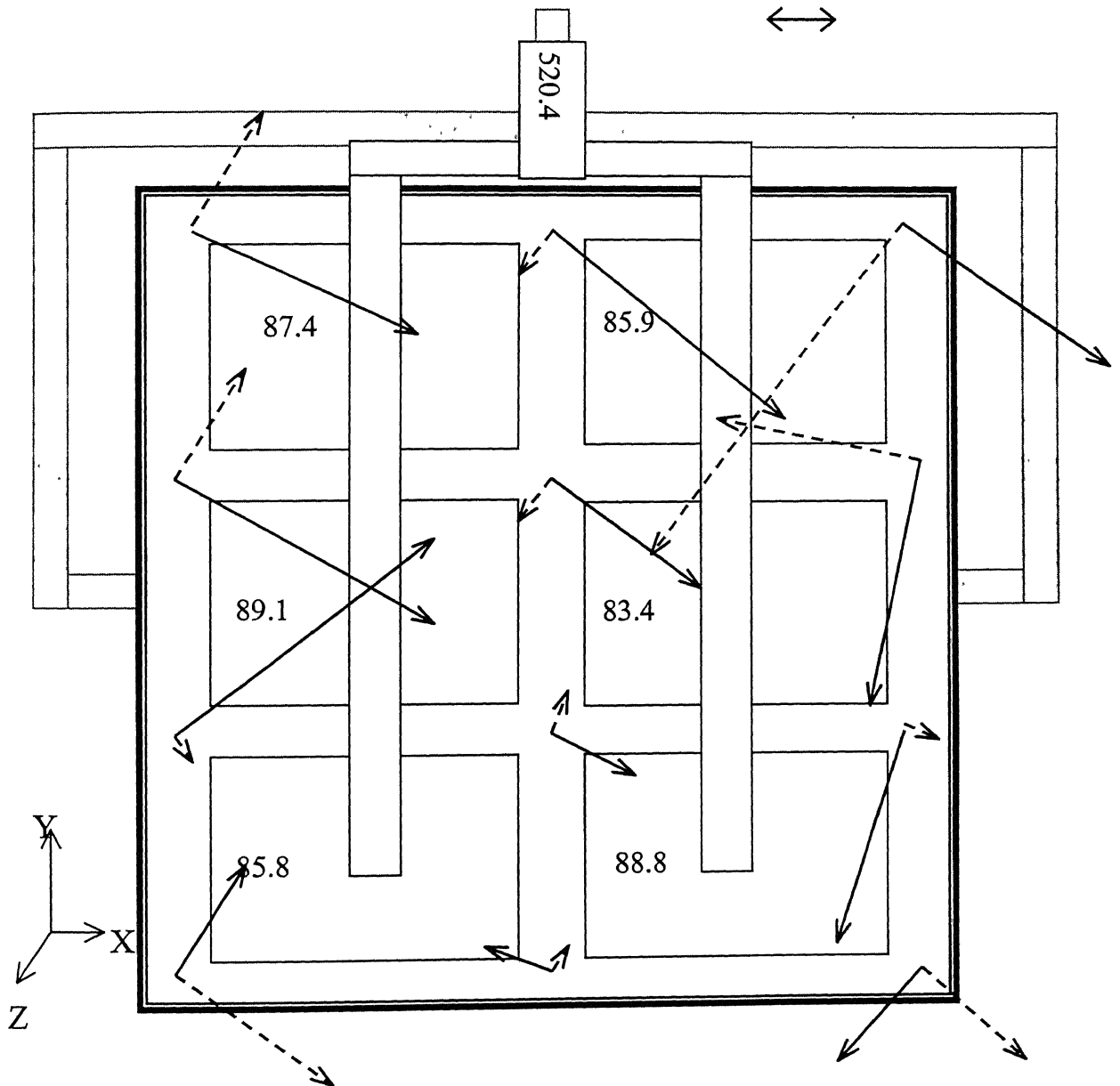


Fig. 5.17 Measured and magnetic field at $Z=1.75 \text{ cm}$ (middle plane of the melt) for the end riser design.

ACD = 1.0 cm

Current density $\cong 0.9 \text{ A/cm}^2$

—————> Horizontal component

- - - - -> Vertical component

1 Gauss

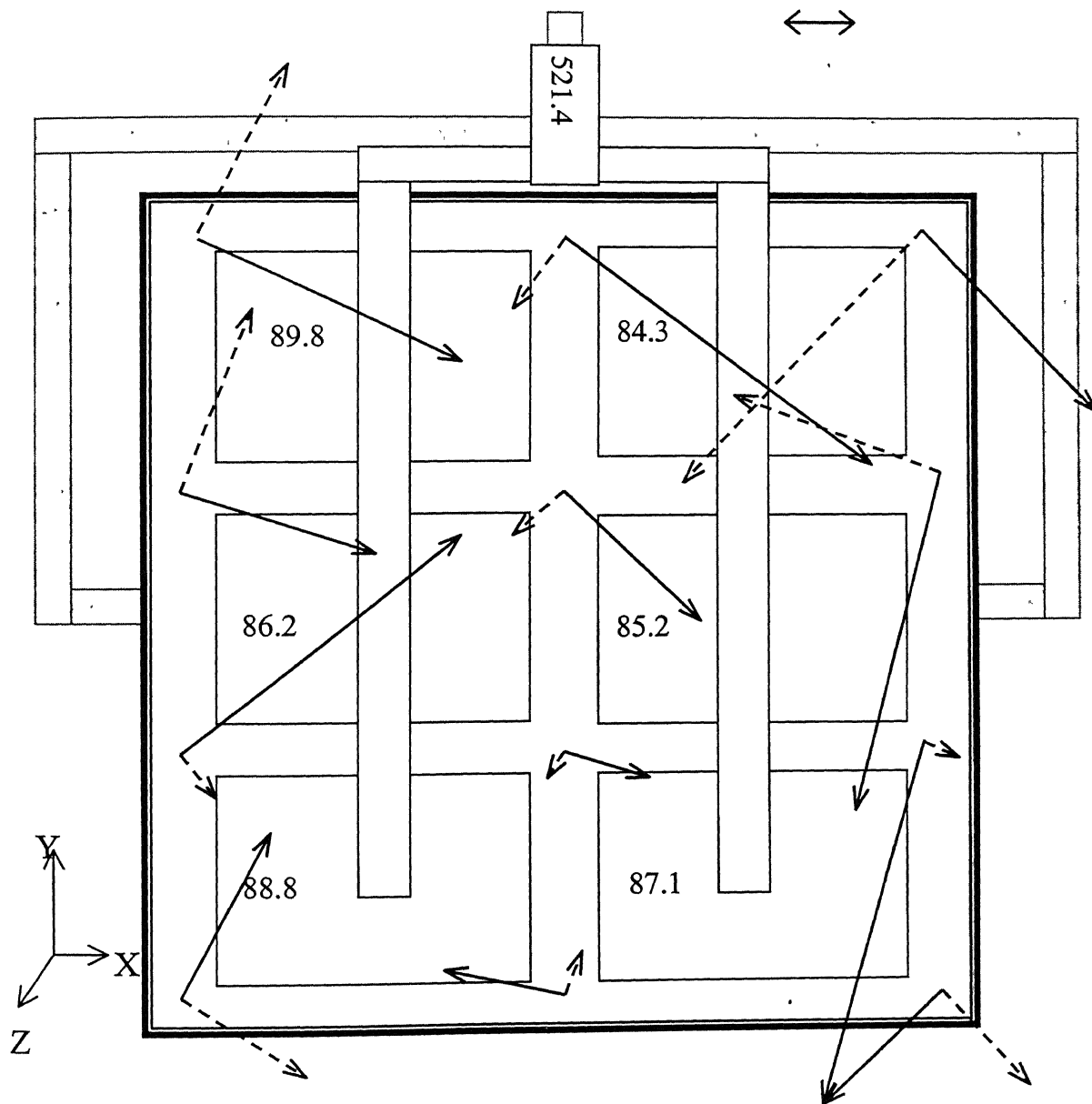


Fig. 5.18 Measured magnetic field at $Z=3.5 \text{ cm}$ (top plane of the melt) for the end riser design.

ACD = 1.0 cm

Current density $\cong 0.9 \text{ A/cm}^2$

$Z = 0.5 \text{ cm}$

—————→ Horizontal component

- - - - -→ Vertical component

1 Gauss

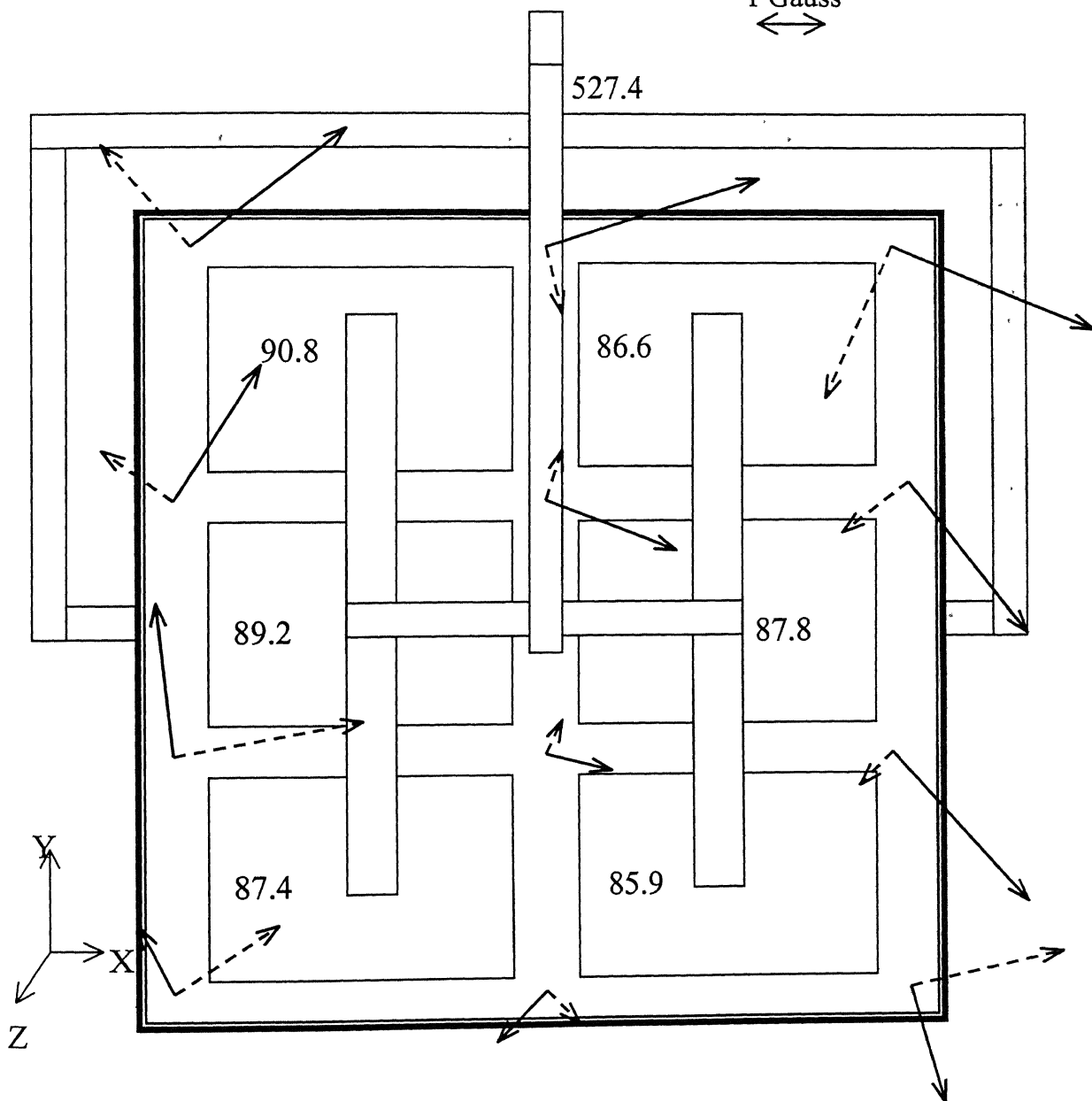


Fig. 5.19 Measured magnetic field for the quarter riser design.

ACD = 1.0 cm

Current density $\cong 1.08 \text{ A/cm}^2$

$Z = 0.5 \text{ cm}$

—————→ Horizontal component

- - - - -→ Vertical component

1 Gauss
↔

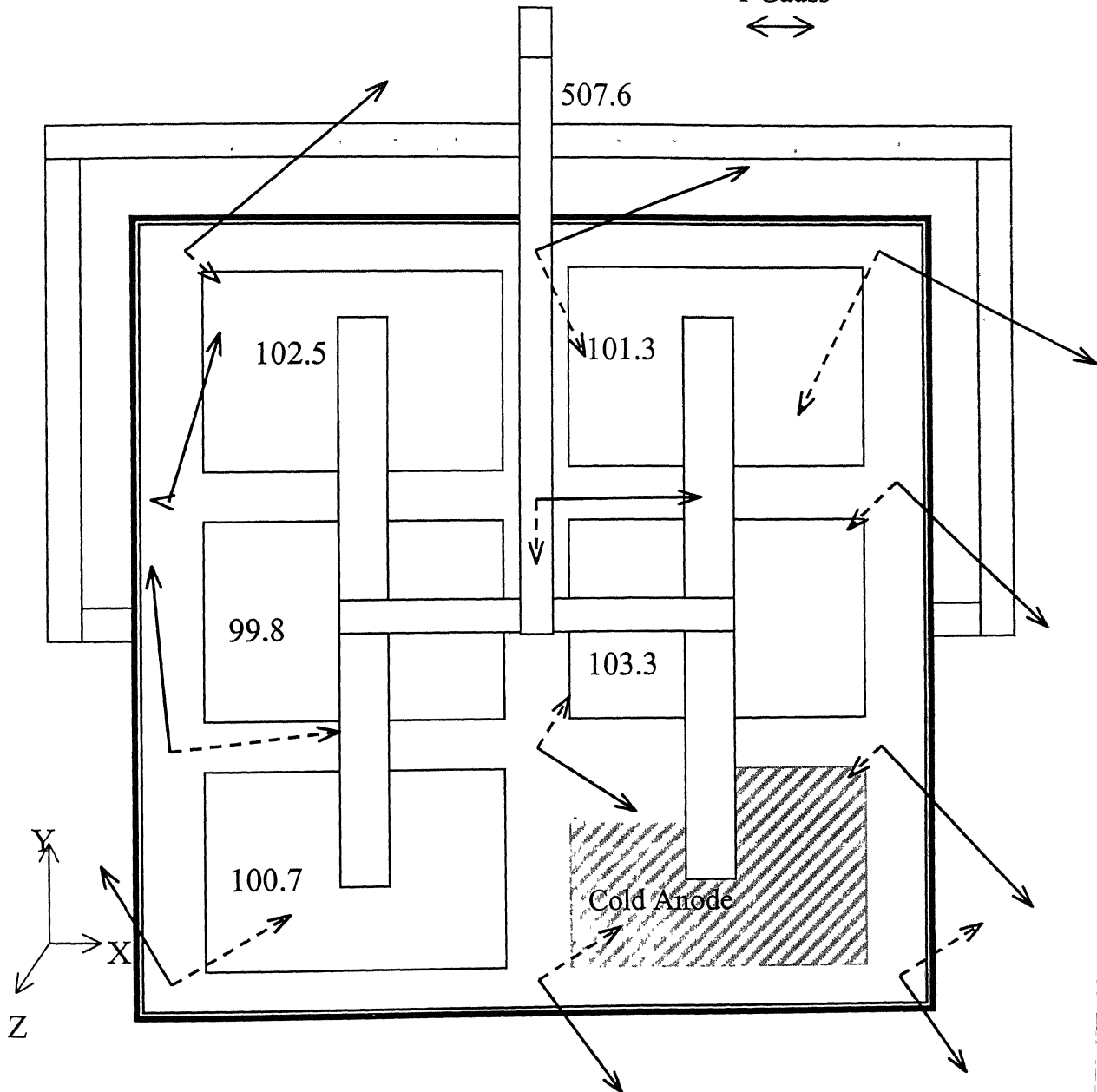


Fig. 5.20 Measured magnetic field for the quarter riser design.

ACD = 1.0 cm

Current density $\cong 1.08 \text{ A/cm}^2$

$Z = 0.5 \text{ cm}$

—————> Horizontal component

- - - - -> Vertical component

1 Gauss

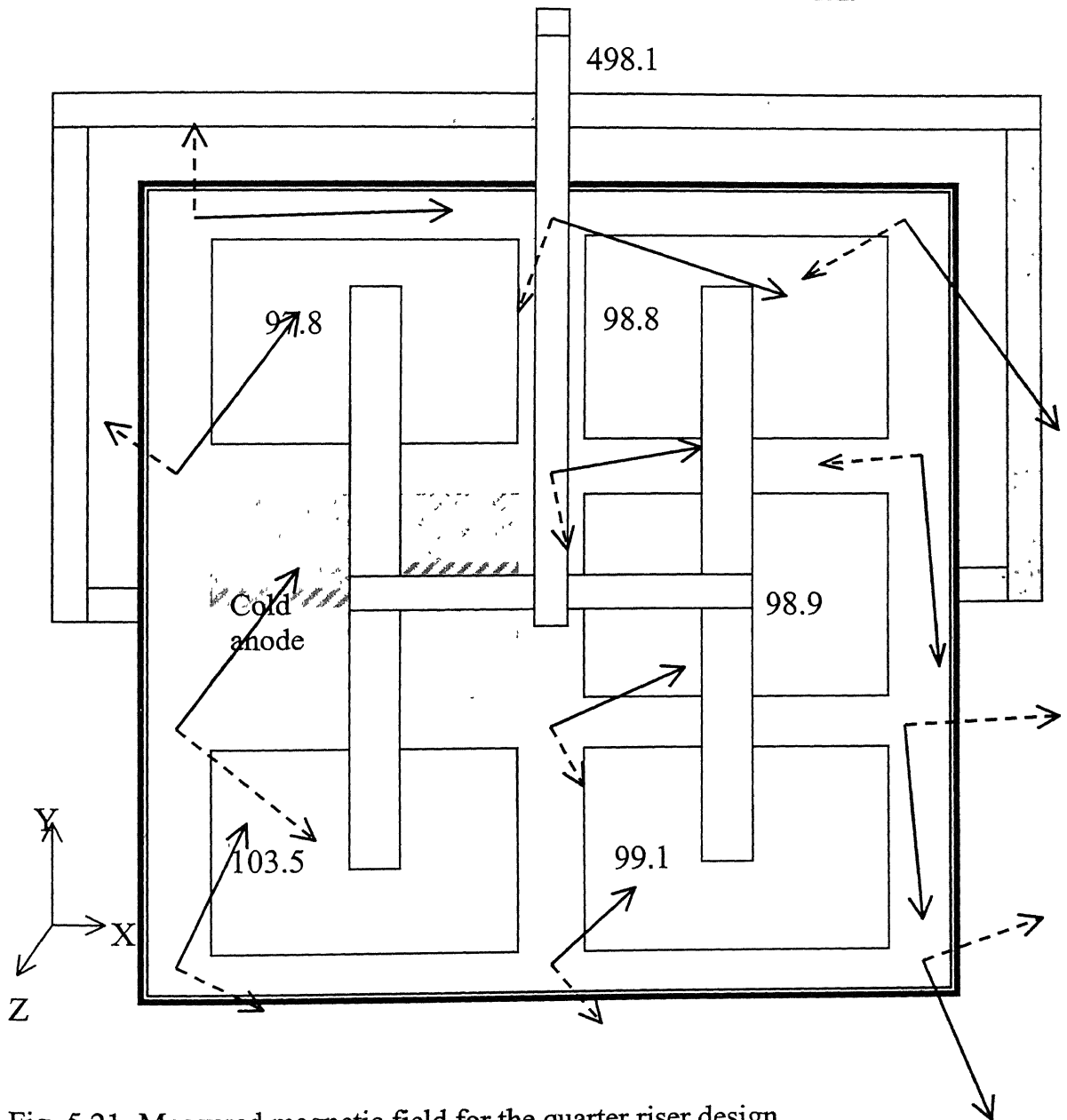


Fig. 5.21 Measured magnetic field for the quarter riser design.

decreasing magnetic field both in the vertical as well as in the horizontal directions. The reason for more uniform magnetic field in the quarter riser design is the uniformity in the current flow as compared to the end riser design.

5.5 VELOCITY PROFILE

Velocities are measured with help of the velocity probe as described in Chapter 4. Velocity is measured with different ACDs, cold anode cases, current distribution, and for two different bus bar designs. The effect of the various parameters on velocity are described below:

5.5.1 Effect of Current Density

Variations in measured velocities, at different locations, with variations in the current input to the cell are as shown in Figs. 5.22-5.24. As expected, velocity is more or less directly proportional to the square of the total current input. This observation is in conforming with the work of Evans et al. [28], which suggests that the electromagnetically driven flow in Hall cells is determined by a balance between the electromagnetic driving forces and the drag forces. This leads to the conclusion that the melt velocity is proportional to the electromagnetic driving force, and, therefore, square of the cell current.

5.5.2 Effect of ACD

Results show that velocity increases with increase in ACD as shown in Fig. 5.25. The increase in velocity with ACD shows that velocity increases more rapidly as ACD increases from 1.5 to 2.0 cm as compared to the increase from 1.0 to 1.5 cm. Horizontal currents are higher in case of lower ACDs and are responsible for turbulence and swirl in melt. But in other hand, the lower ACD increases the drag force, which damps the turbulence and swirl in the cell. So here the drag forces are more predominant than other forces, which causes decrease in the melt velocity with decrease in ACD. Results of this investigation are in agreement with the computed results of Fortien et al.[27], showing that an increase in the ACD decreases drag force.

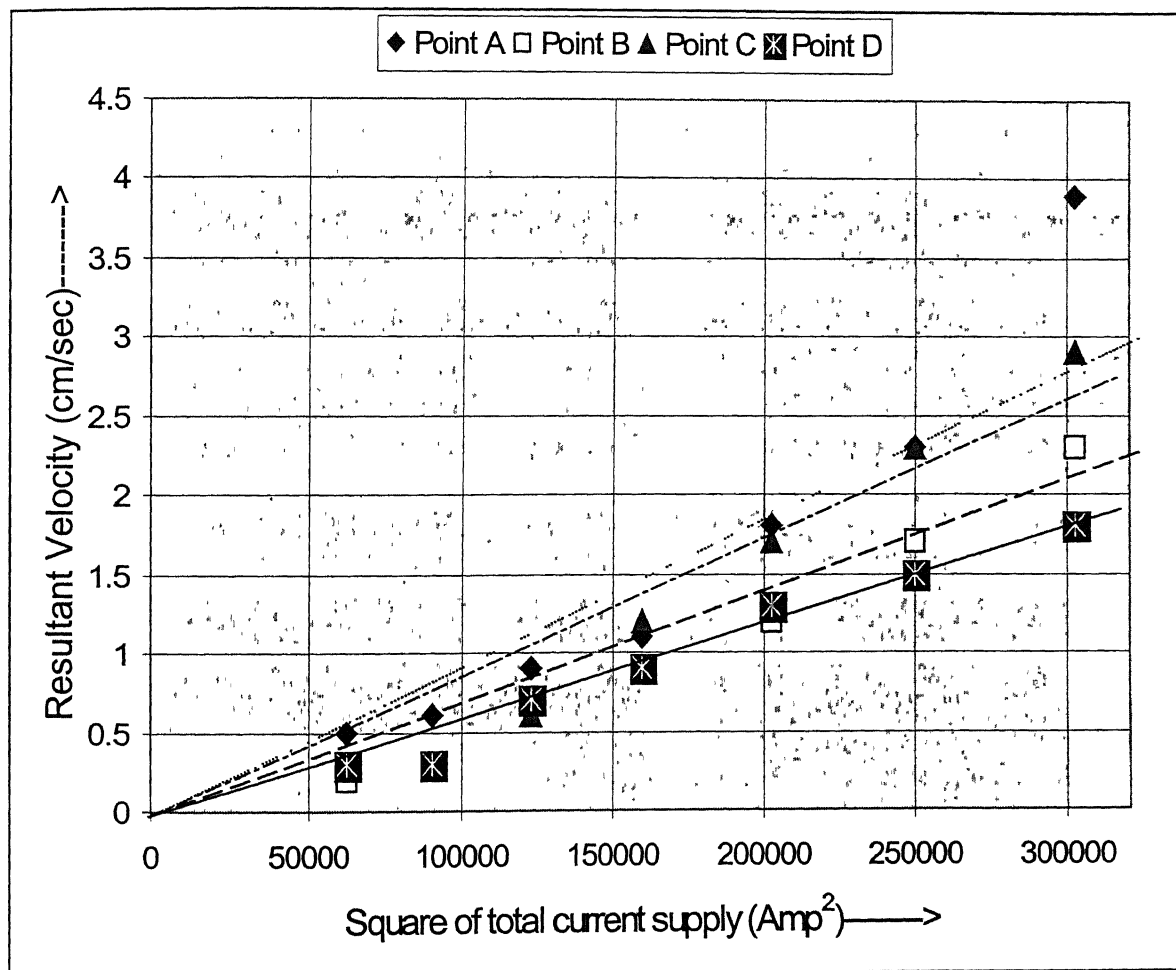


Fig. 5.22 Square of total current input verses resultant velocity graphs for points 'A', 'B', 'C' and 'D'.

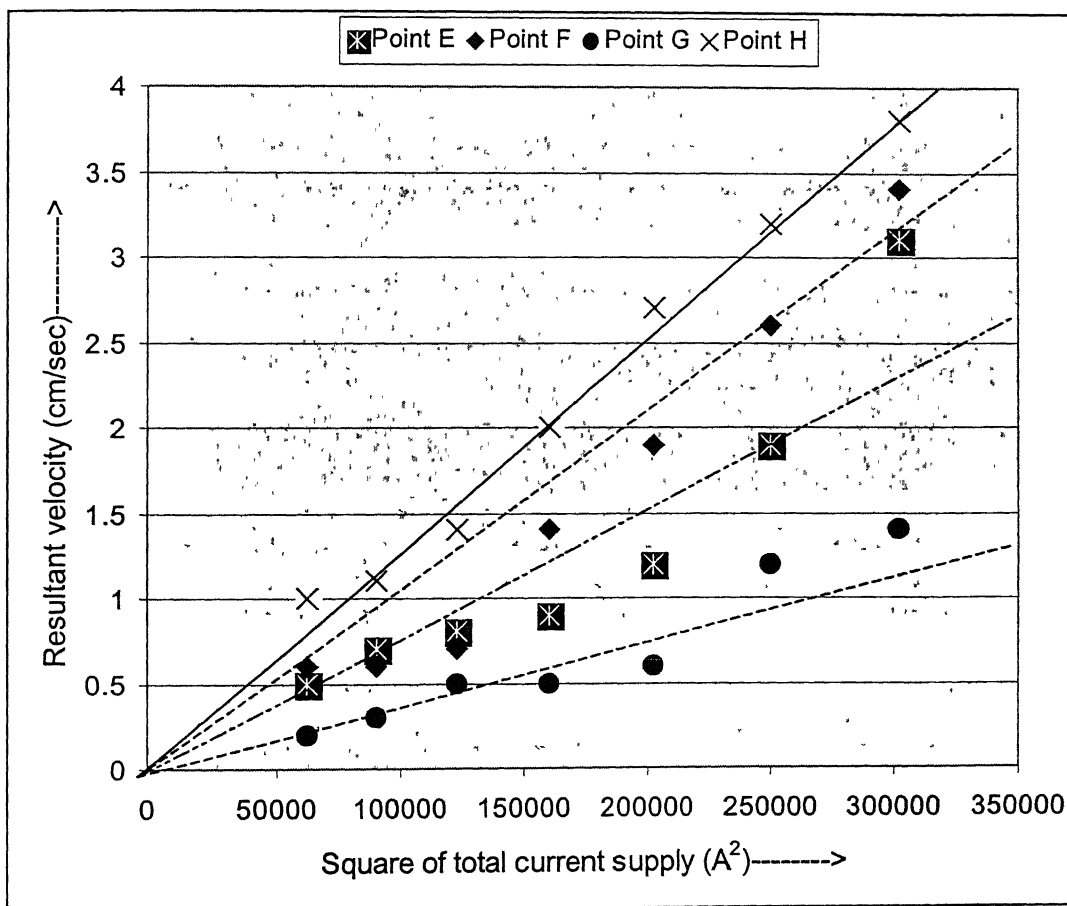


Fig. 5.23 Square of total current input verses resultant velocity graphs for points 'E', 'F', 'G' and 'H'.

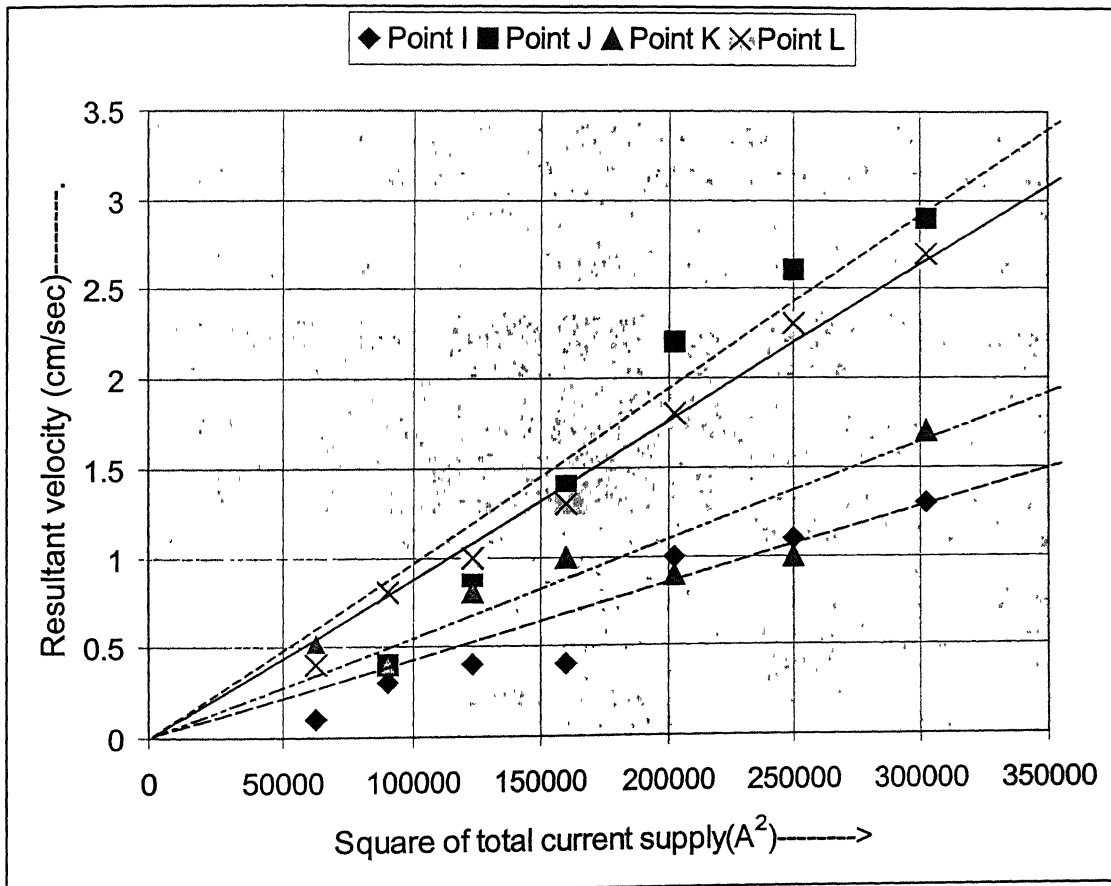


Fig. 5.24 Square of total current input versus resultant velocity graphs for points 'I', 'J', 'K' and 'L'.

ACD = 1.0 cm \longrightarrow

ACD = 1.5 cm \dashrightarrow

ACD = 2.0 cm $\cdots\cdots\longrightarrow$

Current density $\cong 0.9 \text{ A/cm}^2$

1 cm/sec

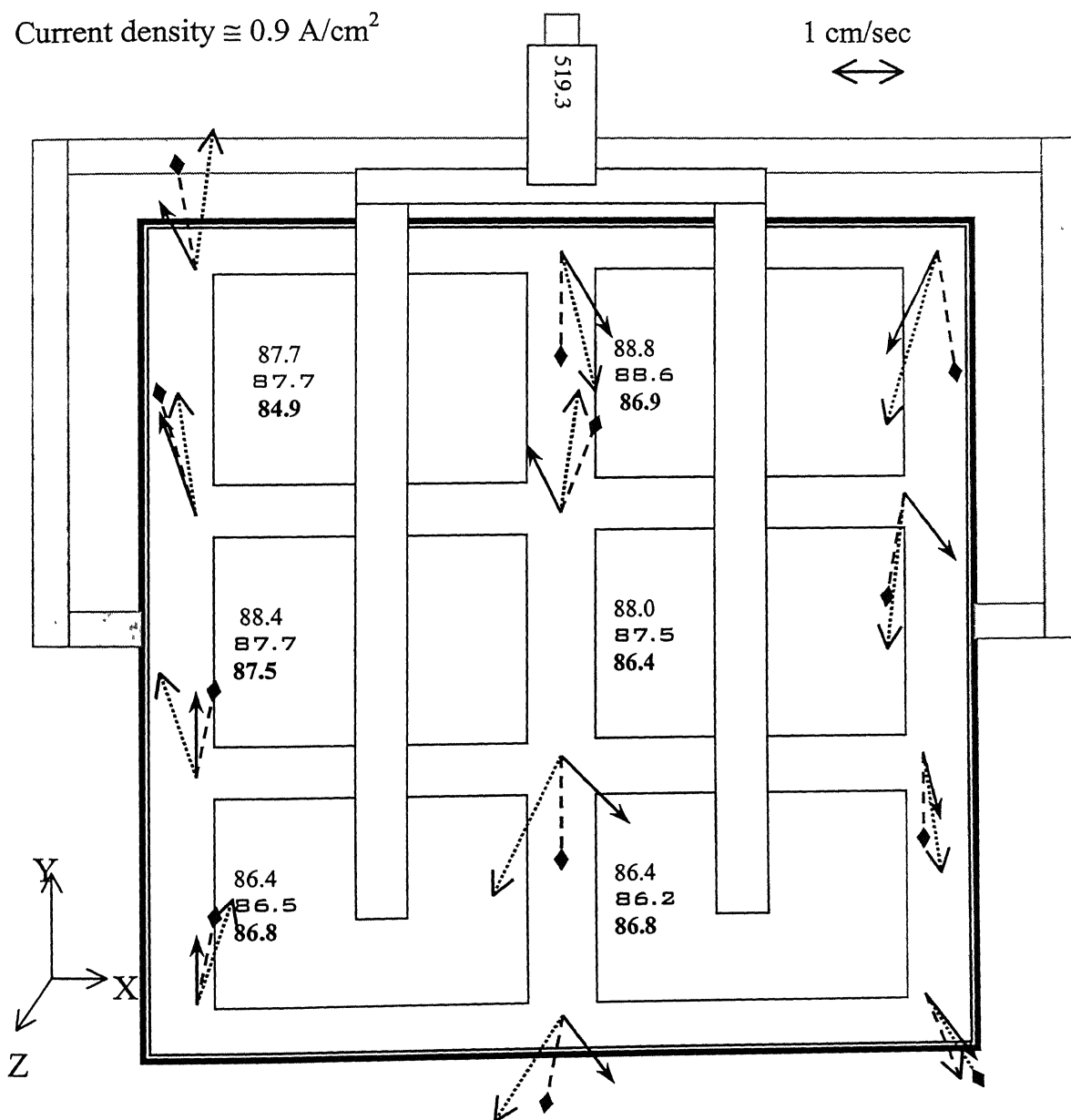


Fig. 5.25 Measured velocities for ACD 1.0 cm (solid arrow), 1.5 cm (coarse Broken Arrow) and 2.0 cm (fine Broken Arrow).

5.5.3 Effect of Bus Bar Design

Figure 5.26 shows that for the end riser design, velocity profile is clockwise and similar to that reported by Banerjee and Evans [33]. From velocity profiles shown in Fig. 5.27, it is apparent that the bus bar modification results in a vigorously circulating anti-clockwise flow in the most portion of the cell and clockwise flow in a small portion of ABEF of the cell. This observation is not conforming with the results of Evans and Banerjee [33], as shown in Fig. 5.28. Difference in flow patterns in two observations is attributed to the fact that the cell, used by Banerjee and Evans, had fourteen anodes and a different bus bar design (See Fig. 5.29). The bus bar design used by them is forming a closed loop, whereas the bus bar design used in the present investigation, as shown in Fig. 4.4b, is forming an open loop. In a closed loop configuration, the current enters from one side and exits from the opposite side (right to left), whereas in the cell used in the present investigation current entry as well as the exit are from the same side.

It becomes clear from the above results that a slight change in the bus bar design may lead to drastic change in the fluid flow. This analysis can be used for designing of an energy efficient cell with only minor modifications in the bus bar design.

5.5.4 Effect of Cold Anode

Taking out one of the anodes simulates the upset. Thus, the current previously passing through the anode is shared equally among the remaining anodes. A substantial amount of change in velocity profile results, especially in the vicinity of the cold anode, as shown in Figs. 5.30-5.33. It is seen that an anti-clockwise torque is generated due to change in magnetic field and current flow directions in the region where a cold anode is located. Generally, the cold anode in the end riser design, as shown in Figs. 5.30-5.31, results in higher clockwise velocity and larger anti-clockwise loop in the immediate vicinity of the cold anode. The quarter riser design shows reverse of the end riser design, as shown in Figs. 5.32-5.33, i.e. higher anti-clockwise velocity and larger clockwise loop in immediate vicinity of the cold anode.

It is thus, concluded that although the cold anodes have only a marginal effect on the magnetic field of a Hall cell, they have a significant effect on the melt circulation.

ACD = 1.5 cm

Current density $\cong 0.9 \text{ A/cm}^2$

→ Horizontal velocity

1 cm/sec

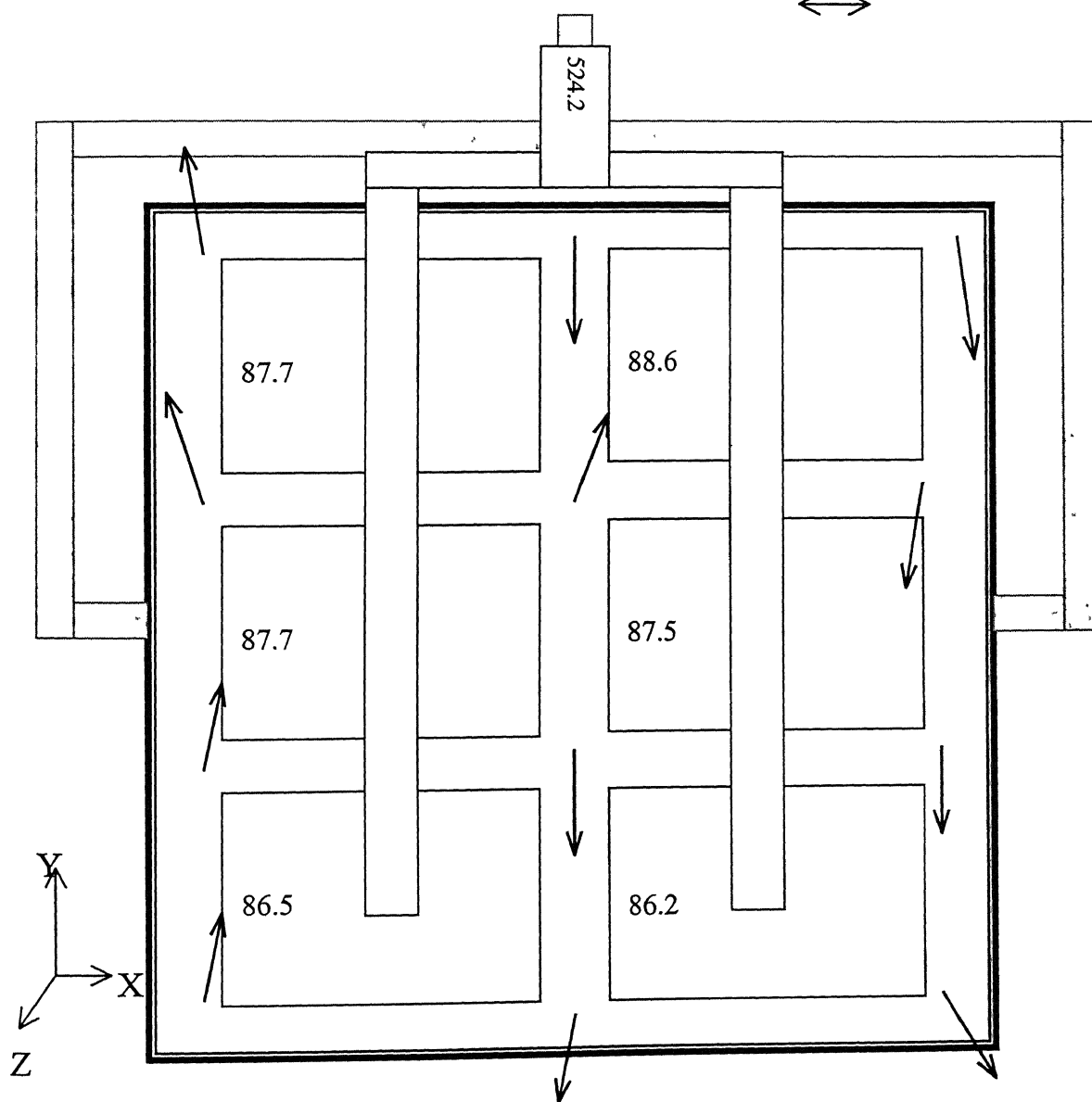


Fig. 5.26 Measured velocities for the end riser design.

ACD = 1.5 cm

Current density $\cong 0.9 \text{ A/cm}^2$

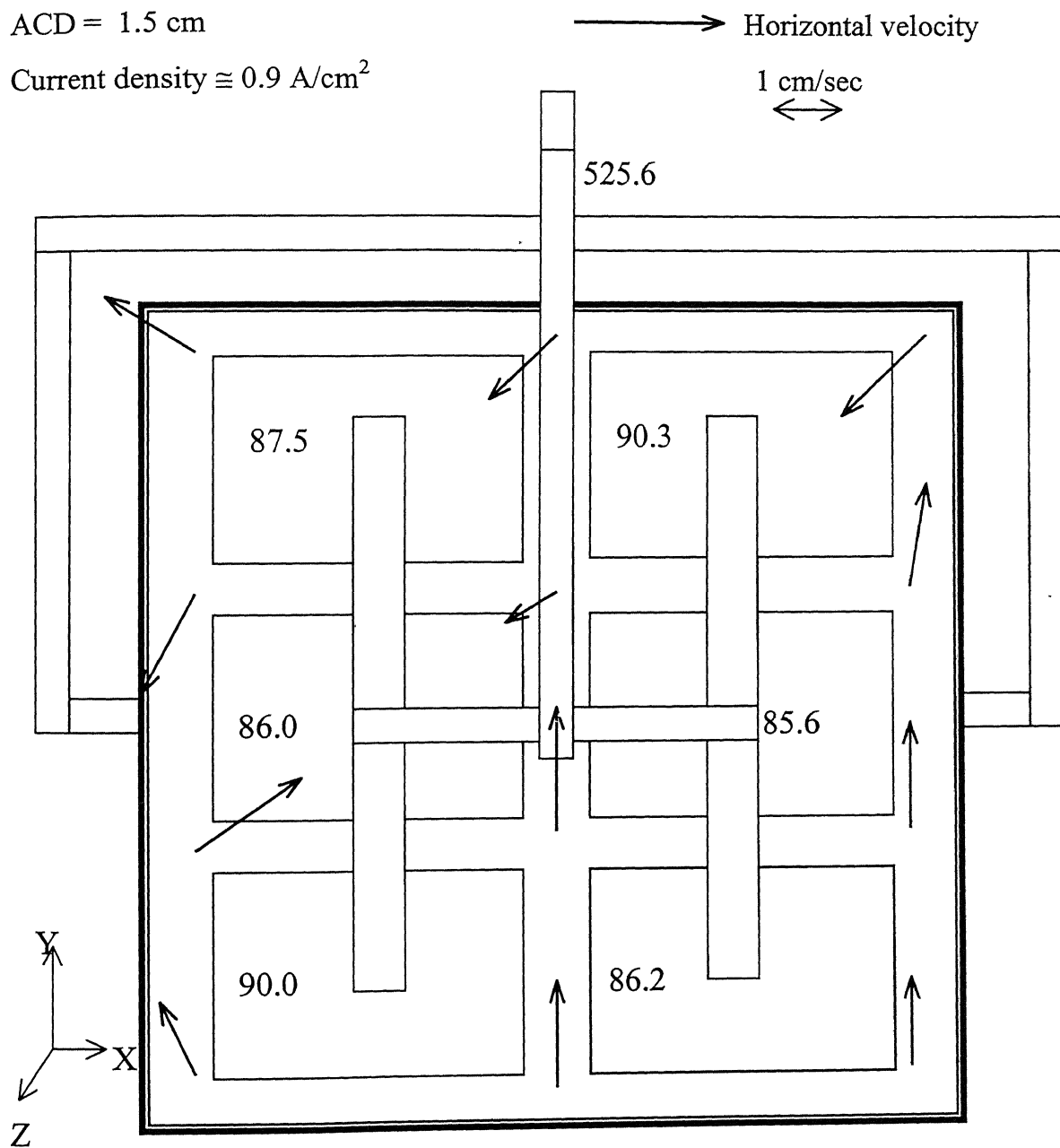


Fig. 5.27 Measured velocities for the quarter riser design.

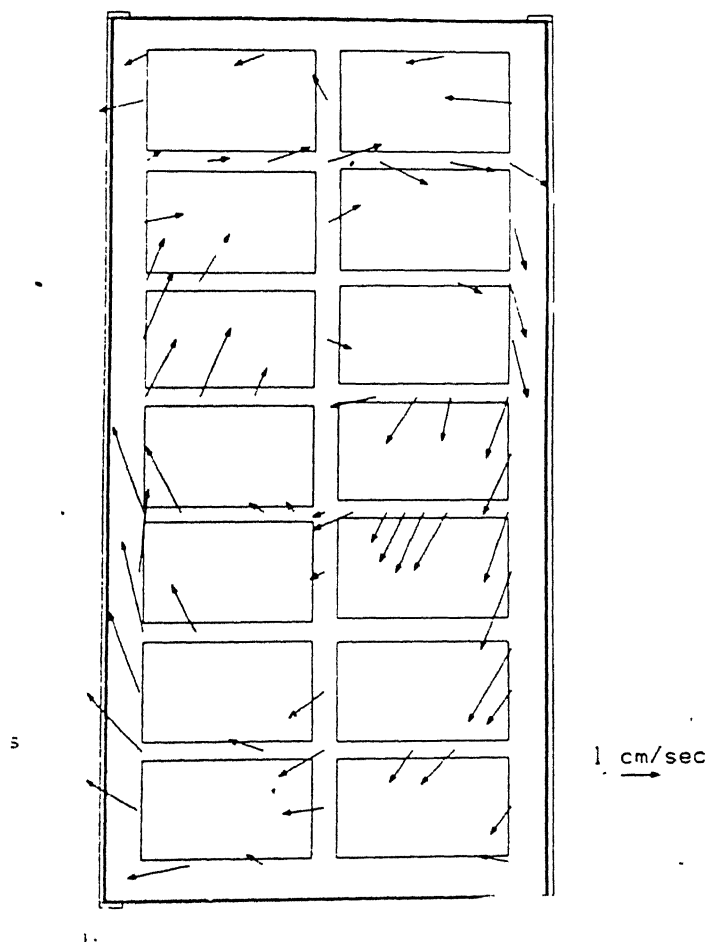
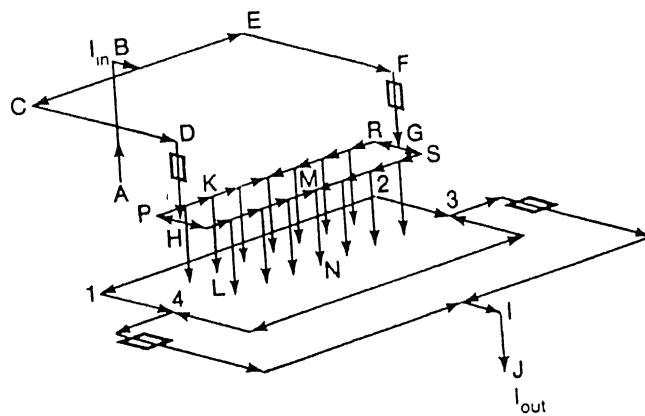
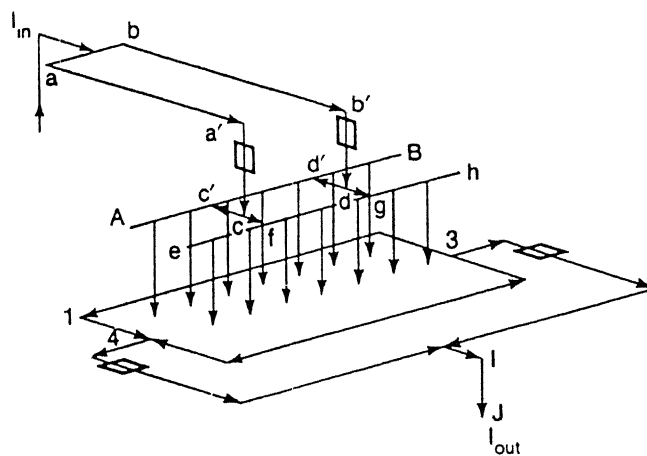


Fig. 5.28 Measured velocities for quarter riser design by Banrjee and Evans[33].



(a)



(b)

Fig. 5.29 Schematic drawing of major current flows, the cell used by Banrjee and Evans [33]: (a) end riser design, (b) the quarter riser design

ACD = 1 cm

Current density $\cong 1.08 \text{ A/cm}^2$

→ Horizontal velocity

1 cm/sec

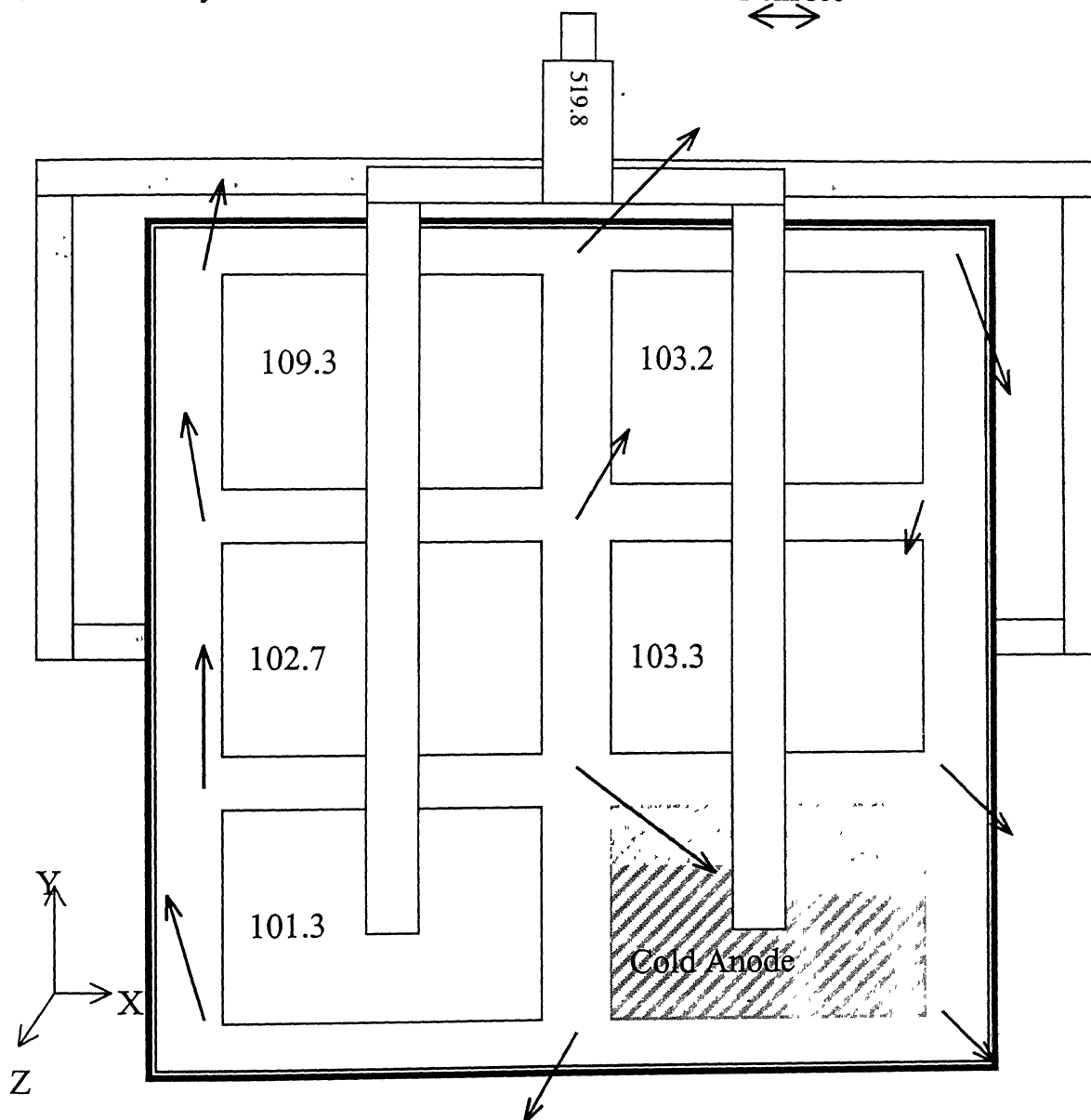


Fig 5.30 Measured velocities for end riser design with corner anode as cold anode.

ACD = 1.0 cm

Current density $\cong 1.08 \text{ A/cm}^2$

Horizontal velocity
1 cm/sec

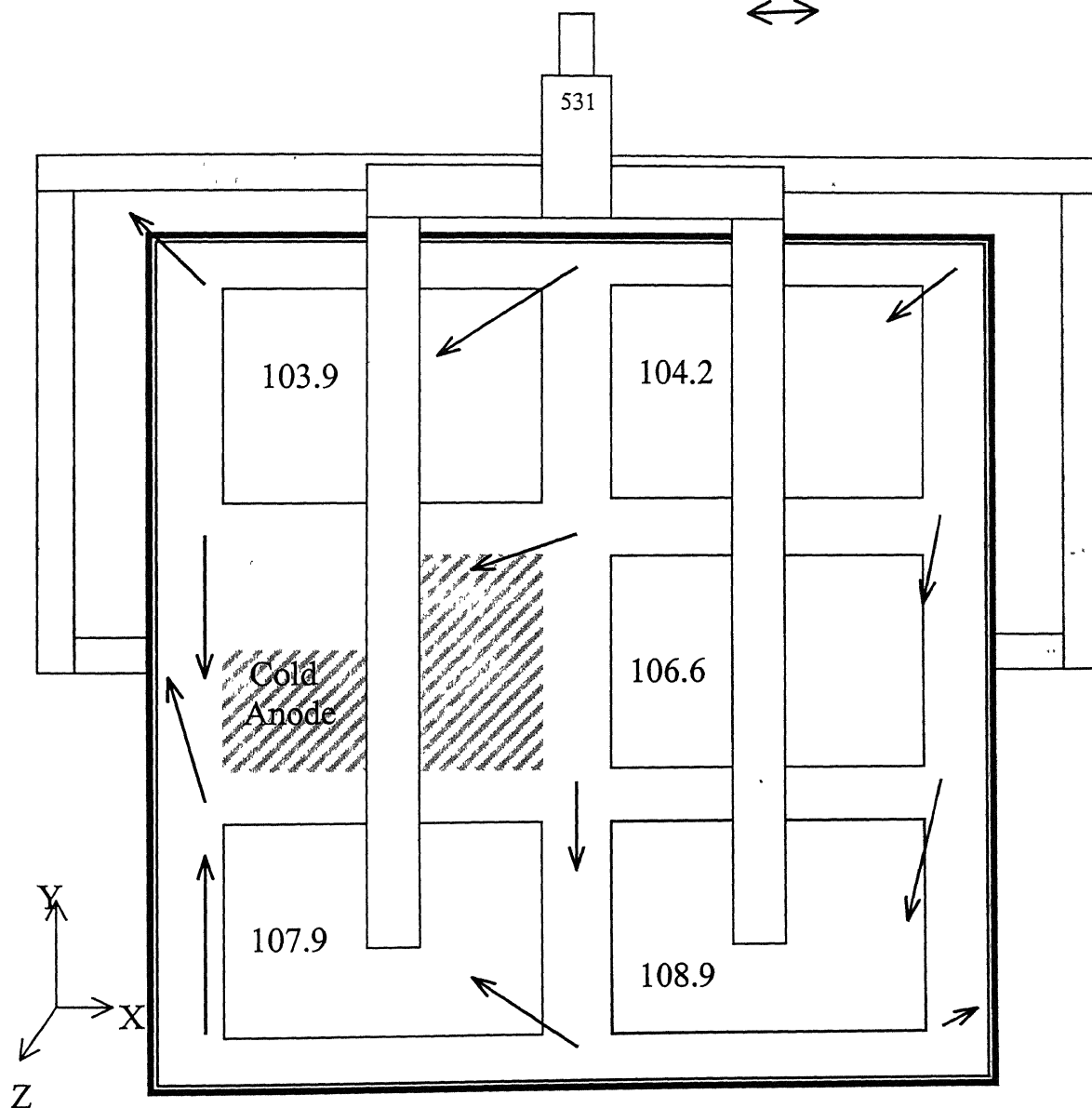


Fig 5.31 Measured velocities for end riser design with middle anode as cold anode.

ACD = 1.0 cm

Current density $\cong 1.08 \text{ A/cm}^2$

→ Horizontal velocity
1 cm/sec
↔

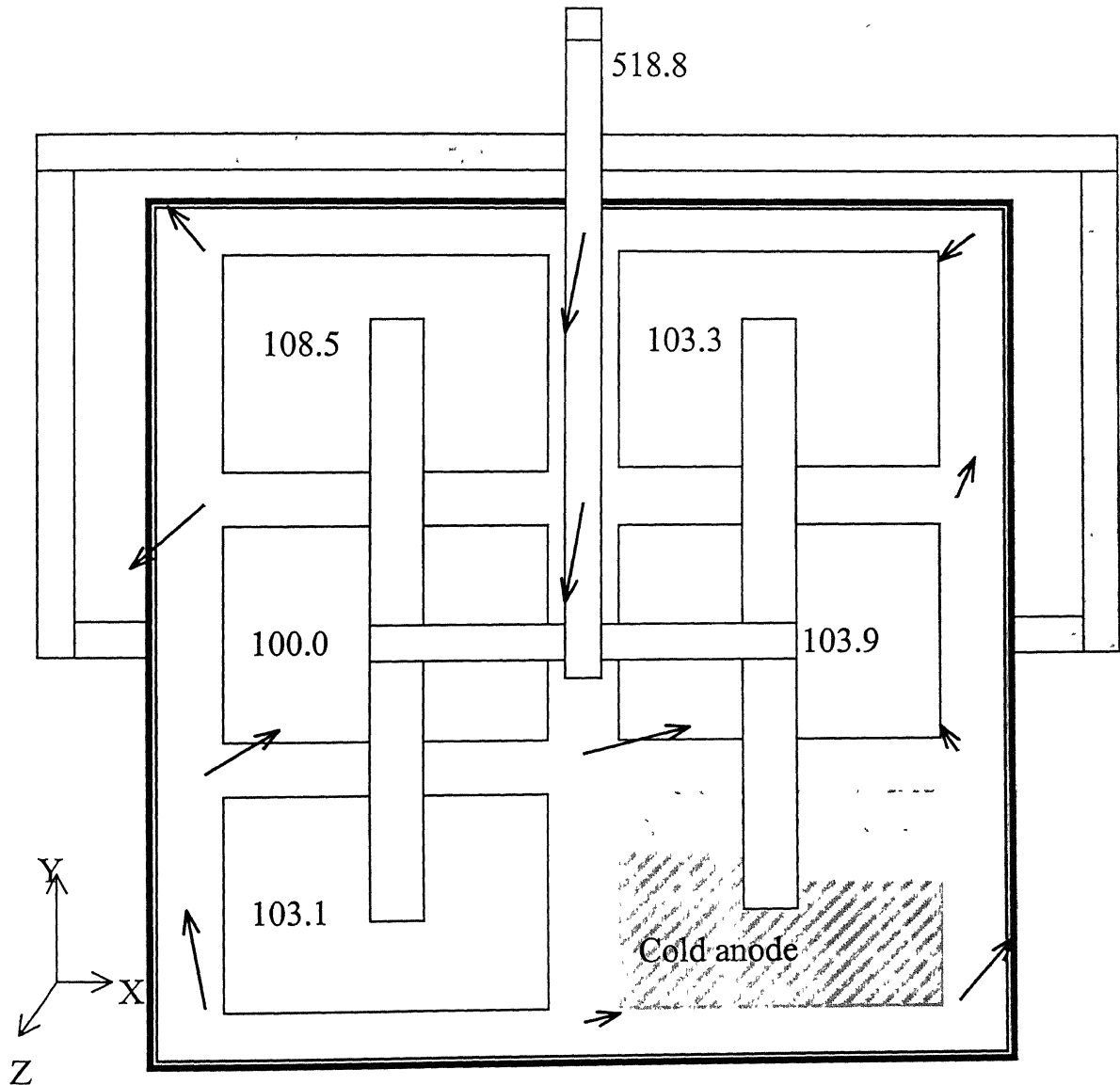


Fig 5.32 Measured velocities for quarter riser design with corner anode as cold anode.

ACD = 1.0 cm

Current density $\cong 1.08 \text{ A/cm}^2$

Horizontal velocity
1 cm/sec

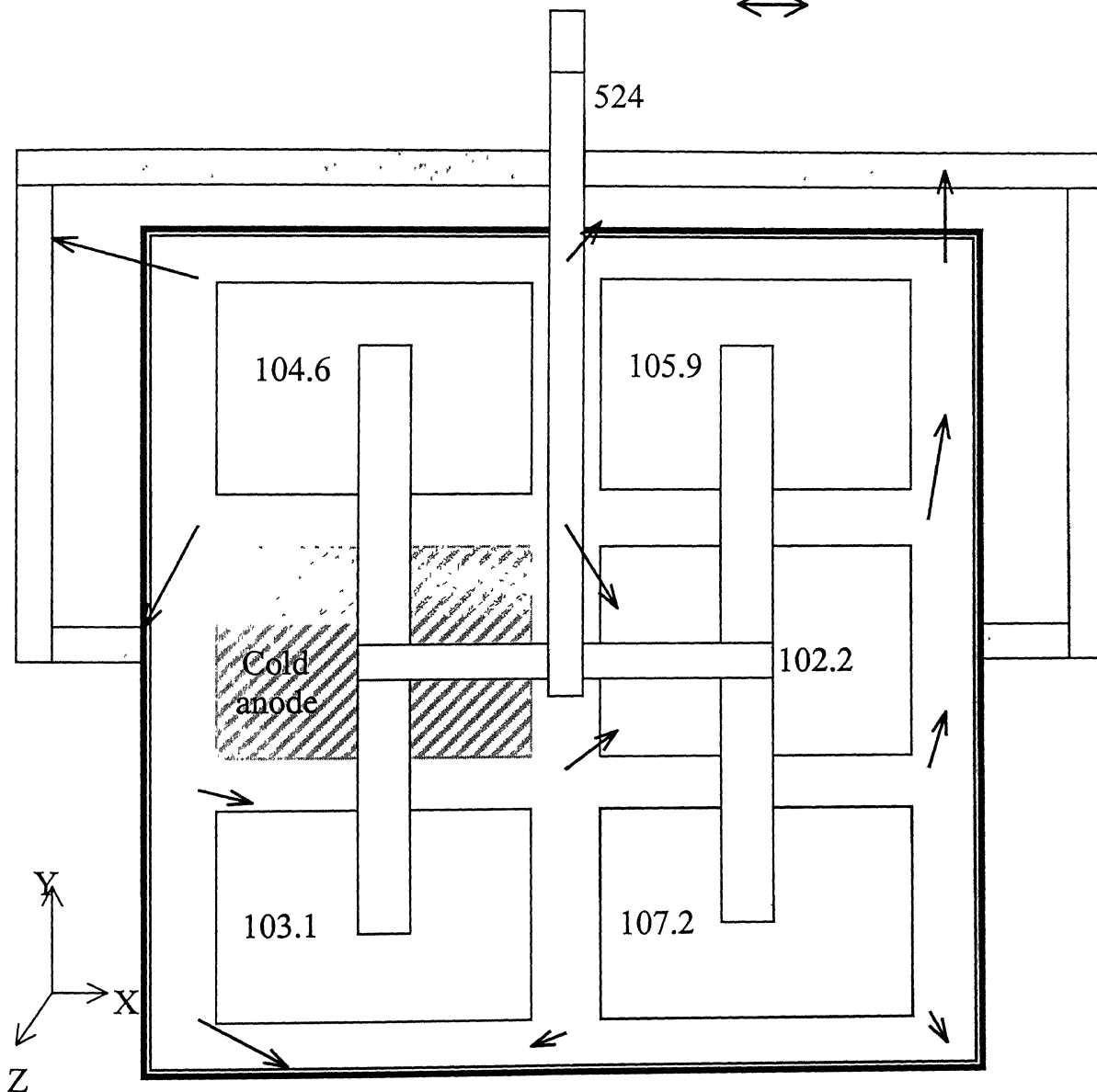


Fig 5.33 Measured velocities for quarter riser design with middle anode as cold anode.

SUMMARY AND CONCLUSIONS

The present investigation is carried out with the prime objective of generating laboratory scale data on temperature, current and magnetic fields, and velocity profiles in the simulated low temperature Hall cell for validating the mathematical models, which are being developed separately. The main aim of these models is to improve the present knowledge about magneto-hydrodynamics in Hall cells, which controls oscillations of the metal/electrolyte interface. Because of this oscillating interface, it is often not possible to operate the cell at an optimum interpole distance. As a result, the cell operates under conditions leading to the higher energy and refractory consumption.

The present investigation has been carried out in several stages. In the first stage, a multi-anode low temperature simulated Hall is designed and fabricated. The second step deals with the measurements of temperature profile, current distribution, and magnetic field. In the third step a velocity probe has been designed and fabricated, and a strategy for its calibration established. In the final step, velocity measurements have been made with changes in the cell design and operating variables.

Temperature distribution within the cell is measured with the help of a chromel-alumel thermocouple. There is no specific thermal trend in the cell. Temperature becomes more or less uniform in switched-on condition of the power supply due to forced convection within the melt.

Magnetic field measurements are conducted using a Hall effect probe at different current inputs, ACDs, anode configurations, and bus bar designs. The two bus bar designs used in the present investigation are end riser and quarter riser designs. Trend of horizontal magnetic field in each experiment is clockwise as expected. Magnetic field has slight difference in the immediate vicinity of the cold anode compare to the base case. The quarter riser design has 90° anti-clockwise magnetic field compare to

the end riser design. Vertical component of magnetic field in the quarter riser design is significantly lower than the end riser design, due to development of destructive situation for magnetic field in the quarter riser design.

The current density within the melt is established by measuring the voltage drop between two copper conductors immersed in the melt. Experimental results show that at a lower ACD, as expected, horizontal currents are higher. The 'cold anode' cases have different current distribution within the vicinity of the cold anode as compared to the 'base' case.

Horizontal velocity profile in the end riser design is clockwise due to a clockwise torque. But in case of the quarter riser design, the profile is anti-clockwise with only a small portion of the melt exhibiting a clockwise rotation. The reason for this is the rotation of the magnetic field 90^0 anti-clockwise in the quarter riser design as compared to the end riser design, which produces anti-clockwise torque. Various other effects like variations in ACD, current density, and unbalanced anode assemblies on velocity profiles within the cell have been discussed in some detail.

The following conclusions are drawn:

1. As expected, the horizontal currents are higher when ACD is reduced.
2. Current distribution in cold anode configuration is different from that in the 'base' case.
3. Vertical component of magnetic field is substantially higher in the end riser design than that in the quarter riser design. The net magnitude of magnetic field is also lower in case of the quarter riser design compare to the end riser design due to uniform distribution of current.
4. Horizontal magnetic field in the quarter riser design turns 90^0 anti-clockwise as compared to that in the end riser design leading to an anti-clockwise profile in the quarter riser design.
5. Horizontal velocity in the melt is directly proportional to the square of the total current input.

6. A substantial amount of change in velocity profile in the case of cold anode, within the immediate vicinity of cold anode, is found as compared to the 'base' case.
7. The velocity trends are clockwise in the end riser design and anti-clockwise in the quarter riser design.

It is hoped that current density, magnetic field, and velocity measurements carried out in low temperature simulated Hall cell would help in validating the mathematical models that are being developed for the design and optimization of industrial Hall-Heroult cells.

6.1 SUGGESTIONS FOR FUTURE WORK

In the present investigations, measurements made on the low temperature Hall cells are limited to only two bus bar designs. It is desirable to make measurements on current density, magnetic fields, and velocity for some other designs as well, e.g. the novel riser design, for better understanding of the effect of the bus bar design. The velocity probe can be improved by using a stronger magnet and incorporating a better design, which would caused the minimum interference with the fluid flow. Effects of varying wall to anode distance, simulating ledge by placing a non-conducting material along the walls, etc. on current, magnetic field, and velocity profile may be examined.

APPENDIX A

The first part of appendix A contains the flow chart and program used to calculate the velocity in the simulated cell. The latter part of the appendix has experimental set-up and procedure for validation of experiments.

A.1 FLOW CHART AND PROGRAM STRUCTURE

The algorithm, used to fit the experimental data to separate out the emf induced by the melt flow, is based on the least square method. The flow chart of the program is shown in Fig. A.1. The program is written in C++, and the program listing included.

A.1.1 The Structure of Program Used to Calculate Velocity in the Cell

The programs written in C++ by using the algorithms define in flow chart.

```
#include<iostream.h>
#include<stdio.h>
#include<math.h>

// Declaration of global constants, characters and functions
float fun(int n,int m,float ci);
int i,j,k;
float E[12],I[12],t[12],d[12],cf[5][5],coff[5][5],y[12],com=0,r;
float flag[5],flag5,f,v,ci;

//Data file declaration
FILE *fptr;
Char fname[2];

//Starting of main function
main()
{
```

```

//Declaration of local constants for function main
float cu,tt,xx,yy,res,ang;
int mm,nn;
//Entering the value of current at which you want velocities
cout<<"Enter the value of current";
cin>>cu;
cout<<"-----"<<endl;
cout<<"Point          Vx          Vy          Resultant          Angle"<<endl;
cout<<"-----"<<endl;
// Calculations for Resultant and Angle
for(mm=65;mm<=76;mm++)
{
    // Calling of Function fun()
    xx=fun(mm,120,cu);
    yy=fun(mm,121,cu);
    // Calculation of Resultant
    res=sqrt(xx*xx+yy*yy);
    // Calculation of angle with +x-axis
    ang=asin(yy/res)*180/3.1414;
    if(xx<0 && yy>=0)
        ang=180-ang;
    if(xx<0 && yy>0)
        ang=-180-ang;
    printf("Point %c %2.1f %2.1f %2.1f %3.1fn",mm,xx,yy,res,ang);
};
}
//Structure of Function fun()
float fun(int n,int m,float ci)
{

```

```

flag[0]=flag[1]=flag[2]=flag[3]=flag[4]=0;
fname[0]=n;
fname[1]=m;
//Opening and Reading the Data File
fptr=fopen(fname,"r");
if(fptr==NULL)
cout<<"File reading unsuccessful"<<endl;
for(i=0; i<12; i++)
    fscanf(fptr,"%f%f",&I[i],&E[i]);
for(i=0; i<12; i++)
    y[i] =E[i];
//Calculation of Coefficients of Equations
for(j=0;j<=2;J++)
{
    flag5=0;
    for(i=0; i<12; i++)
        flag5=flag5+ y[i]*pow(I[i],j);
    d[j]=flag5;
}
cf[0][0]=12;
for(j=1;j<=4;j++)
for(i=0; i<12; i++)
    flag[j]=flag[j]+pow(I[i],j);
cf[1][0]=cf[0][1]=flag[1];
cf[2][0]=cf[1][1]=cf[0][2]=flag[2];
cf[2][1]=cf[1][2]=flag[3];
cf[2][2]=flag[4];
//Solution of Equations by Gauss elimination method
for(k=1;k<=2;k++)

```

```

for(i=k; i<=2; i++)
{
    d[i]=d[i]-((d[k-1]*cf[i][k-1])/cf[k-1][k-1]);
    for(j=2;j>=0;j--)
        cf[i][j]= cf[i][j] -((cf[k-1][j]* cf[i][k-1])/cf[k-1][k-1]);
}
for(i=2; i>=0; i--)
{
    f=0;
    for(j=i+1;j<=2;j++)
    {
        f=f+cf[i][j]*coff[j];
    }
    coff[i]=( d[i]-f)/cf[i][i];
}

```

//Calculation of Velocity Multiplying Slope with emf.

```

if(fname[1]=='x')
    v=-850;
if(fname[1]=='y')
    v=1375;
float
ll=((coff[0]+coff[1]*ci+coff[2]*ci*ci)-
((coff[0]+coff[1]*100+coff[2]*10000)+(coff[1]+2*coff[2]*100)*(ci-100)));
//Closing the Data File
fclose(fp);
//Returning the Value of Velocity Component to Calling Function
return(ll*v);
}

```

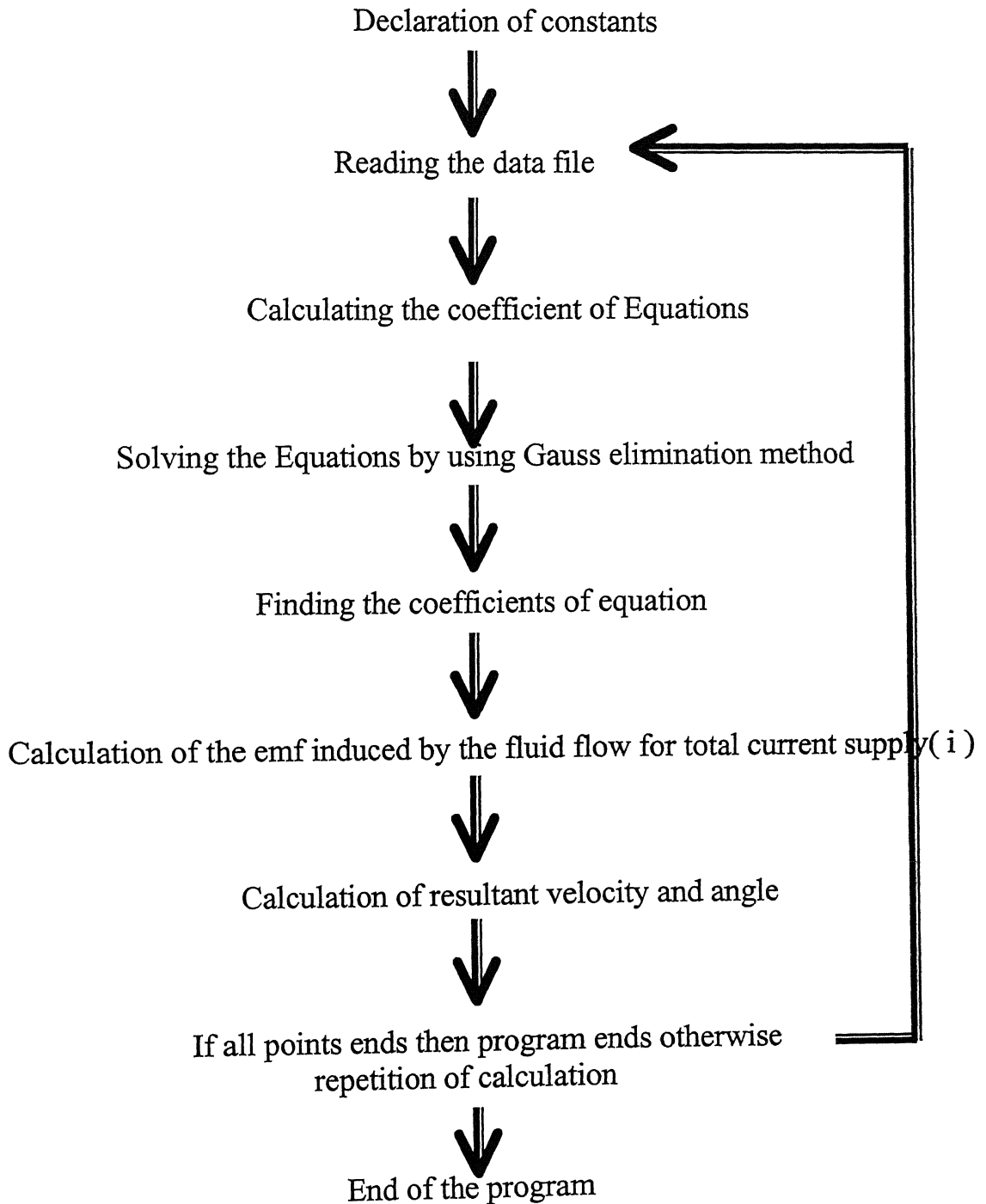


Fig. A.1 Flow chart of the program used for velocity calculations using velocity probe data.

A.2 VALIDATION OF EXPERIMENTAL PROCEDURE

The objective of validation of experiments is to establish that the current flow through the melt indeed follows the Ohm's law. Since the cell has three components of emfs, the electromagnetically-induced flow is eliminated in these validation experiments by confining the current flow to a small portion of the overall melt. Thus, only the other two emfs contribute.

A.2.1 Experimental Set-Up

The calibration apparatus, as described in Chapter 4, is used here too. Two steel electrodes are immersed in the melt. Since the calibration pot is insulated from the motor and ground, there is no leakage of current. The electrodes have round edges to minimize the disturbances in the melt flow due to immersion of the electrodes. (see Fig. A.2). The electrodes are covered with an insulating tape 1.0 cm above the bottom edge to ensure constant area for the current flow. This results in a constant current density at a predefined total current input through the electrodes. The velocity probe is rigidly fixed between the two electrodes, as shown in Fig. A.3. This gives no disturbance in the current distribution when the melt flows radially due to rotation of the calibration pot. Since the electrodes are rigidly fixed with the probe, the current distribution around the probe remains the same, even when the position of the probe changes within the pot. The positioning of velocity probe with respect to the electrodes is shown in Fig. A.4.

A.2.2 Experimental Procedure

The electrode wires are connected to the power supply. The probe, attached to electrodes, is inserted into the melt in the calibration pot with the help of a rigid support. The calibration pot is rotated with the help of an electric motor. The speed of rotation of the melt is supposed to be the same as that of the calibration pot. Electric current, supplied to the electrodes, is varied from 0 to 15 Amp in steps of 3.0 Amp. Thus, the current density varies from 0 to 6.0 Amp/cm². The melt flow is only due to the circular motion of the calibration pot. Predefined velocity below the velocity probe is maintained by controlling the rpm of the motor and the distance of the velocity

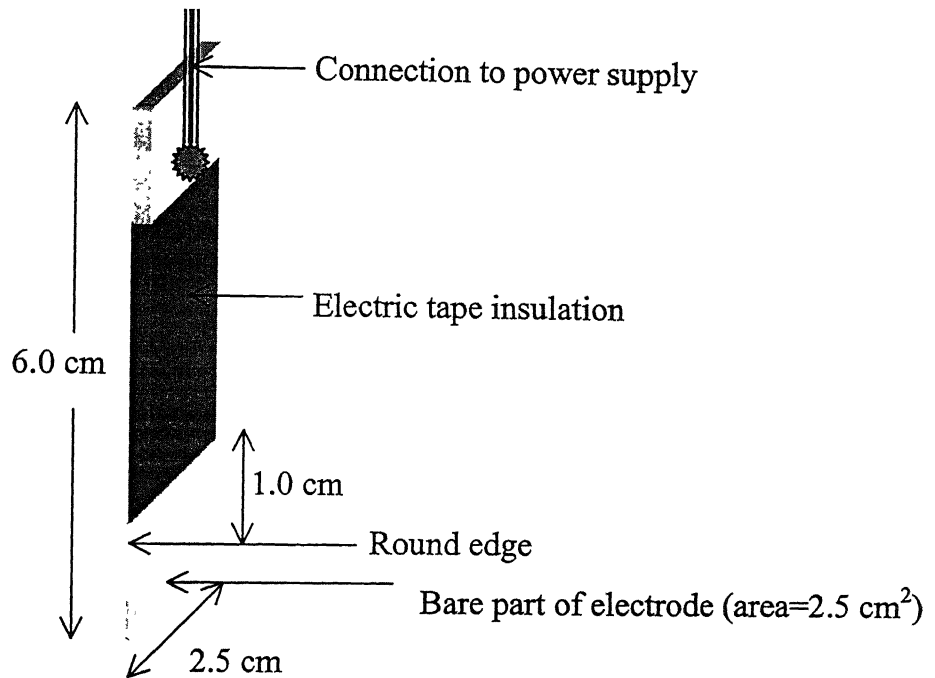


Fig. A.2 The shape and size of one electrode made of mild steel.

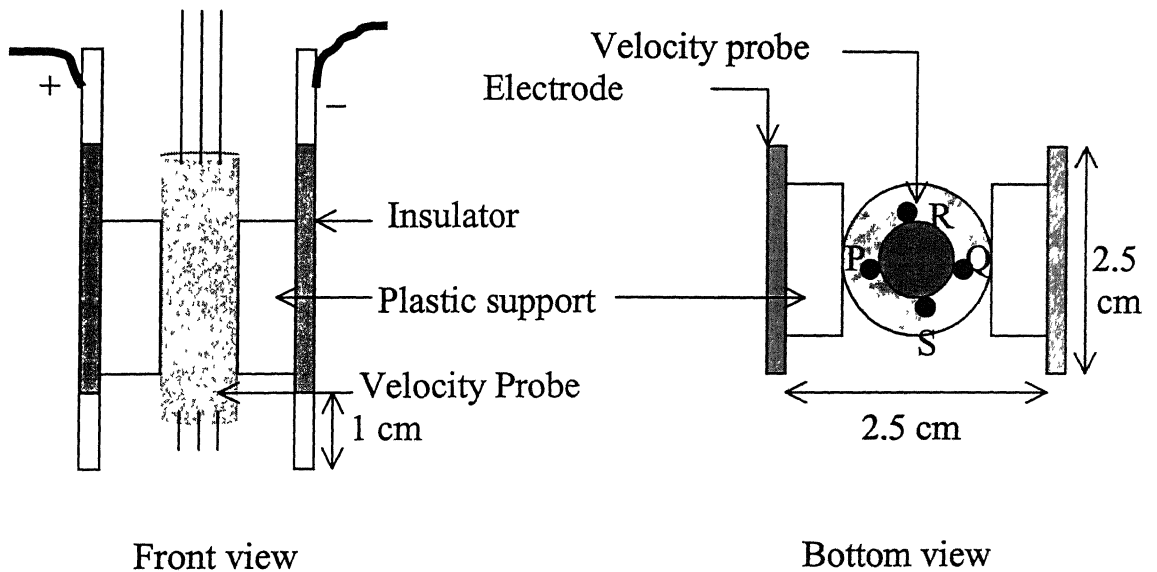


Fig. A.3 The arrangement of electrodes used to validate the experimental procedure for velocity measurements.

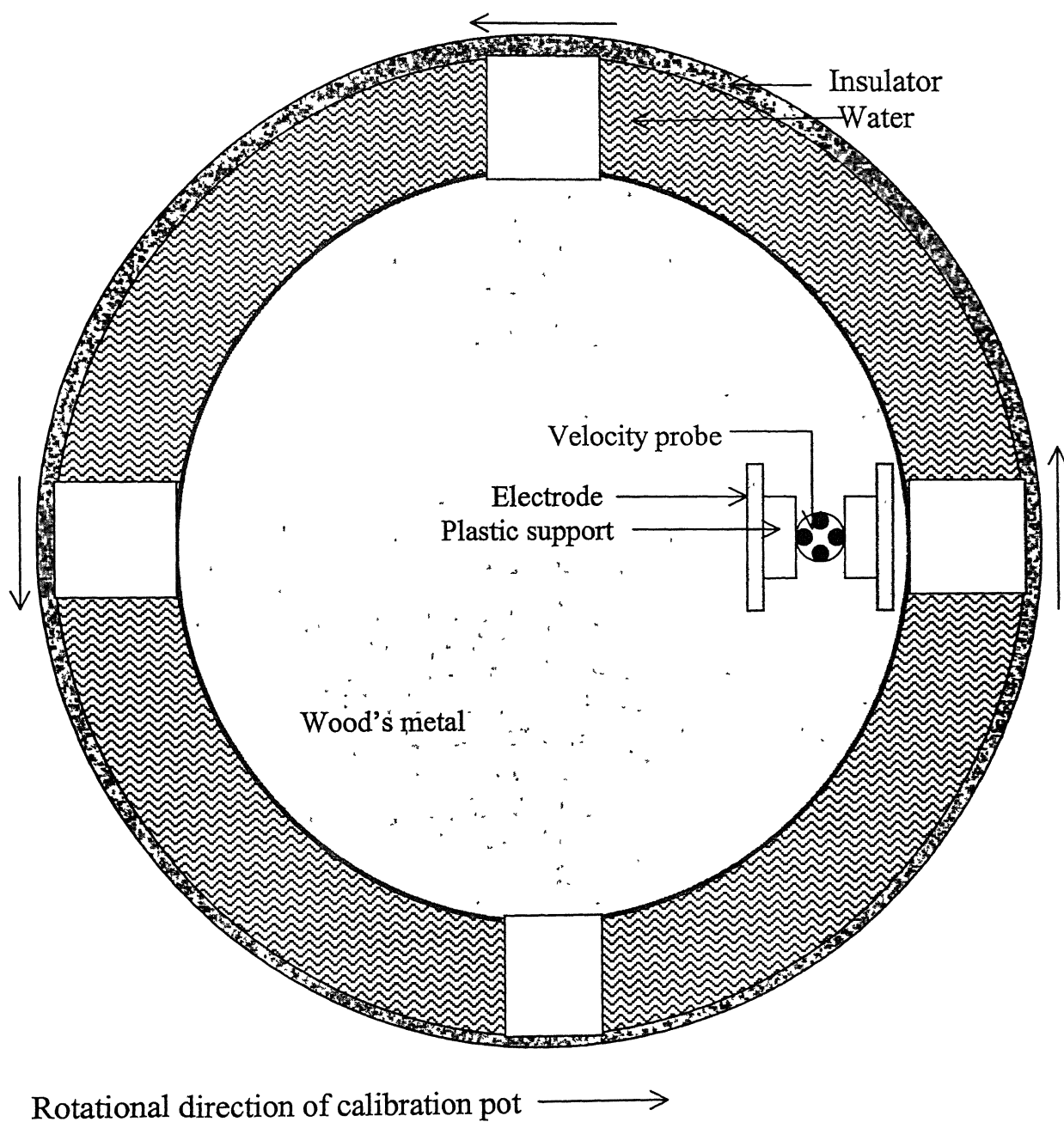


Fig. A.4 Experimental set-up of validation experiment (Top view).

probe from the center of the calibration pot. The nano-voltmeters readings are recorded for different speeds of the melt below the velocity probe and total current input. Magnetic field is measured for 6.0 and 15.0 Amp current input.

A.2.3 Results and Discussion

Magnetic fields and velocities are measured for different sets of experiments with different current densities and velocities of the melt.

A.2.3.1 Magnetic Field Measurements: Magnetic field, near the velocity probe, is measured at current input of 6.0 and 15.0 Amp. Recorded values of magnetic field are tabulated in Table A.1, indicating that the operating conditions with respect to the magneto-hydrodynamics in the calibration pot and the simulated Hall cell are more or less the same.

Table A.1 Magnetic field near the probe in the calibration pot for the current inputs of 6.0 and 15.0 Amp.

Reading	X-component (Gauss)		Y-component (Gauss)		Z-component (Gauss)	
	6.0 Amp	15.0 Amp	6.0 Amp	15.0 Amp	6.0 Amp	15.0 Amp
First	0.9	1.9	0.4	0.8	1.0	2.3
Second	0.8	2.2	0.2	0.6	0.9	2.1
Third	0.9	2.2	0.3	0.8	0.8	2.1

A.2.3.2 The EMF Measurements: The emf measurements are reported in Fig. A.5 and Table A.2. The measurements show that the emf readings are linearly increasing with increase in current input for a constant speed of the melt flow, simply following the Ohm's law. The shifting of lines at different speeds of the melt is approximately the same as the emf difference generated by the velocity difference between the two experiments.

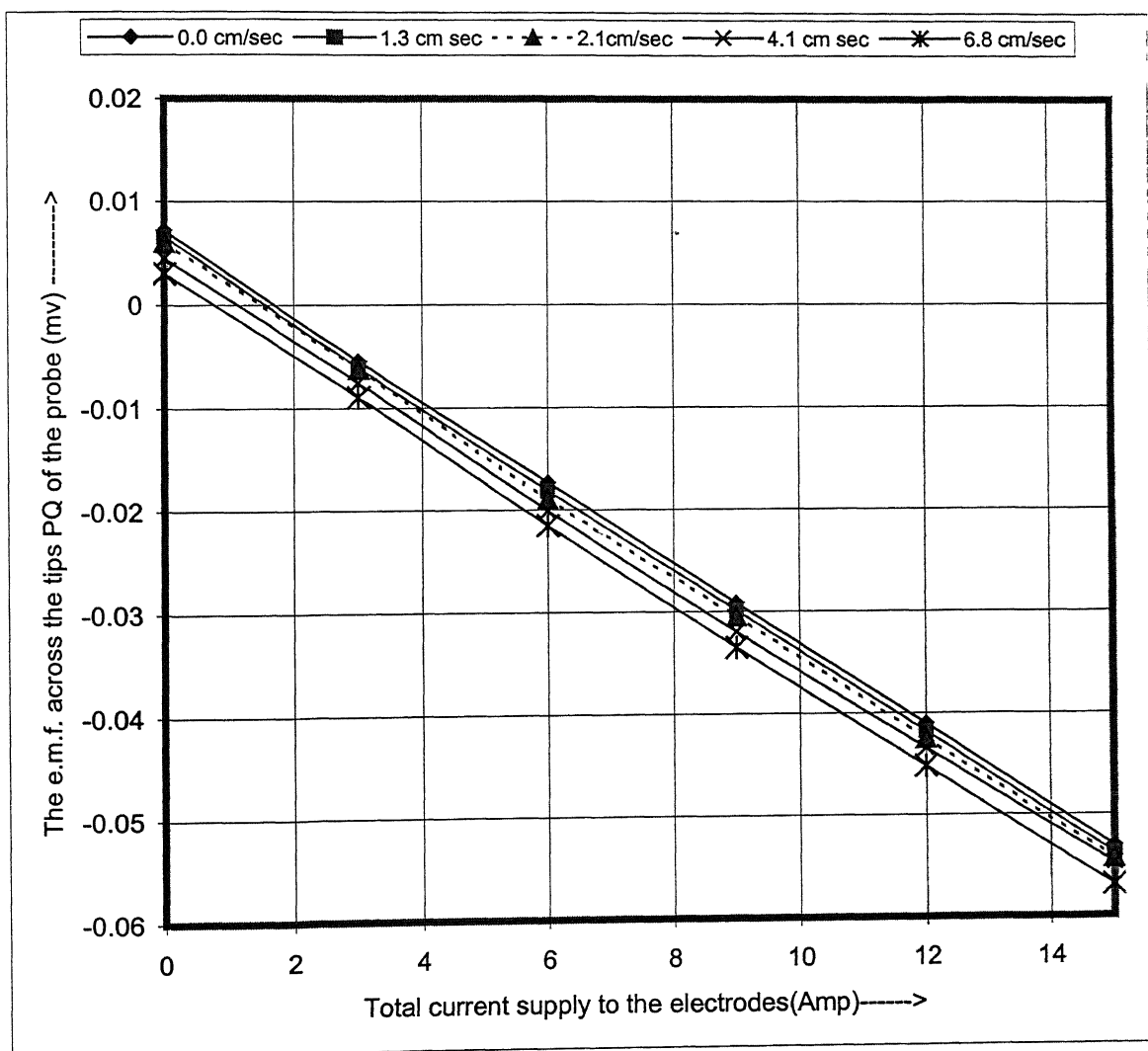


Fig. A.5 Current verses emf plots at different velocities of the melt below the velocity probe.

Table A.2 Emf readings (mv) for varying current inputs at different melt velocities.

Current (Amp)	0.0 cm/sec	1.3 cm/sec	2.1 cm/sec	4.1 cm/sec	6.8 cm/sec
0	0.00720	0.00662	0.00607	0.00451	0.00305
3	-0.00545	-0.00610	-0.00623	-0.00757	-0.00895
6	-0.01733	-0.01813	-0.01893	-0.02009	-0.02157
9	-0.02920	-0.02992	-0.03050	-0.03202	-0.03355
12	-0.04105	-0.04180	-0.04251	-0.04343	-0.04521
15	-0.05310	-0.05380	-0.05432	-0.05480	-0.05692

A.2.4 Conclusion

It is concluded from the above results that current flow in the melt follows Ohm's law. Difference in the emfs for two different velocities of the melt below the velocity probe is approximately the same as induced by the difference in velocity of the melt at the same current input. Magnitude of the net emf is increasing with increase in melt velocity. Since the emf due to current flow is constant and the emf due to melt flow increases with melt velocity the lines are shifting to higher magnitude.

REFERENCES

1. Peacy and Medlin, Light Metals 1979, p. 475
2. Burkin A. R., Production of Aluminium and Alumina, Published by John Wiley & Sons, 1987
3. Wahnsiedler W. E., Light Metals 1987, p. 269
4. Potocnik V., Light Metals 1989, p. 227
5. Segatz M., Vogelsang D., Droste C., Baekler P., Light Metals 1979, p. 475
6. Fraser K., Tayler M., Jenkin A. , Light Metals 1990, p. 221
7. Purdi J. M., Bilek M., Tayler M. P., Jhang W. D., Wilch B. J., Chen J. J., Light Metals 1993, p. 355
8. Robl R. F., Haupin W. E., Sharma D., Light Metals 1977, p.185
9. Evans J. W., Zundelvich Y., Sharma D., Met. Trans. 12 B, 1981, p. 343
10. Echelini M., Lacunza M., Crespo N., Light Metals 1988, p. 557
11. Haupin W. E., JOM July 1971
12. Ahmad H. A., Elrefaie F. A., El-Demardash, El-Raghy S. M., Bassury Z., Light Metals 1993, p. 375
13. Dervedde E., Cambridge L. E., Light Metals Vol 1 1975, p.111
14. Johnson A. R., JOM 1988, p. 11
15. Arita Y., Urata N., Ikeuchi H., Light Metals 1978, p. 59
16. Crojothheim K., Krohn C., Neeumann R., Toklep K., Met. Trans. Vol.4 1973, p. 1945
17. El-Raghy S. M., Light Metals 1991, p. 399
18. Evans J. W., Zundelvich Y., Sharma D., Met. Trans. 12 B June 1981, p. 353
19. Furman Adian, Mathematical Modeling applied to Aluminium Reduction Cells, Heat and Mass Transfer in Metallurgical Systems, p. 215
20. Solinas G. A., Light Metals Vol. I 1978, p. 15
21. Urata N., Arita Y., Ikeuchi H., Light Metals Vol. I 1975, p. 233

22. Muller T. B., Solberg K. O., Light Metals 1973, p. 151
23. El-Demerdash M. F., Khalil E. E., Ahamd H. A., Reda S., Light Metals 1993, p. 369
24. Bradley B. F., Dewing E. W., Rogers J. N., Light Metals 1981, p. 541
25. Johnson A. R., Light Metals 1978
26. Bilek M. M., Zhang W. D., Stevens F. J., Light Metals 1994, p. 323
27. Fortien S., Gerhadf M., Gesing A. J., Light Metals 1984, p. 721
28. Lee H. C., Evans J. W., Light Metals 1985, p.565
29. Taberaux A. T., Hester R. B., Light Metals 1985, p. 519
30. Lobmann G., Light Metals 1992, p. 441
31. Urata N., Light Metals 1985, p. 581
32. Lee H. C., Evans J. W., Vives C., Met. Trans. 15 B 1984, p. 734
33. Banrjee S. K., Evans J. W., Met. Trans. 21 B Feb 1990, p. 59

A-132012

A 132012
Date Slip

Date Slip

This book is to be returned on
the date last stamped.

[illegible]